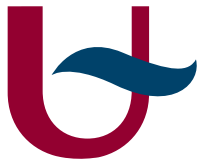

UNIVERSITEIT ANTWERPEN

Faculteit Wetenschappen

Departement Fysica

An *ab initio* study of the adsorption of atoms and molecules graphene

---

Een *ab initio* studie van de adsorptie van atomen en moleculen op grafeen

Proefschrift voorgelegd tot het behalen van de graad van doctor in de wetenschappen aan de Universiteit Antwerpen te verdedigen door

Ortwin Leenaerts

Promotor: Prof. dr. B. Partoens
Co-promotor: Prof. dr. F. M. Peeters

Antwerpen 2010

Contents

List of abbreviations

1D, 2D, 3D	one-, two-, three-dimensional
BZ	Brillouin zone
CNT	carbon nanotube
CT	charge transfer
CVD	chemical vapor deposition
DFT	density functional theory
DOS	density of states
FET	field effect transistor
FG	fluorographene
FLG	few-layer graphene
GGA	generalized gradient approximation
GO	graphene oxide
HF	Hartree-Fock
HOMO	highest occupied molecular orbital
HOPG	highly ordered pyrolytic graphite
HK	Hohenberg-Kohn
IE	ionization potential
KS	Kohn-Sham
LCAO	linear combination of atomic orbitals
LDA	local density approximation
LUMO	lowest unoccupied molecular orbital
MD	molecular dynamics
MO	molecular orbital
MP	Monkhorst-Pack
PBE	Perdew-Burke-Ernzerhof
PAW	projector augmented wave
POMO	partially occupied molecular orbital
TB	tight-binding
vdW	van der Waals
WF	work function

Preface

Dimensionality is one of the most decisive characteristics of a material: the same substance can have very different properties when forming a 0, 1, 2, or 3 dimensional structure. While quasi zero dimensional (e.g. quantum dots), quasi one dimensional (e.g. nanotubes and nanowires) and of course three dimensional crystal structures have been and are widely studied, the research on two dimensional crystals has been minimal until the recent (2004) experimental realization of two dimensional atomic crystals [1]. Among these newly discovered materials, a single one, called graphene, has been catching almost all attention because of its extraordinary properties and its relative ease of fabrication. This remarkable 2D crystal is nothing more than a single layer of graphite and has, as such, already been known for some time as a theoretical material.

Graphene is the main subject material of this thesis, but only a few of the unique features of graphene will be explored because it has so many interesting aspects that it is impossible to cover them all. This is well illustrated by the exponentially growing literature which already reached over 2000 research papers in 2009 alone. This enormous interest can be explained on the one hand by the special properties of graphene, which makes it interesting from an academical point of view, and on the other hand the variety of possible applications that seem to follow from these unique features. That the entire field of graphene research has grown well mature now is evidenced by 8 separate PACS classification numbers on topics involving graphene.

The focus of the work presented here is on the interaction between graphene and atomic and molecular adsorbates. With the use of ab initio calculations this interaction is simulated and the results are linked with experimental findings. The thesis is divided into 4 parts: in the first part some properties and applications of graphene are discussed and also the most widely used methods to produce graphene samples are presented. The second part is more technical and deals with all the theoretical tools that are needed to perform and interpret the different calculations that are done in the third part. In this third part, physisorption and chemisorption on graphene are investigated, together with the permeability of graphene membranes

and the properties of the graphene derivatives graphane and fluorographene. Finally, a summary and outlook are given.

Acknowledgements

I wish to express my gratitude here to my promotor Prof. B. Partoens and my copromotor Prof. F. M. Peeters for giving me the opportunity to work in the Condensed Matter Theory group (CMT) of the University of Antwerp and the chance to learn from their expertise in the field. Their willingness to answer all the questions I have had and their ability to recognize interesting research topics at an early stage have been indispensable for the results presented in this thesis. I have also benefited a lot from numerous interesting discussions with colleagues from the CMT group. Special thanks in this regard go to Hartwin Peelaers who has always been prepared to answer a diversity of practical and technical questions.
Finally, I want to thank all the other colleagues at the university, friends, and family for their (occasional) interest in the research that I was doing. Without these stimulations it would have been much harder to produce this thesis.

Part I

Graphene: Introduction

Chapter 1

Carbon allotropes

Carbon forms the basis of all organic molecules, which makes it the most important element for life on our planet. Furthermore it is present in over 95% of the known chemical compounds overall [2]. It is unequaled by any of the other elements of the periodic table when it comes to the versatility of bond formation: carbon atoms bind to a variety of other atoms, both electropositive and electronegative, and are able to form long chains or crystals when bonding among themselves. Even when the rich chemistry resulting from the interaction with other elements is excluded, carbon possesses an extraordinary flexibility and has a variety of interesting allotropes. The diversity of the bonds it can form is nicely demonstrated by the properties of the two best known carbon materials, graphite and diamond. These two crystals appear to be so different from one another that it might be difficult to convince the layman of the fact that they consist of the same element and only differ insofar the type of bonding is concerned.

The carbon allotropes, i.e. those materials which consist entirely of carbon atoms, can be divided into three classes according to the type of bonds linking the atoms together. This type of bonding depends on the hybridization of the carbon atomic orbitals which is (usually) sp^2 or sp^3. When all carbon atoms have sp^3-hybridization, diamond-structures are formed and in the case of sp^2-hybridization one gets graphitic materials. The third class of allotropes contains the amorphous carbons which consist of (non-crystalline) mixtures of sp^2- and sp^3-hybridized carbon atoms. A schematic overview of the different carbon allotropes is given in Fig. 1.1. The mixed carbon allotropes are interesting materials but they play no role in this thesis and are therefore not given any further attention. The other two classes are shortly described in the following.

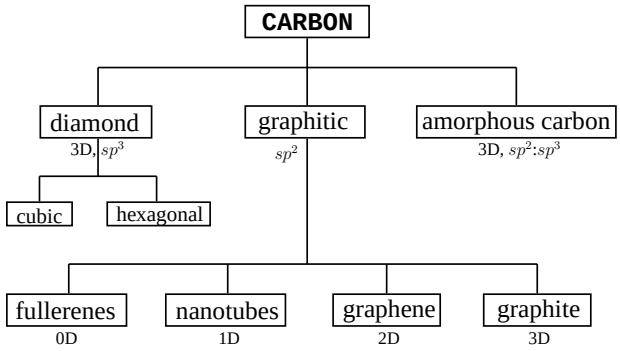

Figure 1.1. *The different carbon allotropes: the dimensionality and (main) hybridization are indicated.*

1.1 Diamond

Diamond is the strongest of all bulk materials and has the highest thermal conductivity ever measured. It owes these exceptional properties to the strong covalent bonding between its atoms. Each atom in diamond has four bonding partners with which it forms equivalent sp^3-bonds. In this way, different crystal structures can be built such as the usual cubic diamond structure and the hexagonal Lonsdaleite. All these materials are characterized by an exceptional hardness and they have a large band gap in their electronic spectrum which makes them excellent insulator and gives them their transparent appearance. Cubic diamond is the thermodynamically stable form of carbon for pressures above 60 kbar.

1.2 Graphitic materials

In contrast to diamond, the carbon atoms of the second class of allotropes are sp^2-hybridized. These sp^2-bonded materials are special in that they can have any dimension ranging from 0D fullerenes to 3D graphite. They are often referred to as graphitic materials since graphite is the best and longest known representative of this class.

1.2.1 Graphite

Graphite is the most stable carbon allotrope and is therefore most common in nature. Consequently, it has already been known for centuries. It owes its primary use as a material to make writing tools (i.e. pencils) and lubricants to its unusual layered structure at the nanoscale. As shown in Fig. 1.2, the graphite structure consists of planes of covalently bonded carbon atoms which are held together by weak van der Waals-forces. This results in an in-plane bonding that

exceeds the interlayer bonding in strength by several orders of magnitude. This is also demonstrated by the in-plane bond length of 1.42 Å as compared to 3.35 Å for the interlayer bonds. The electric and thermal properties of graphite are highly anisotropic, because electrons and phonons can propagate much faster along the planes than from one plane to another. So, although it is 3D in nature, graphite can often be regarded as a (2+1)D material.

In the last decades, there has been an enormous expansion of the known carbon allotropes with the discovery of 0D fullerenes in 1985, 1D carbon nanotubes in 1991, and eventually 2D graphene in 2004. The last one, graphene, forms the basis of all these other graphitic allotropes (see Fig. 1.2) which makes it all the more curious that it has been discovered only recently. A possible explanation for this might be the fact that researchers for long believed it could not exist. Contrary to the case of fullerenes and nanotubes, which were predicted before their actual observation, 2D graphene was thought to be unstable at any finite temperature (see below).

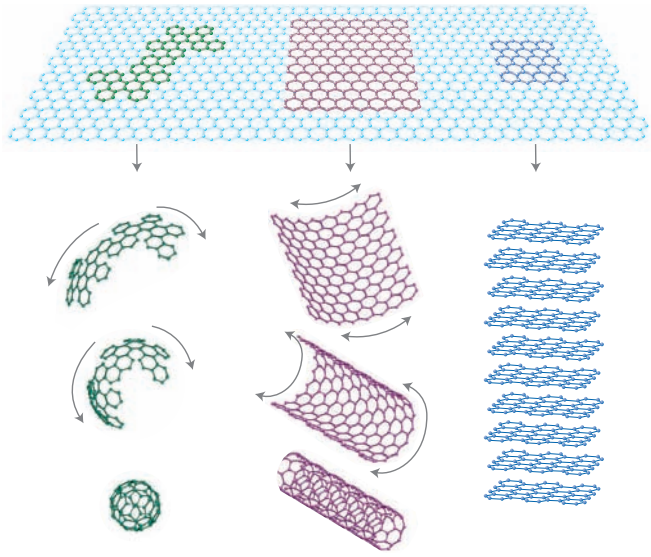

Figure 1.2. *Graphene forms the basis of the other graphitic carbon allotropes; from left to right: fullerenes (C_{60}), carbon nanotubes, and graphite. (Figure taken from ref. [3].)*

1.2.2 Fullerenes and carbon nanotubes

Fullerenes and (single-walled) carbon nanotubes can be thought of as rolled up monolayer graphene (see Fig. 1.2) and, consequently, many of their properties can be derived from those of graphene. Especially carbon nanotubes with large diameters can be considered as graphene to which periodic boundary conditions are applied in the direction perpendicular to the tube axis. Therefore a great deal of the results obtained for graphene in this thesis can also be extrapolated to these systems.

1.3 Graphene: the non-existing material

It has been a widely accepted belief that monolayers of graphene could not exist because these materials are two-dimensional. More than 70 years ago Peierls [4] and Landau [5] showed that a divergent contribution of thermal fluctuations in all low-dimensional crystals induces displacements of atoms that are comparable to the interatomic distances at any finite temperature. Therefore strictly 2D crystals are thermodynamically unstable and can not exist. Experimental observations of a decreasing melting temperature for films with a decreasing thickness seemed to provide strong support for this theory. It came therefore as a surprise when, in 2004, several 2D materials were observed by Geim *et al.* at Manchester University [1]. Among these 2D materials were graphene, the structurally similar boron nitride, and others, but only graphene has been intensively studied till now. There has been a long debate on the cause of the apparent stability of graphene monolayers but there seems to have emerged a consensus that the 2D crystals become intrinsically stable by a soft crumpling in the third dimension (see Fig. 1.3). This crumpling has been observed on a lateral scale of approximately 10 nm and is believed to suppress thermal vibrations [6]. An alternative explanation is found when one considers the graphene layer as extracted from a 3D material (graphite) which is kept in its metastable state by (van der Waals) interaction with a supporting substrate and the strong in-plane bonds which prevent the formation of defects.

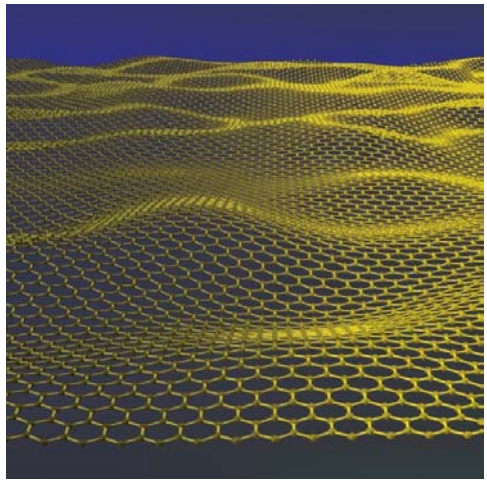

Figure 1.3. *Simulated model for the crumpling of a graphene monolayer in the third dimension. (Figure from Ref. [3] (journal cover).)*

Chapter 2

Graphene: Synthesis and Electronic Properties

A variety of factors can change the properties of graphene because of its two-dimensional nature. As will be shown in the next section, the preparation mode is one of the key factors on which these properties depend. But first I will describe some of the most important electronic and mechanical properties of (perfect) monolayers of graphene.

2.1 Electronic properties

2.1.1 Dirac particles in graphene

The electronic properties of graphene are well described by the electronic structure of a perfect, flat, freestanding and infinite graphene crystal in vacuum[1]. Such an idealized case can be treated theoretically and can therefore provide a lot of insight. The results of several theoretical approximations for the electronic band structure and the density of states are shown in Fig. 2.1. These were calculated with density functional theory (DFT), first-neighbor tight-binding (TB) involving only p_z atomic orbitals, and the Dirac-Weyl equation (i.e. the Dirac equation for massless fermions), respectively. The details of these theoretical calculations are given in the next chapter because here we are only concerned with the results.
The DFT-calculations are the most accurate ones, but it can be seen from the figure that the TB-approximation gives a (qualitatively) correct description of the valence and conduction bands. For small excitations (<2eV) from the Fermi-level

[1]This is an idealization in several ways since every 'real' system has defects and ripples and is supported in some way or the other (and of course it is finite and not in vacuum).

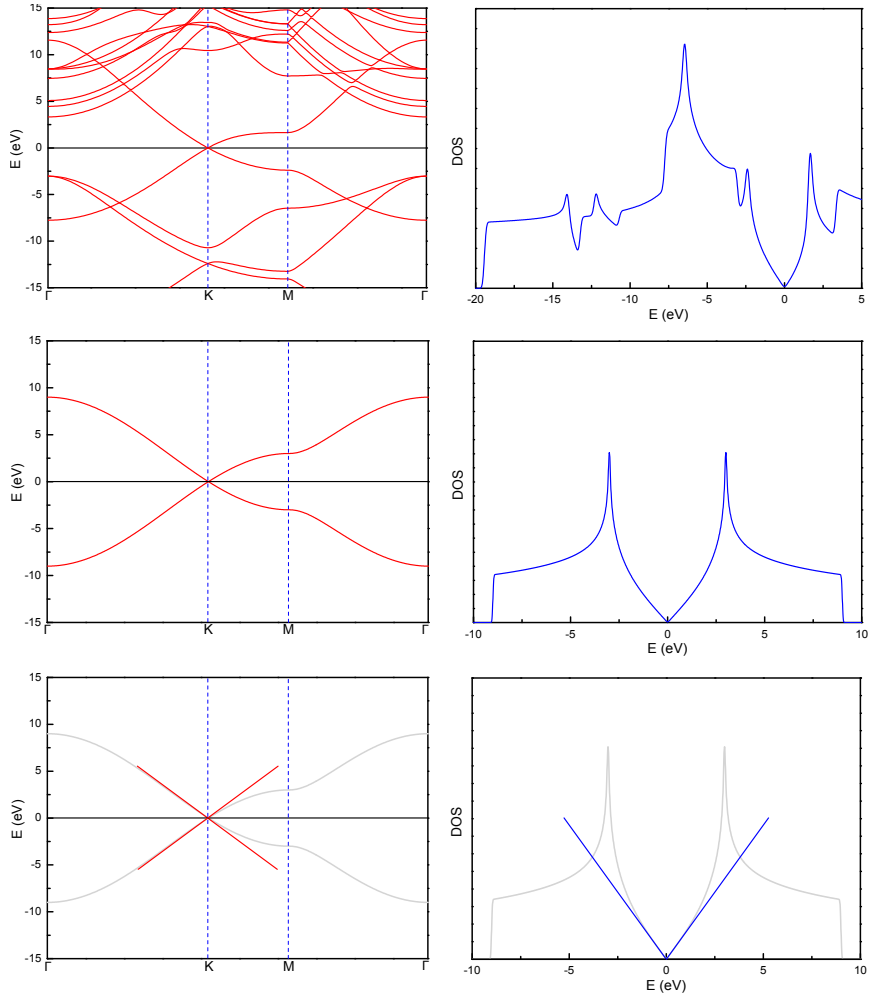

Figure 2.1. *The electronic band structure (left) and the density of states (right) for intrinsic graphene, calculated with different theoretical models: (a) density functional theory, (b) nearest-neighbour tight-binding, and (c) Dirac theory (QED) for massless fermions. The Fermi-energy is set to zero.*

of the neutral system a good description is provided by a linear spectrum which can be deduced from a 2D Dirac-Weyl hamiltonian,

$$H \approx \hbar v_F \begin{pmatrix} 0 & p_x - ip_y \\ p_x + ip_y & 0 \end{pmatrix} = \hbar v_F \sigma \cdot \mathbf{p}, \tag{2.1}$$

where v_F denotes the Fermi velocity (a constant) and σ represents the 2D vector of Pauli matrices, (σ_x, σ_y). The Fermi velocity is isotropic for small excitations and can be measured or calculated to be $v_F \approx 1.10^6 ms^{-1}$. This is about 300 times

smaller than the velocity of light in vacuum. The point in the energy spectrum that coincides with the Fermi-level of the neutral system is called the Dirac point, but this name is also used for the corresponding point in reciprocal space (usually the K-point) of the hexagonal lattice. The DOS is zero at the Dirac point, but at the same time there is no gap in the band structure so that graphene is actually a zero gap semiconductor.

2.1.2 Ambipolar electric field effect

An interesting consequence of the unique electronic spectrum of graphene is the possibility to change the amount and type of charge carriers continuously from electrons to holes through the application of a homogeneous electric field perpendicular to the graphene sample. The electric field shifts the Fermi-level up and down and is therefore capable of inducing both electrons or holes in graphene. In Fig. 2.2 the experimental confirmation of this ambipolar electric field effect is demonstrated by resistivity measurements under varying gate voltages.

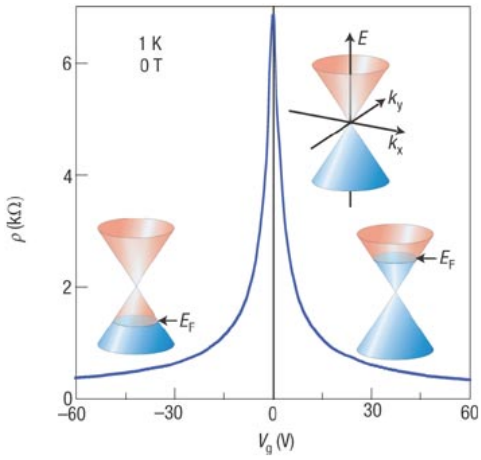

Figure 2.2. *Experimental observation of the ambipolar electric field effect in monolayer graphene on a SiO_2 substrate. The insets show the conical low-energy spectrum with different positions of the Fermi-energy, E_F, corresponding to negative, zero, and positive gate voltages, V_g, respectively.(Taken from ref. [3].)*

2.1.3 Klein tunneling

Another surprising consequence of the Dirac-Weyl nature of the charge carriers in graphene is the fact that they can tunnel without reflection through potential barriers for normal incidence [7]. This can be understood when the influence of the

potential is regarded as a local shift of the Fermi-level of the system (see Fig. 2.3). The Dirac-particle changes its nature from electron to hole (or vice versa) in the barrier so that it can go through without scattering. This strange behavior of the

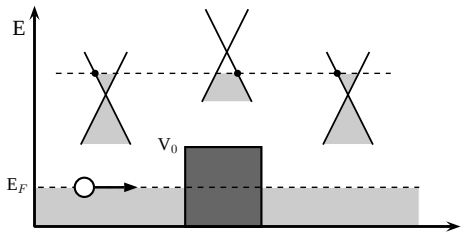

Figure 2.3. *Klein-tunneling in graphene: an electron state outside the barrier can tunnel without reflection through the barrier as a hole state.*

charge carriers has both advantages and disadvantages for practical applications of graphene in electronics: the reduced scattering makes quasi-ballistic transport possible but, on the other hand, it is very difficult to constrain the carrier flow by potential barriers. Furthermore, it is impossible to 'switch off' the conductivity of graphene devices (see below) which is an important requirement for some electronic applications such as field effect transistors.

2.1.4 Minimum conductivity

As can be seen from Fig. 2.2, the resistivity remains finite, even at vanishing gate voltage. Since the density of states is zero at this point (see Fig. 2.1), this means there is a non-vanishing conductivity although there appear to be no charge carriers in graphene. The Dirac spectrum of intrinsic graphene leads to the prediction of a universal ballistic conductivity in the zero-carrier regime which has, however, not been observed experimentally. Instead, experimental measurements of the minimal conductivity find a sample-dependent minimum which is approximately a factor of π larger than the theoretical predicted value. The commonly accepted solution to this problem ascribes this minimum conductivity to randomly distributed electron-hole puddles caused by inhomogeneities in the environment of the sample (such as ripples and defects in the substrate) [8]. The different electron and hole puddles are not isolated, because of the Klein tunneling, which makes sure that there is always a finite amount of possible charge carriers present in graphene.

2.1.5 Creating a band gap

The minimal conductivity caused by the Dirac-Weyl nature of the electronic band structure is a major drawback for most applications in electronics (see below).

This problem should be solved if one can induce a gap in the band spectrum. This can be done in several ways: confining the electrons in one direction by cutting stripes (nanoribbons) from a graphene layer or applying a potential difference over a bilayer of graphene can lead to the opening of an appreciable band gap. Another possibility is to create a gap by chemical modification of the graphene layer. When radicals such as atomic oxygen, hydrogen or fluorine are adsorbed to the graphene surface they form covalent bonds with the carbon atoms. To make these covalent bonds possible, the carbon atoms change their hybridization from sp^2 to sp^3 which leads to the opening of a band gap (similar as in diamond). This last possibility is further examined in Chapter 12.

2.2 Mechanical properties

The mechanical properties of graphene are also remarkable. Graphene is the strongest material ever measured with a Young's modulus of about 1 TPa, but at the same time it is very soft and can take the form of the underlying substrate.[2] The mechanical properties of graphene and some related materials will be treated later in this thesis, so I will not go into detail here.

2.3 Graphene sample preparation

2.3.1 Introduction

The 2D nature of graphene causes it to be exposed completely to the environment, i.e. every carbon atom of the graphene crystal is capable of interacting with the surroundings. Most graphene samples are grown or deposited on a substrate with which they interact while the other side of the graphene sheet is exposed to an atmosphere or vacuum. Variations in the nature of the substrate or atmosphere lead to a wide variety of electronic properties of the graphene sample. E.g. the type of charge carriers in graphene, electrons or holes, depends strongly on the environment.

Consequently, it is very important to know the different experimental circumstances and preparation methods for graphene. However, these experimental circumstances are still a subject of debate and the preparation methods are evolving at an increasingly high pace. In this section an attempt is made to give an overview of the most common preparation methods so far. The possible environmental influences are treated later when necessary.

[2] This issue appears to be still rather controversial and is highly dependent on the type of underlying substrate.

Two major classes of preparation techniques can be distinguished; those that start from graphite and in a variety of ways try to isolate few layer graphene (FLG) and ultimately monolayers (top-down approach), and those in which the graphene is actually synthesized out of some non-related materials that contain carbon atoms (bottom-up). Techniques of the first class will be called exfoliation methods, while the second class of techniques will be referred to as synthesis methods.

2.3.2 Exfoliation methods

The layered structure of graphite in which there is strong (covalent) bonding between the carbon atoms in a plane and weak van der Waals-bonding between the different planes, suggests an easy route to produce graphene by breaking the weak interlayer bonding and separate the different planes. However, several difficulties with this procedure might be expected: how can this separation be done in a controllable way so that different samples contain the same number of layers, and how can the layers be kept apart after separation? The importance of these problems depends strongly on the actual technique that is used to produce the FLG.

Mechanical exfoliation

Mechanical exfoliation is the preparation method that lead to the very first isolation of a graphene sample [1]. Besides its historical importance, mechanical exfoliation is still extremely valuable. Especially in academic research it is a widely applied technique because the resulting sample quality is still unequaled by any of the more recent techniques. The conceptual simplicity of this technique, which is also referred to as the 'scotch-tape method', makes it surprising that it took so long to discover single layer graphene samples. Essentially, the whole preparation process consists of the repeated peeling of a multilayered graphitic material of a highly ordered pyrolytic graphite (HOPG) crystal with a celluphene tape and, subsequently, pressing the tape on a Si/SiO_2 substrate to deposit the (few-layered) graphene samples. The SiO_2 of the substrate must have a carefully chosen thickness (~ 300 nm) to enhance the optical contrast of a single layer of graphene by an interference effect. With an optical microscope it is then possible to distinguish between monolayer graphene and the many multilayered graphitic materials, left behind on the substrate after removal of the tape. The size of the samples produced this way is of the order of several μm^2, but putting a polymer coating on the substrate can increase the adhesion of the graphene sheets thereby allowing the production of larger (mm^2) pieces.
The graphene samples produced by mechanical cleavage have very good electronic quality and are essentially free of defects, but there are some serious problems that are difficult to overcome. It seems impossible to use this method for mass production because there is no control over the number of layers. The monolayers

of graphene are produced among a myriad of FLG's and have to be searched for with an optical microscope, so it is difficult to imagine how this could ever become a high-throughput method for industrial applications. Therefore other techniques are needed for these applications.

Chemical exfoliation

A more recent technique for graphene production is to separate the individual sheets in graphite with a solution-based process (for a review see ref. [9]). This method makes use of an intermediate step in which graphite is chemically modified to make it water dispersible. One way is to oxidize graphite to graphite oxide (GO) which can be intercalated with water to separate the layers (see Fig. 2.4). However it is graphene that is wanted not GO, therefore it is necessary to reduce the GO again to graphene. This can be done by thermal annealing or chemical reduction in solution. The problem with chemical reduction in solution is that the different layers quickly aggregate after reduction since they are no longer soluble. This is a problem that seems difficult to overcome. Another way is thermal reduction after the solution is deposited by spray coating on a heated substrate like SiO_2.

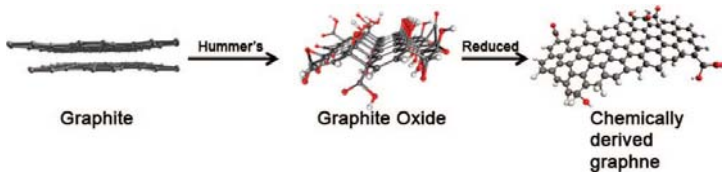

Figure 2.4. *Molecular model for the conversion of graphite to chemically derived graphene through oxidation/reduction process (from ref. [10]).*

The main advantage of chemical exfoliation is that it is low cost and has massive scalability. But the quality of the samples is very low because a lot of defects are introduced in the oxidation/reduction process.

2.3.3 Synthesis methods

The other strategy to produce graphene is from the bottom up by 'gluing together' precursor organic molecules or carbon atoms. This can be done in many ways and the various methods are evolving very fast. But it is possible to distinguish between three different approaches: organic synthesis in solution, chemical vapor deposition on a metal substrate, and thermal decomposition of a silicon carbide substrate.

Organic synthesis

The synthesis of planar benzene-based macromolecules from polycyclic aromatic hydrocarbons (PAH) is a research field that dates back from long before the discovery of graphene. But the field is now attracting renewed interest as a possible route to graphene. The macromolecules are synthesized in solution. This restricts their size because increasing the weight of a macromolecule decreases the solubility and enhances the formation of more 3D-like structures. However in 2008 it was demonstrated that graphene nanoribbons with lengths of about 12 nm could be produced this way [11]. With further development this might become an attractive route to graphene for electronic applications.

Epitaxial graphene on silicon carbide

Another technique, which is perhaps one of the most promising techniques for large-scale graphene production, is to extract graphene layer by layer from a silicon carbide (SiC) crystal surface by controlled heating in vacuum or a suitable oxygen-containing atmosphere. A lot of theoretical and experimental work has been performed to identify the processes behind the graphene formation on the SiC surface and this has resulted in a reasonable understanding of the important factors involved [12]. The most decisive factor for the properties of the produced graphene multilayers is the surface from which it is extracted.

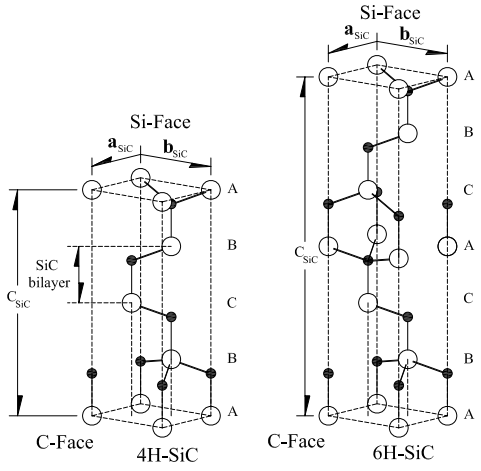

Figure 2.5. *Crystal structure of 4H-SiC and 6H-SiC. Filled circles are carbon atoms and open circles are silicon atoms. The Si-face and C-face are indicated. (Taken from ref. [12].)*

The most used crystal types for the SiC are 4H-SiC and 6H-SiC (see Fig. 2.5). These are hexagonal lattices that have two different polar faces along the c-axis. When taking a finite slab of these crystals, this results in two inequivalent surfaces, (0001) and $(000\bar{1})$, which are respectively Si-terminated and C-terminated. The growth of graphene on these surfaces comes about when the Si atoms are evaporated from the surface. The Si atoms bind to oxygen to form SiO molecules and desorb from the surface. The C atoms are left behind and they reconstruct to form graphene layers. The graphene layer closest to the SiC is called the buffer layer and it is chemically bonded to the Si or C atoms of the substrate so that π-bands are absent in the electronic spectrum of this layer (see Fig. 2.5). The following layers exhibit the Dirac spectrum typical for freestanding graphene. But, depending on the growth side, the graphene samples are n-doped (Si-face) or slightly p-doped (C-face), as shown in Fig. 2.6.

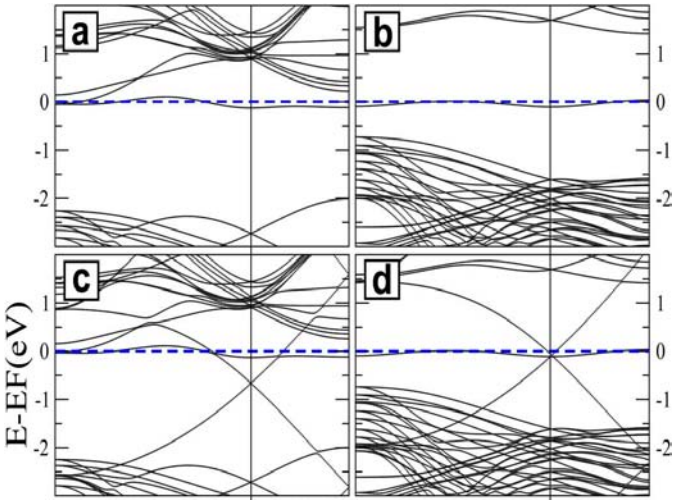

Figure 2.6. *Electronic band structure for graphene layers grown on the Si-face (a,c) and the C-face (b,d) of a SiC crystal. (a) and (b) show the band structure of the buffer layer, while (c) and (d) show the Dirac-like spectrum of the first true graphene layer (Taken from ref. [13].)*

Chemical Vapor Deposition

Maybe the most promising technique for the future is chemical vapor deposition. This technique can be described as the growing of graphene on a heated metallic substrate in a well-chosen atmosphere containing organic molecules. A lot of different substrates (Ni, Cu, Ru, ...) and atmospheres (CH_4/H_2, $CH_4/H_2/Ar$, ...) have already been examined, but there is still much room for improvement. There are

a lot of advantages of this method compared to the other ones: after etching away the substrate it is possible to transfer the graphene samples to any other substrate and, in principle, there is no limit on the size of the samples since they cover the whole substrate; another interesting consequence of this is the possibility to use prepatterned substrates to grow graphene samples with a well defined shape (see Fig. 2.7).

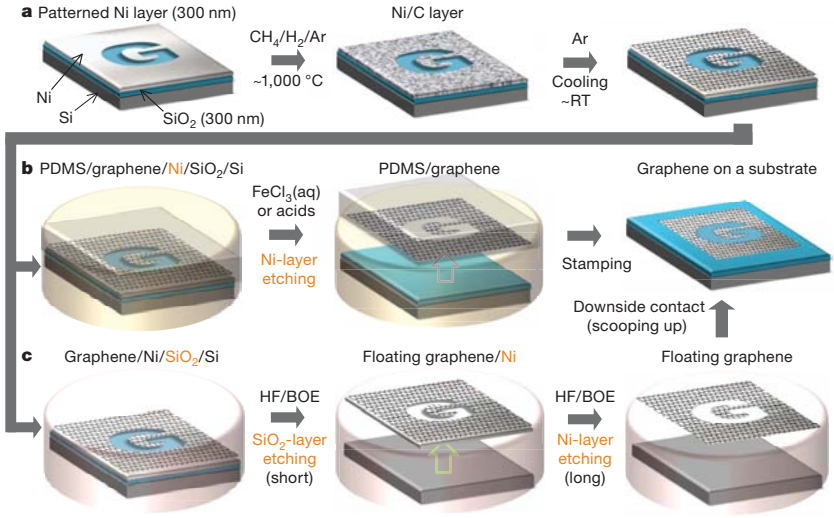

Figure 2.7. *a) Chemical vapor deposition of graphene on an patterned Ni layer. b,c) Etching with different techniques and subsequent transfer to another substrate.(Taken from ref. [14].)*

But for now there are still many problems: good ways to control the number of grown layers are still to be found and the presence of different growing centers induces polycrystalline samples which reduces the sample quality.

2.4 Applications

It is evident that the remarkable properties of graphene can lead to interesting new applications. These applications appear to be the subject of a lot of speculations, but some of these speculations are not so far from being realized anymore.

2.4.1 High-speed electronics

With the fundamental limitations of silicon-based electronics in sight, it is time to look for other materials to continue the advancement in electronic applications.

Graphene might be a good candidate because it obviously possesses many properties that make it interesting to use in electronics: it has high mobility charge carriers, even at high carrier concentrations, and exhibits ballistic transport on a submicrometer level, even at room temperature. However, the actual use of graphene in practical electronics is still very limited.

2.4.2 Transparent electrodes

Indium tin oxide (ITO) is the most used material these days for the fabrication of conducting coatings for liquid crystal displays (LCD), solar cells and the like. However, the high cost, limited resources, and brittle nature of ITO greatly restrict its application. The exceptional chemical and mechanical stability of graphene combined with its high conductivity, atomic layer thickness and essentially unlimited supply, make it an ideal candidate to replace ITO and become the leading material for transparent conducting electrode applications. Furthermore graphene is much more flexible and is therefore also a good material to use in touch screens etc. The applicability of graphene for this kind of usage has already been demonstrated [14].

2.4.3 Sensors

The small dimensions of graphene make it very sensitive to external influences. This is a useful property for sensor applications and allows one to transform graphene samples into nanosensors.

Mass sensors

Graphene can be made into a free-hanging, suspended membrane by (partially) etching away the SiO_2 substrate or deposition on a prepatterned substrate with holes into it. As such it can be made in a high-frequency resonator of which the frequency is highly dependent on any adsorbed species. The slightest mass differences can be detected in this way because of the low mass density of graphene.

Gas sensors

A new generation of gas sensors has recently emerged with the advent of carbon nanotubes and semiconductor nanowires. Because of the small dimensions of these materials, the charge carrier concentrations that result from adsorbed gas molecules can lead to detectable signals. The usual way to do this is by using these nanomaterials in a field effect transistor (FET) device in which the adsorbing molecules play the role of the gate voltage. The induced resistivity changes can be measured and in this way an exceptional sensitivity is achieved allowing the detection of toxic gases in concentrations of the order of one part per billion (p.p.b.).

Graphene can be regarded as the most recent member of this new generation of gas sensors but it has some superior properties that increase the sensitivity even further.

- Graphene is a 2D material and has, consequently, its whole volume exposed to possible adsorbates.
- Graphene is highly conductive and has therefore low Johnson-noise[3] even in the absence of charge carriers.
- In its neutral state, there are no charge carriers in graphene so that a few charge carriers can cause notable changes in the carrier concentration and hence the conductivity.
- Graphene crystals are almost defect-free which ensures decreased noise due to thermal movement of defects.

The combination of all these features allows for the ultimate detection of single molecular adsorption events with graphene sensors [15].

The usability of graphene for gas sensors has been demonstrated [15], but a lot of research still needs to be done to understand all the processes involved in the sensing mechanism. A great part of this thesis is concerned with the theoretical investigation of the interaction between adsorbates and graphene which might be useful for this kind of applications. Properties such as binding energies and charge transfers between molecules and graphene layers will be examined by simulating the adsorbate-graphene system within the density functional theory formalism.

[3] Johnson noise is the electronic noise generated by the thermal agitation of charge carriers.

Part II

Methodology

Chapter 3

General Introduction

In this part, I will cover all the theoretical methods that are used in the following. The knowledge of these theories in not always necessary to understand the results that are achieved with them, but they are included for completeness. One exception is the qualitative molecular orbital theory (section 4.3) which is used to interpret a lot of the results and is therefore required to understand the conclusions.

3.1 The Schrödinger equation

To get a better understanding of the adsorption properties of graphene, a good theoretical model is very useful. This model should at least be quantum mechanical since we are dealing with interactions at the atomic and molecular level, but relativistic effects can be neglected for the low mass atoms which we are concerned with in this thesis. Most of the properties of interest here can be deduced from static, i.e. time-independent, situations. In conclusion, our model needs to start from the non-relativistic, time-independent Schrödinger equation which, from now on, will be simply referred to as the Schrödinger equation.

The problem is now to find solutions for this Schrödinger equation. Suppose the system under study consists of N electrons and M nuclei, so the Schrödinger equation can be written as

$$\hat{H}_{tot}\Psi(\mathbf{x}_1, ..., \mathbf{x}_N, \mathbf{R}_1, ..., \mathbf{R}_M) = E_{tot}\Psi(\mathbf{x}_1, ..., \mathbf{x}_N, \mathbf{R}_1, ..., \mathbf{R}_M), \tag{3.1}$$

where the coordinates $\mathbf{x}_i$ represent both the position coordinates, $\mathbf{r}_i$, and the spin coordinates, σ_i, of the N electrons and the coordinates $\mathbf{R}_I$ are the position coordinates of the M atomic nuclei in the system. The hamiltonian operator, $\hat{H}$, is given

by

$$\begin{aligned}\hat{H}_{tot} &= -\frac{\hbar^2}{2m_e}\sum_i^N \nabla_i^2 - \sum_I^M \frac{\hbar^2}{2M_I}\nabla_I^2 - \sum_i^N\sum_I^M \frac{Z_I e^2}{|\mathbf{r}_i - \mathbf{R}_I|} \\ &\quad + \frac{1}{2}\sum_{i\neq j}^N \frac{e^2}{|\mathbf{r}_i - \mathbf{r}_j|} + \frac{1}{2}\sum_{I\neq J}^M \frac{Z_I Z_J e^2}{|\mathbf{R}_I - \mathbf{R}_J|}, \end{aligned} \tag{3.2}$$

where m_e is the mass of an electron and M_I and Z_I are respectively the mass and the charge (atomic number) of the nuclei. The first and the second term of equation (3.2) correspond to the kinetic energies of the electrons and nuclei, while the others represent the electron-nucleus, electron-electron, and nucleus-nucleus Coulomb interaction terms respectively.
It is clear that finding the ground state solution of the Schrödinger equation (3.1) with the hamiltonian given by (3.2) is not an easy task. In fact, it is impossible to solve this equation exactly but for the simplest problems such as the hydrogen atom. However, it is possible to make a number of approximations to this equation, based on physical arguments, so that approximate solutions are feasible.

3.2 The Born-Oppenheimer or adiabatic approximation

A first approximation can be made when considering the large difference in mass between electrons and nuclei. The lightest nucleus, the proton, weighs approximately 1800 times more than an electron and for carbon atoms this ratio is already about 22000. This means that the kinetic energy of the nuclei (the second term in (3.2)), which is inversely proportional with the nuclear mass M_I, is relatively small and can be neglected. Consequently, the nuclei can be considered as frozen and the nucleus-nucleus repulsion term becomes merely a constant. Taking this into account, the hamiltonian can be rewritten as

$$\hat{H}_{tot} \simeq \hat{H}_e + E_{nuc}, \tag{3.3}$$

with

$$\hat{H}_e = -\frac{\hbar^2}{2m_e}\sum_i^N \nabla_i^2 + \frac{1}{2}\sum_{i\neq j}^N \frac{e^2}{|\mathbf{r}_i - \mathbf{r}_j|} - \sum_i^N\sum_I^M \frac{Z_I e^2}{|\mathbf{r}_i - \mathbf{R}_I|} \tag{3.4}$$

$$E_{nuc} = \frac{1}{2}\sum_{I\neq J}^M \frac{Z_I Z_J e^2}{|\mathbf{R}_I - \mathbf{R}_J|}. \tag{3.5}$$

It is now possible to solve the electronic part (3.4) separately using the nuclear coordinates as parameters, and then add the nuclear repulsion part (3.5) to get

the total energy. When looking for the ground state of the system, the nuclear positions can be changed until the total energy minimum has been reached (see next section).
Because the nuclear repulsion energy is easily calculated, only equation (3.4) is of real interest now. For convenience in notation I will simply refer to $\hat{H}_e$ as $\hat{H}$ and define $\hbar = e = m_e = 1$ to get rid of all the constants in our notation (i.e. we switch to atomic units), so that

$$\hat{H} = \underbrace{-\frac{1}{2}\sum_{i}^{N}\nabla_i^2}_{\hat{T}} + \underbrace{\frac{1}{2}\sum_{i\neq j}^{N}\frac{1}{|\mathbf{r}_i - \mathbf{r}_j|}}_{\hat{V}_{ee}} \underbrace{-\sum_{i}^{N}\sum_{I}^{M}\frac{Z_I}{|\mathbf{r}_i - \mathbf{R}_I|}}_{\hat{V}_{ext}} \tag{3.6}$$

and the energy is expressed in hartree (1 hartree = 27.21138 eV) and lengths in bohr (1 bohr = 0.529177 Å). Note that the hamiltonian (3.6) is completely determined by the number of electrons N, and the positions $\{\mathbf{R}_I\}$ and charges $\{Z_I\}$ of the nuclei. Or, stated in another way, the hamiltonian is entirely specified through the third term on the right in (3.6), i.e. the term originating from the nuclear potentials, while the first two terms can be considered universal.
A consequence of applying the adiabatic approximation to the hamiltonian (3.2) is the removal of the nuclear coordinates from the many particle wavefunction as given in (3.1). The total energy is given by

$$E_{tot} = \langle \hat{H}_{tot} \rangle \simeq \langle \hat{H} \rangle + E_{nuc} = \langle \hat{T} \rangle + \langle \hat{V}_{ee} \rangle + \langle \hat{V}_{ext} \rangle + E_{nuc}, \tag{3.7}$$

where the expectation values are taken with respect to $\psi(\mathbf{x}_1, ..., \mathbf{x}_N)$. This does not mean that the energy is independent of the nuclear coordinates, but that the interaction of the electrons with the nuclei is only included as an interaction with the external potential $V_{ext}(\mathbf{r}) = \sum_I \frac{Z_I}{|\mathbf{r}-\mathbf{R}_I|}$.

3.3 The force theorem

Suppose that it would be feasible to find the exact ground state wavefunction, $\psi_0(\mathbf{x}_1, ..., \mathbf{x}_N)$, for any given set of nuclear coordinates $\{\mathbf{R}_I\}$. Is it possible in this case to find that particular set of nuclear coordinates that minimizes the total energy (3.7)? After all, it does not seem possible to check all sets of coordinates and then pick the one with the lowest energy. However, if we can calculate the forces on the nuclei we can move them according to classical mechanics until all forces on them vanish,[1] i.e.

$$\mathbf{F}_I = -\frac{\partial E_{tot}}{\partial \mathbf{R}_I} = 0 \qquad \text{for} \quad I = 1, ..., M. \tag{3.8}$$

[1] This only ensures we reach a local minimum, of course.

For the calculation of these forces we can apply the force theorem stated by Hellmann[16] and Feynman[17]: an evaluation of the forces from (3.7) gives

$$-\frac{\partial E_{tot}}{\partial \mathbf{R}_I} = -\langle \frac{\partial \psi_0}{\partial \mathbf{R}_I} | \hat{H} | \psi_0 \rangle - \langle \psi_0 | \frac{\partial \hat{H}}{\partial \mathbf{R}_I} | \psi_0 \rangle - \langle \psi_0 | \hat{H} | \frac{\partial \psi_0}{\partial \mathbf{R}_I} \rangle - \frac{\partial E_{nuc}}{\partial \mathbf{R}_I}. \tag{3.9}$$

The first and the third term on the right vanish because of the variation principle. So we get

$$\begin{aligned} \mathbf{F}_I &= -\langle \psi_0 | \frac{\partial \hat{H}}{\partial \mathbf{R}_I} | \psi_0 \rangle - \frac{\partial E_{nuc}}{\mathbf{R}_I} \\ &= -\langle \frac{\partial \hat{T}}{\partial \mathbf{R}_I} \rangle - \langle \frac{\partial \hat{V}_{ee}}{\partial \mathbf{R}_I} \rangle - \langle \frac{\partial \hat{V}_{ext}}{\partial \mathbf{R}_I} \rangle - \frac{\partial E_{nuc}}{\partial \mathbf{R}_I} \\ &= -\langle \frac{\partial \hat{V}_{ext}}{\partial \mathbf{R}_I} \rangle - \frac{\partial E_{nuc}}{\partial \mathbf{R}_I} \\ &= -\int d\mathbf{r} \rho_0(\mathbf{r}) \frac{\partial V_{ext}(\mathbf{r})}{\partial \mathbf{R}_I} - \frac{\partial E_{nuc}}{\partial \mathbf{R}_I} \end{aligned} \tag{3.10}$$

with the ground state electron density, $\rho_0(\mathbf{r})$, defined as

$$\rho_0(\mathbf{r}) = N \int |\psi_0(\mathbf{x}_1, ..., \mathbf{x}_N)|^2 d\sigma_1 d\mathbf{x}_2 ... d\mathbf{x}_N, \tag{3.11}$$

So the forces on the nuclei only depend on the ground state density and the positions of the other nuclei and can be calculated if the wavefunction (or electron density) is known.

Chapter 4

Approximate Solutions

Now that we know that it is possible to find the total ground state solution if we are capable of finding the (electronic) ground state solutions for fixed nuclear configurations, our problem is reduced to finding these electronic ground state solutions. For this it is useful to introduce some additional approximations.

4.1 The variation principle and finite basis sets

It is still an impossible task to find any eigenfunction of the hamiltonian operator, but suppose all the (many-body) eigenfunctions $\{\phi_i\}$ were known. The set of these eigenfunctions is complete and can be chosen to be orthonormal. It is then possible to write any wavefunction ψ (with the same number of electrons) formally as $\psi = \sum_i c_i \phi_i$ and the expectation value for the energy of this wavefunction[1] is then

$$E = \langle\psi|\hat{H}|\psi\rangle = \sum_{i,j} c_j^* c_i \langle\phi_j|\hat{H}|\phi_i\rangle = \sum_i |c_i|^2 E_i \geq E_0 \sum_i |c_i|^2 = E_0, \qquad (4.1)$$

with E_0 the lowest eigenvalue of $\hat{H}$, i.e. the ground state energy. The expectation value of the energy of any wavefunction ψ is thus higher than or equal to the ground state energy. This is a very important result because this allows us to search for the ground state wavefunction and energy by testing different 'trial wavefunctions' and taking the state corresponding to the lowest energy as the best approximation for the true ground state.
The problem is now to find good trial wavefunctions. It is often clear from the system under study what the wavefunctions should look like. Based on this insight, a particular wavefunction $\Psi(\mathbf{x}; p_1, p_2, ..., p_n)$, depending on a finite number

[1] The wavefunction is assumed to be normalized.

of parameters $\{p_i\}$, can be proposed. In that case, the expectation value for the energy, E, is a function of these parameters and can be minimized with respect to them by requiring that

$$\frac{\partial E}{\partial p_1} = \frac{\partial E}{\partial p_2} = ... = \frac{\partial E}{\partial p_n} = 0. \tag{4.2}$$

In practice, it can be very useful to define a finite basis set of (often orthonormal) functions, $\{\chi_j\}$, and search for solutions that are linear combinations of these basis functions,

$$\phi = \sum_j^{N_b} c_j \chi_j, \tag{4.3}$$

through the variation of the (finite) set of coefficients $\{c_j\}$, while keeping the basis functions fixed. The approximate ground state corresponds to the best linear combination of the basis functions and is obtained when

$$\frac{\partial}{\partial c_j^*} \frac{\langle\phi|\hat{H}|\phi\rangle}{\langle\phi|\phi\rangle} = 0 \tag{4.4}$$

for all c_j. Introducing a Lagrange multiplier λ, we can rewrite this as

$$\frac{\partial}{\partial c_j^*} \Big(\langle\phi|\hat{H}|\phi\rangle - \lambda(\langle\phi|\phi\rangle - 1) \Big) = 0. \tag{4.5}$$

and after substitution of the wavefunction (4.3) into (4.5), we get

$$\sum_j c_j \Big(\langle\chi_i|\hat{H}|\chi_j\rangle - \lambda\langle\chi_i|\chi_j\rangle \Big) = 0. \tag{4.6}$$

This can be cast in the form of a generalized eigenvalue equation,

$$\sum_j H_{ij} c_j = \lambda \sum_j S_{ij} c_j, \tag{4.7}$$

with $H_{ij} = \langle\chi_i|\hat{H}|\chi_j\rangle$ and $S_{ij} = \langle\chi_i|\chi_j\rangle$. These N_b equations ($i = 1, ..., N_b$) can be solved once the matrix elements H_{ij} and S_{ij} are calculated. From the N_b solutions the one with the lowest expectation value for the energy is the best approximation of the ground state. After multiplying (4.6) with c_i^* and summing over i we find

$$\lambda = \frac{\sum_{i,j} c_i^* c_j \langle\chi_i|\hat{H}|\chi_j\rangle}{\sum_{i,j} c_i^* c_j \langle\chi_i|\chi_j\rangle} \tag{4.8}$$

i.e. λ corresponds with the expectation energy, so the solution of (4.7) with the lowest eigenvalue is the sought-after approximation.
In the following sections a few specific examples are given of special basis sets that will be helpful in analyzing some of the results of more advanced calculations.

4.2 Independent particles: the Hartree-Fock approximation

A major problem with trying to solve the many-body Schrödinger equation is the representation of the many-body wavefunction. Imagine the amount of information needed to describe the many-body wavefunction of a system containing 10 electrons. Suppose we want to represent each electron numerically on a very coarse grid of 10^3 points (3D), then $(10^3)^{10} = 10^{30}$ values are needed to represent the many-body wavefunction at the same level of accuracy. One solution to this problem is to look at the different electrons as independent of one another, with the consequence that, in our example, only $10 \times (10^3) = 10^4$ values are needed to represent the wavefunction. This approximation, known as the Hartree-Fock approximation, is relatively crude, of course, but it has the advantage that it gives an intuitive picture of electrons occupying different orbitals[2]. Furthermore this approximation forms the basis of the, in principle, exact configuration interaction theory. However, this is not the reason for including the Hartree-Fock theory here: the HF approximation will not be used in any of the performed calculations but it is very important for a good understanding of the Kohn-Sham approach to density functional theory which will be used extensively. Therefore the emphasis here will be on the introduced concepts.

Assuming that the different electrons of the system under study can be represented occupying different orbitals, Hartree proposed a wavefunction of the form $\psi_H(\mathbf{x}_1, ..., \mathbf{x}_N) = \phi_1(\mathbf{x}_1)\phi_2(\mathbf{x}_2)...\phi_N(\mathbf{x}_N)$, with the (single-particle) orbitals $\{\phi_i(\mathbf{x}_i)\}$ unspecified (but they are usually chosen to be orthonormal)[18]. It was soon realized by Slater [19] and Fock [20] that this could easily be improved upon by enforcing the Pauli exclusion principle on ψ_H, i.e.

$$\psi_{HF}(\mathbf{x}_1, ..., \mathbf{x}_N) = \frac{1}{\sqrt{N!}} \sum_{i}^{N!} (-1)^{P(i)} P_i\{\phi_1(\mathbf{x}_1)\phi_2(\mathbf{x}_2)...\phi_N(\mathbf{x}_N)\}, \tag{4.9}$$

where the sum is over all the different permutations of the orbitals $\{\phi_i\}$. Wavefunctions of the form (4.9) have the correct fermion behavior when any two electrons are interchanged, i.e they change sign, and they are known as Slater-determinants. We can now use this wavefunction as a trial wavefunction for our hamiltonian

$$\hat{H} = -\frac{1}{2}\sum_{i}^{N} \nabla_i^2 - \sum_{i}^{N}\sum_{I}^{M} \frac{Z_I}{|\mathbf{r}_i - \mathbf{R}_I|} + \frac{1}{2}\sum_{i\neq j}^{N} \frac{1}{|\mathbf{r}_i - \mathbf{r}_j|} \tag{4.10}$$

$$\equiv \sum_{i}^{N} \hat{h}_1(\mathbf{r}_i) + \frac{1}{2}\sum_{i\neq j}^{N} \hat{h}_2(\mathbf{r}_i, \mathbf{r}_j), \tag{4.11}$$

[2]Actually they are spin orbitals, but I will just call them orbitals.

with the single-particle operator $\hat{h}_1$ and the two-particle operator $\hat{h}_2$ defined as

$$\hat{h}_1(\mathbf{r}_i) = \frac{1}{2}\nabla_i^2 + \sum_I^M \frac{Z_I}{|\mathbf{r}_i - \mathbf{R}_I|}, \quad \text{and} \quad \hat{h}_2(\mathbf{r}_i, \mathbf{r}_j) = \frac{1}{|\mathbf{r}_i - \mathbf{r}_j|}. \tag{4.12}$$

It is easy to show that for a Slater determinant with the additional constraint that $\langle\phi_i|\phi_j\rangle = \delta_{ij}$ we get

$$\begin{aligned}
\langle\hat{H}\rangle &= \langle\psi_{HF}|\sum_i^N \hat{h}_1(\mathbf{r}_i) + \frac{1}{2}\sum_{i\neq j}^N \hat{h}_2(\mathbf{r}_i, \mathbf{r}_j)|\psi_{HF}\rangle \\
&= \sum_i^N \langle\phi_i|\hat{h}_1(\mathbf{r}_i)|\phi_i\rangle + \frac{1}{2}\sum_{i\neq j}^N \Big(\langle\phi_i\phi_j|\hat{h}_2(\mathbf{r}_i, \mathbf{r}_j)|\phi_i\phi_j\rangle - \langle\phi_j\phi_i|\hat{h}_2(\mathbf{r}_i, \mathbf{r}_j)|\phi_i\phi_j\rangle\Big) \\
&\equiv \sum_i^N \langle\phi_i|\hat{h}_1(\mathbf{r}_i)|\phi_i\rangle + \frac{1}{2}\sum_{i,j}^N (J_{ij} - K_{ij})
\end{aligned} \tag{4.13}$$

On the last line the Coulomb interaction terms, J_{ij}, and the exchange terms, K_{ij}, are defined. The exchange terms result from imposing the antisymmetry on the wavefunction in (4.9), when interchanging two electrons. Note that the Coulomb terms also contain the non-physical self-interaction terms (for $i = j$) which are removed by the corresponding exchange terms.

Applying the variation principle to the different orbitals, i.e. $\phi_i \to \phi_i + \delta\phi_i$, we arrive at the Hartee-Fock equations,

$$\hat{F}_{HF}\phi_j = \epsilon_j\phi_j \qquad \text{for} \quad j = 1, 2, ..., N, \tag{4.14}$$

where $\epsilon_j, ..., \epsilon_N$ are the Lagrange multipliers, and the Fock operator $\hat{F}_{HF}$ is defined by

$$\hat{F}_{HF} = \hat{h}_1 + \sum_i^N (\hat{J}_i - \hat{K}_i). \tag{4.15}$$

So the many-body Schrödinger equation has been replaced by the single-particle Hartree-Fock equation of which the N lowest energy solutions can be combined into a Slater determinant to give the approximate many-body wavefunction. The interaction between the electrons occupying different orbitals is included in the Coulomb and exchange operators, $\hat{J}_i$ and $\hat{K}_i$, which will be discussed in more detail now.

The Coulomb operator

The Coulomb operator, $\hat{J}_i$, is defined by

$$\hat{J}_i\phi_j(\mathbf{x}_1) = \int \phi_i^*(\mathbf{x}_2)\hat{h}_2\phi_i(\mathbf{x}_2)\phi_j(\mathbf{x}_1)d\mathbf{x}_2 = \int \frac{|\phi_i(\mathbf{x}_2)|^2}{|\mathbf{r}_1 - \mathbf{r}_2|}d\mathbf{x}_2\ \phi_j(\mathbf{x}_1) \quad (4.16)$$

$$\Rightarrow \quad \hat{J}_i = \int \frac{|\phi_i(\mathbf{x}_2)|^2}{|\mathbf{r}_1 - \mathbf{r}_2|}d\mathbf{x}_2 \quad (4.17)$$

In other words, $\hat{J}_i$ corresponds to the classical electrostatic potential that an electron at position $\mathbf{r}_1$ feels due to the average charge distribution of an electron in ϕ_i. Since the result of the Coulomb operator, $\hat{J}_i\phi_j(\mathbf{x}_1)$, on an orbital, ϕ_j, only depends on the value of the orbital at $\mathbf{x}_1$, the operator is called local.

The exchange operator

In contrast to the Coulomb operator, the exchange operator, $\hat{K}_i$, has no classical counterpart and is only defined through its operation on an orbital $\phi_j(\mathbf{x}_1)$

$$\begin{aligned}\hat{K}_i\phi_j(\mathbf{x}_1) &= \int \phi_i^*(\mathbf{x}_2)\hat{h}_2\phi_i(\mathbf{x}_1)\phi_j(\mathbf{x}_2)d\mathbf{x}_2 \\ &= \int \frac{\phi_i^*(\mathbf{x}_2)\phi_j(\mathbf{x}_2)}{|\mathbf{r}_1 - \mathbf{r}_2|}d\mathbf{x}_2\ \phi_i(\mathbf{x}_1) \quad (4.18)\end{aligned}$$

So the operation of $\hat{K}_i$ leads to an interchange of the coordinates of the two orbitals and, consequently, the result of the exchange operator on an orbital, ϕ_j, depends on the value of ϕ_j at every point in space. Therefore $\hat{K}_i$ is called a non-local operator. It is clear that both $\hat{J}_i$ and $\hat{K}_i$ depend on the orbitals ϕ_i so that the Fock operator (4.15) depends on all the orbitals $\phi_1, ..., \phi_N$. Therefore the solutions of the Hartree-Fock equations (4.14) have to be found self-consistently: starting from an initial guess for the orbitals, new orbitals are computed from the HF equations which can then be used as a better guess for the orbitals. This procedure can be repeated until convergence has been reached, i.e. until the input and output orbitals are (nearly) the same. A problem with the procedure of finding the electron orbitals is that they still have to be represented at every point in space, which is, in practice, impossible. The use of a finite basis set to represent the different orbitals, as described in the previous section, can resolve this problem and leads to the so-called Hartree-Fock-Roothaan method [21].

Discussion

The N lowest energy solutions of the Fock-operator can be combined into a Slater-determinant which is the approximate ground state wavefunction for the hamiltonian (4.10). But it is also possible to regard this wavefunction as the exact solution

for the independent-particle hamiltonian

$$\hat{H}_{HF} = \sum_{i}^{N} \hat{F}_{HF}(i). \tag{4.19}$$

However, the expectation value for this hamiltonian, $\langle\psi_{HF}|\hat{H}_{HF}|\psi_{HF}\rangle$, is not the energy of the system described by (4.10). But from (4.15) and (4.13), it follows that they are related,

$$E = \langle\hat{H}\rangle = \langle\hat{H}_{HF}\rangle - \frac{1}{2}\sum_{i}\langle\hat{J}_i - \hat{K}_i\rangle. \tag{4.20}$$

4.3 LCAO and qualitative molecular orbital theory

Molecular orbital (MO) theory is a very widely used theory in quantum chemistry which is able to give both quantitative as qualitative results for molecular systems. Since there are better suited approaches to get quantitative results for the problems in this thesis, such as density functional theory, the focus will be on the qualitative results that can be obtained with molecular orbital theory. These will be very important for the interpretation of many of the performed calculations. Because this theory is not so well known in the physics community, several examples will be given to demonstrate this interpretative power.
Molecular orbital theory is comparable to the Hartree-Fock theory. Just like the Hartree-Fock approximation, it assumes the different electrons in the system to occupy different orbitals, represented by orthonormal wavefunctions which can be combined into a Slater determinant to get the full many-body wavefunction. But in contrast to HF theory, the hamiltonian (4.10) is replaced with an (unknown) effective hamiltonian, $\hat{H}_{\text{eff}}$, which has as exact eigenfunctions Slater determinants, $\Psi(\mathbf{x}_1, ..., \mathbf{x}_N) = |\phi_1, ..., \phi_n|$,

$$\hat{H}_{\text{eff}} = \sum_{I}^{N} \hat{h}_{\text{eff}}(i) \tag{4.21}$$

$$\Rightarrow \quad \hat{H}_{\text{eff}}\Psi = \sum_{I}^{N} \hat{h}_{\text{eff}}(i)\Psi = (\sum_{i}^{N} \epsilon_i)\Psi = E\Psi \tag{4.22}$$

with $\hat{h}_{\text{eff}}\phi_i = \epsilon_i\phi_i$. Similar to the Hartree-Fock-Roothaan approach, it is possible to express the orbitals as linear combinations of a predefined basis set. In the qualitative application of MO theory the (normalized) atomic orbitals, $\{\chi_1, ...\chi_{N_b}\}$, of the different atoms of the system, which are supposed to be known, are taken as

the basis. So ϕ_p can (approximately) be written as a linear combination of atomic orbitals (LCAO), $\phi_p = \sum_j^{N_b} c_{jp}\chi_j$ and it follows that

$$\langle\chi_i|\hat{h}_{\text{eff}}|\phi_p\rangle \simeq \sum_j^{N_b} c_{jp}\langle\chi_i|\hat{h}_{\text{eff}}|\chi_j\rangle = \epsilon_p \sum_j^{N_b} c_{jp}\langle\chi_i|\chi_j\rangle. \tag{4.23}$$

This can be written as a generalized matrix eigenvalue problem

$$\begin{aligned} &\textstyle\sum_j^{N_b} c_{jp}(H_{ij} - \epsilon_p S_{ij}) = 0, \qquad j = 1, ..., N_b \\ &\Rightarrow (\underline{\underline{\mathrm{H}}} - \epsilon\underline{\underline{\mathrm{S}}})\underline{\mathrm{c}} = 0. \end{aligned} \tag{4.24}$$

with the effective hamiltonian matrix and the overlap matrix respectively defined by $H_{ij} = \langle\chi_i|\hat{h}_{\text{eff}}|\chi_j\rangle$ and $S_{ij} = \langle\chi_i|\chi_j\rangle$. The last equation only has a non-trivial solution if the determinant of the matrix $(\underline{\underline{\mathrm{H}}} - \epsilon\underline{\underline{\mathrm{S}}})$ is zero, $|\underline{\underline{\mathrm{H}}} - \epsilon\underline{\underline{\mathrm{S}}}| = 0$. This is called the secular equation and it is easily solved once H_{ij} and S_{ij} are known. But, although the matrix elements S_{ij} are known, because the atomic orbitals are supposed to be given, H_{ij} is unspecified since $\hat{h}_{\text{eff}}$ is not known. In practice, several strategies are used to get realistic estimates for these unknowns, e.g. by fitting to experimental data, but these are not very important when only qualitative results are desired. Some simple examples will be given to demonstrate how it is possible to get qualitative estimates of the unknown matrix elements.

4.3.1 Homonuclear diatomic molecules

As a first example, the simplest molecule of all is studied, namely the hydrogen molecule-ion, H_2^+. The basis set for this molecule consists of only two atomic orbitals, the spherical symmetric 1s-orbitals, s_a and s_b, of the two hydrogen atoms. Writing the molecular orbitals as a linear combination of these atomic orbitals, $\sigma_i = c_{1i}s_\mathrm{a} + c_{2i}s_\mathrm{b}$, the secular equation becomes

$$\begin{vmatrix} H_{\mathrm{aa}} - \epsilon S_{\mathrm{aa}} & H_{\mathrm{ab}} - \epsilon S_{\mathrm{ab}} \\ H_{\mathrm{ba}} - \epsilon S_{\mathrm{ba}} & H_{\mathrm{bb}} - \epsilon S_{\mathrm{bb}} \end{vmatrix} = 0. \tag{4.25}$$

$S_{\mathrm{aa}} = S_{\mathrm{bb}} = 1$, because of the normalization of the atomic orbitals, and if we define $S_{\mathrm{ab}} = S_{\mathrm{ba}} \equiv S$, $H_{\mathrm{aa}} = H_{\mathrm{bb}} \equiv \alpha$, and $H_{\mathrm{ab}} = H_{\mathrm{ba}} \equiv \beta$, the determinant can be written as

$$\begin{vmatrix} \alpha - \epsilon & \beta - \epsilon S \\ \beta - \epsilon S & \alpha - \epsilon \end{vmatrix} = 0. \tag{4.26}$$

which results in

$$\epsilon_1 = \frac{\alpha + \beta}{1 + S}, \qquad \epsilon_2 = \frac{\alpha - \beta}{1 - S} \tag{4.27}$$

and the corresponding normalized molecular orbitals are

$$\sigma_1 = \frac{1}{\sqrt{2(1+S)}}(s_\mathrm{a} + s_\mathrm{b}), \qquad \sigma_2 = \frac{1}{\sqrt{2(1-S)}}(s_\mathrm{a} - s_\mathrm{b}) \tag{4.28}$$

So the problem is completely solved once we know α and β. The hydrogen molecule-ion is a single electron system and therefore the exact effective hamiltonian (4.21) is known

$$\hat{H}_\mathrm{eff} = \hat{h}_\mathrm{eff}(1) = -\frac{1}{2}\nabla^2 - \frac{1}{r_a} - \frac{1}{r_b} + \frac{1}{R} \tag{4.29}$$

where r_a and r_b are the distances of the electron from the two nuclei which are separated by a distance R. Note that the repulsion term between the two nuclei (3.5) has been explicitely incorporated here. It is now possible to find an explicit expression for the so-called Coulomb integrals, α,

$$\alpha = \langle s_a|\hat{h}_\mathrm{eff}(1)|s_a\rangle = \langle s_a| - \frac{1}{2}\nabla^2 - \frac{1}{r_a}|s_a\rangle + \langle s_a| - \frac{1}{r_b} + \frac{1}{R}|s_a\rangle \tag{4.30}$$

$$= E_\mathrm{1s} + \left(-\int \frac{|s_a|^2}{r_b} d\mathbf{x}_1 + \frac{1}{R}\right). \tag{4.31}$$

The first term follows from the fact that s_a is an exact eigenfunction of the hydrogen hamiltonian with energy E_{1s}. The term between brackets will be close to zero when the distance between the nuclei is large enough. Therefore it will be neglected so that the self-interaction can be approximated by

$$\alpha \approx E_\mathrm{1s}. \tag{4.32}$$

The so-called resonance intergrals (or exchange integrals), β, can be treated in a similar way.

$$\beta = \langle s_a|\hat{h}_\mathrm{eff}(1)|s_b\rangle = \langle s_a| - \frac{1}{2}\nabla^2 - \frac{1}{r_a}|s_b\rangle + \langle s_a| - \frac{1}{r_b} + \frac{1}{R}|s_b\rangle \tag{4.33}$$

$$= E_\mathrm{1s}S + \left(-\int s_a \frac{1}{r_b} s_b d\mathbf{x}_1 + \frac{S}{R}\right). \tag{4.34}$$

However, now the term between brackets can not be neglected. The maximum of the overlap between s_a and s_b is situated right between the two nuclei and therefore its interaction with one nucleus (the first term between the brackets) is roughly twice as large as the interaction between the two nuclei weighted with the overlap (the second term between the brackets). So the resonance integral, β, can be approximated as

$$\beta \approx E_{1s}S - \frac{S}{R} \qquad \Rightarrow \qquad \beta \sim S \tag{4.35}$$

Inserting these approximations into the formulas (4.27) for the solution of the secular equation gives

$$\epsilon_1 = E_{1s} - \frac{S}{R(1+S)}, \qquad \epsilon_2 = E_{1s} + \frac{S}{R(1-S)} \tag{4.36}$$

Because the overlap S is a positive quantity $\epsilon_1 < E_{1s}$ and $\epsilon_2 > E_{1s}$. Therefore the corresponding molecular orbitals, σ_1 and σ_2, are referred to as the bonding and anti-bonding orbitals, respectively. The denominator of the energy shifts in (4.36) makes sure that the anti-bonding orbital is always more anti-bonding than the bonding orbital is bonding. A schematic summary of the results so far is given in Fig. 4.1a.

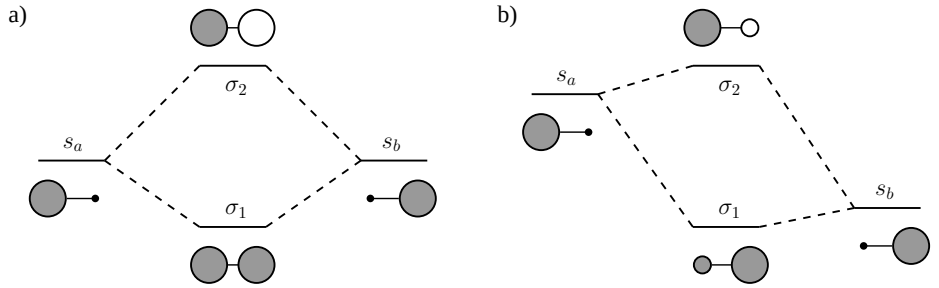

Figure 4.1. *The energy levels of the MO's of a) a homonuclear and b) a heteronuclear molecule.*

From this approximation one could get the impression that decreasing the distance between the nuclei, and consequently increasing the overlap, will infinitely lower the energy of the bonding orbital. However, the approximations were only valid for large distances and a short look at (4.31) makes it clear that at short distances the energy will increase enormously by the nuclear repulsion. This is also shown in Fig. 4.2 where the approximate solutions are plotted together with the full LCAO solutions.

4.3.2 Heteronuclear diatomic molecules

In the example of the hydrogen molecule the two interacting atomic orbitals had the same energy. Let us now examine what happens if the two interacting atomic orbitals, s_a and s_b have different energy. In that case the secular equation can be written as

$$\begin{vmatrix} \alpha_a - \epsilon & \beta - \epsilon S \\ \beta - \epsilon S & \alpha_b - \epsilon \end{vmatrix} = 0. \tag{4.37}$$

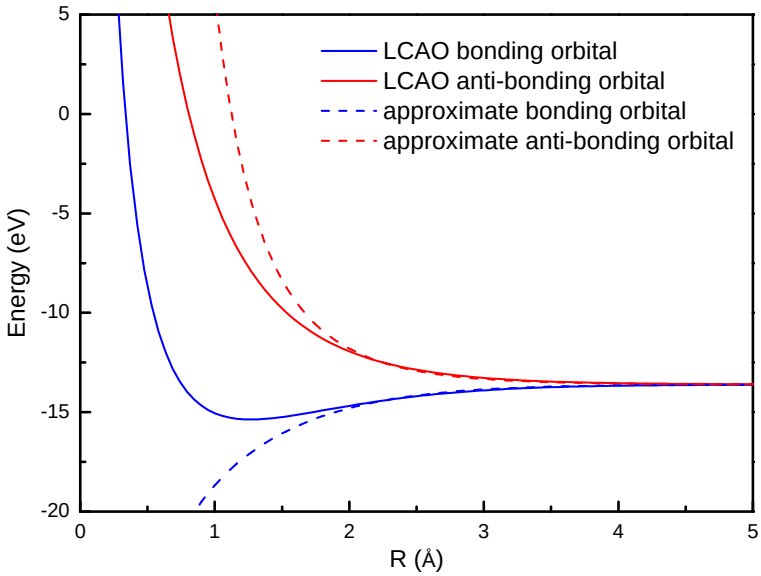

Figure 4.2. *Variation of the energy levels with the internuclear distance in a hydrogen molecule-ion.*

Assuming that the difference in energy, $(\alpha_b - \alpha_a) > 0$, is large, the solutions are

$$\epsilon_1 \approx \alpha_a - \frac{\beta^2}{\alpha_b - \alpha_a}, \qquad \epsilon_2 \approx \alpha_b + \frac{\beta^2}{\alpha_b - \alpha_a} \tag{4.38}$$

and the corresponding (unnormalized) molecular orbitals are

$$\sigma_1 \approx s_a - \left(\frac{\beta}{\alpha_b - \alpha_a}\right) s_b, \qquad \sigma_2 \approx \left(\frac{\beta}{\alpha_b - \alpha_a}\right) s_a + s_b. \tag{4.39}$$

So the bonding orbital, σ_1, has an energy that is a little bit lower than the lowest energy of the atomic orbitals and is located largely at the position of the atom with the lowest atomic orbital energy. On the other hand, the anti-bonding orbital has an energy that is higher than the highest energy of the atomic orbitals and is located largely at the position of this atom with the highest energy. This is schematically represented in Fig. 4.1b.

Discussion

From the two simple examples, given above, a lot of qualitative information and rules can be deduced which can be applied to much more complicated systems. The picture that was given is not only applicable to the interaction between two atomic 1s-orbitals, but can be applied to any number of orbitals with arbitrary symmetry. Bringing together two arbitrary orbitals results in the formation of two

new orbitals, a bonding and an anti-bonding one, of which the first is (usually) shifted down in energy and the second is shifted up by a larger amount. The rules for the shifting of the energies can be summarized as follows:

$$\Delta E \approx \begin{cases} \beta & \text{if} \quad \alpha_a = \alpha_b \\ \frac{\beta^2}{\alpha_b - \alpha_a} & \text{if} \quad \alpha_a \ll \alpha_b \end{cases} \tag{4.40}$$

with α_a and α_b the energies of the interacting orbitals. In other words there will only be interaction between orbitals that have similar energies and nonzero overlap. This last requirement follows from the fact that the resonance integral, β, is proportional with the overlap S (see (4.35)). So when e.g. two atoms approach each other only those atomic orbitals interact with each other that have nonzero overlap and are close in energy. Usually only the orbitals of valence electrons will have an appreciable overlap and core electrons can be neglected.

Many-electron systems

Until now, only single electron systems have been treated. In the qualitative molecular orbital theory a description of many-electron molecules is obtained by simply adding extra electrons in the molecular orbitals of the system. In other words, the (inter-atomic) electron-electron interaction is neglected. When filling up the molecular orbitals with electrons, some interesting conclusions can be made with respect to bonding and charge transfers between the atoms. To illustrate the bonding and charge transfer mechanisms between atoms, consider the fictitious system of interacting atoms, A and B, of which the orbital energies are given in Fig. 4.3. Four possible orbital-orbital interactions are explicitly shown.

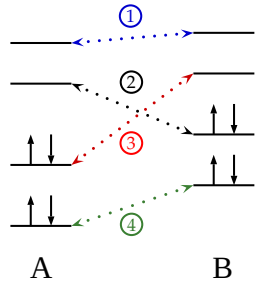

Figure 4.3. *The interaction between the orbitals of two fictitious atoms A and B. Four interactions are explicitly shown.*

The first one (1) is between empty orbitals and it is clear that this interaction will (in general[3]) have no influence on the bonding and does not induce charge transfer.

[3]For exceptions, see later.

The interaction between filled and empty orbitals, (2) and (3), stabilizes the bond between A and B since the filled orbitals are pushed down due to the interaction. The empty orbitals are shifted to higher energies but, because they are empty, this has no influence on the energy. Both the interactions will lead to charge transfer: interaction (2) induces a charge transfer from B to A and interaction (3) from A to B. The total charge transfer depends on the relative strength of the two interactions which in turn depends on the overlap and the energy difference of the orbitals.
The interaction between filled orbitals, interaction (4), is always repulsive because the resulting bonding orbital is less stabilized than the anti-bonding MO is destabilized. There is no charge transfer involved here since both orbitals were already filled.

For now, only interacting atoms have been considered, but all the results are readily generalized to interacting molecules. The only difference is that instead of interacting atomic orbitals, one has interacting molecular orbitals now. However, the interaction between molecules is usually weaker.
In this thesis, the interaction of atoms and molecules with a graphene surface is investigated. Graphene, however, is a solid and it is not immediately clear how the ideas discussed above can be applied to this case. It is necessary therefore to generalize these ideas to the solid state case. This can be done with the well-known tight-binding approximation.

4.4 Tight-binding approach

The tight-binding approach is a well-known model in condensed matter physics. It is closely related to the LCAO approximation from the previous section and might be considered as the application of this approximation to periodic structures (crystals). For periodic structures one can apply the Bloch theorem (see Appendix A). In short, the basis of n_b atomic orbitals in the LCAO method can be replaced by a basis set of n_b basis functions per wavevector, $\mathbf{k}$, constructed by placing the atomic orbitals at all the lattice sites, $\mathbf{R}$,

$$\phi_i(\mathbf{r}) \quad \rightarrow \quad \Phi_{i,\mathbf{k}}(\mathbf{r}) = \sum_{\mathbf{R}} c_{\mathbf{k},\mathbf{R}} \phi_i(\mathbf{r}+\mathbf{R}). \tag{4.41}$$

For these basis functions to obey the Bloch theorem,

$$\Phi_{i,\mathbf{k}}(\mathbf{r}+\mathbf{R}') = e^{i\mathbf{k}\cdot\mathbf{R}'}\Phi_{i,\mathbf{k}}(\mathbf{r}), \tag{4.42}$$

it is required[4] that $c_{\mathbf{k},\mathbf{R}} = e^{-i\mathbf{k}\cdot\mathbf{R}}$, so that

$$\Phi_{i,\mathbf{k}}(\mathbf{r}) = \sum_{\mathbf{R}} e^{-i\mathbf{k}\cdot\mathbf{R}}\phi_i(\mathbf{r}+\mathbf{R}). \tag{4.43}$$

[4]This follows immediately from inserting (4.41) in (4.42)

With these basis functions it is possible to set up a secular equation for every wavevector, $\mathbf{k}$,

$$|H_{ij,\mathbf{k}} - ES_{ij,\mathbf{k}}| = 0, \tag{4.44}$$

with $H_{ij,\mathbf{k}} = \langle\Phi_{i,\mathbf{k}}|\hat{H}|\Phi_{j,\mathbf{k}}\rangle$ and $S_{ij,\mathbf{k}} = \langle\Phi_{i,\mathbf{k}}|\Phi_{j,\mathbf{k}}\rangle$. The overlap matrix $S_{ij,\mathbf{k}}$ is usually taken to be the identity matrix, δ_{ij}. The hamiltonian matrix, $H_{ij,\mathbf{k}}$, can be written as

$$\begin{aligned} H_{ij,\mathbf{k}} = \langle\Phi_{i,\mathbf{k}}|\hat{H}|\Phi_{j,\mathbf{k}}\rangle &= \sum_{\mathbf{R}}\sum_{\mathbf{R}'} e^{i\mathbf{k}(\mathbf{R}-\mathbf{R}')}\langle\phi_i(\mathbf{r}+\mathbf{R})|\hat{H}|\phi_j(\mathbf{r}+\mathbf{R}')\rangle \quad (4.45)\\ &= N\sum_{\mathbf{R}'} e^{-i\mathbf{k}\mathbf{R}'}\langle\phi_i(\mathbf{r})|\hat{H}|\phi_j(\mathbf{r}+\mathbf{R}')\rangle. \quad (4.46) \end{aligned}$$

where N denotes the number of unit cells. Dividing (4.46) by N makes sure that the energy in (4.44) is given per unit cell. From (4.46) it can be seen that the interaction of an orbital, ϕ_i, with all the orbitals, ϕ_j at every lattice site, R', is taken into account. But we know from MO theory that the interaction at large distance is negligible (since it is proportional to the overlap between the interacting orbitals), so it is sufficient to calculate

$$H_{ij,\mathbf{k}} = \sum_{\mathbf{R}\leq\mathbf{R}_0} e^{-i\mathbf{k}\mathbf{R}}\langle\phi_i(\mathbf{r})|\hat{H}|\phi_j(\mathbf{r}+\mathbf{R})\rangle. \tag{4.47}$$

with $\mathbf{R}_0$ some appropriate distance (usually the first or second nearest neighbor distance). For the remaining terms one can apply similar approximations as for the LCAO approximation.
As an example of the tight-binding approach, I will use it to give a qualitative description for the valence and conduction band of graphene.

Graphene: tight-binding approximation

The crystal structure of graphene is shown in Fig. 4.4 together with the first Brillouin zone. The high symmetry points that determine the lines along which the electronic band structure is usually calculated (as shown in e.g. Fig. 2.1) are also indicated.
Graphene is very well suited for a description with a tight-binding model. The reason for this is that its two dimensional nature allows the separate treatment of atomic orbitals that are symmetric and anti-symmetric with respect to the graphene plane. The overlap between these two types of orbitals is necessarily zero so they will not interact. In Fig. 4.5 the different atomic orbitals of the carbon atoms in a graphene crystal are shown.
The three different sp^2-orbitals are lower in energy than the p_z orbital and will have much more overlap with the orbitals of the same symmetry on neighboring

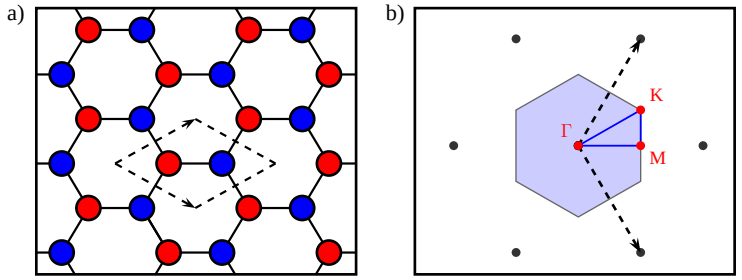

Figure 4.4. *a) The crystal structure of graphene: there are two carbon atoms per unitcell which build up two sublattices shown in different colors. b) The corresponding reciprocal space and the first BZ: the high symmetry point, Γ, K, and M are indicated.*

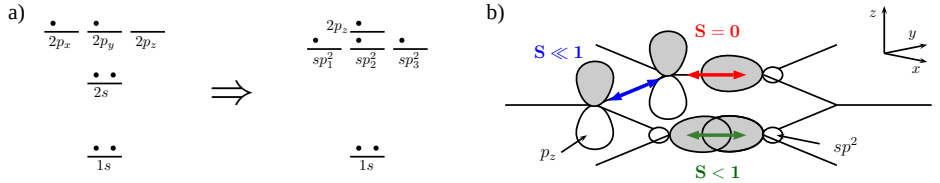

Figure 4.5. *a) Energy levels of carbon atomic orbitals and hybridized orbitals. b) The interaction between the (valence) orbitals of carbon atoms in a graphene crystal.*

atoms. Therefore the resulting bonding and anti-bonding molecular orbitals will lie far below and above the Fermi-level, respectively. The interaction between the p_z-orbitals of neighboring atoms will be smaller, which results in bonding and anti-bonding orbitals close to the Fermi-level. Since we are interested in the behavior of electrons around the Fermi-level, only the p_z-orbitals will be considered. So there are two atomic orbitals per unitcell, one p_z-orbital on each carbon atom, that are taken into account. From these two orbitals, p_A and p_B, Bloch waves of the form (4.43) are constructed that are spread out over the A- and B-sublattice, respectively. These Bloch-waves, $P_{A,\mathbf{k}}$ and $P_{B,\mathbf{k}}$, are used to set up the secular equation for every wavevector, $\mathbf{k}$,

$$\begin{vmatrix} H_{\mathrm{AA},\mathbf{k}} - E & H_{\mathrm{AB},\mathbf{k}} \\ H_{\mathrm{BA},\mathbf{k}} & H_{\mathrm{BB},\mathbf{k}} - E \end{vmatrix} = 0, \tag{4.48}$$

where the overlap matrix, $S_{\mathrm{ij},\mathbf{k}}$, has been approximated by the identity matrix. If we take only into account nearest-neighbor interaction then every p_z-orbital interacts only with itself and with 3 p_z-orbitals on the other sublattice (see Fig. 4.5b). Using (4.47), the secular equation becomes

$$\begin{vmatrix} \alpha - E & \beta f(\mathbf{k}) \\ \beta f(\mathbf{k})^* & \alpha - E \end{vmatrix} = 0,$$

with $\alpha = \langle p_A|\hat{H}|p_A\rangle$, $\beta = \langle p_A|\hat{H}|p_B\rangle$. The form factor, $f(\mathbf{k})$, is defined by

$$f(\mathbf{k}) = e^{i\mathbf{k}(\frac{1}{3}\mathbf{a}_1+\frac{1}{3}\mathbf{a}_2)} + e^{i\mathbf{k}(\frac{1}{3}\mathbf{a}_1-\frac{2}{3}\mathbf{a}_2)} + e^{i\mathbf{k}(-\frac{2}{3}\mathbf{a}_1+\frac{1}{3}\mathbf{a}_2)}. \tag{4.49}$$

if only first-neighbor interaction is taken into account. α is usually taken to be zero because it merely shifts the energy scale, while the value of β is determined from fits to experiment or density functional theory calculations. A fit to a DFT-LDA calculation (see next section) gives $\beta \approx 2.8$ eV. With this value for β we can solve the secular equation and find $E_i(\mathbf{k})$. It is easy to solve this equation at high symmetry points such as the Γ-point, (0,0), or the K-point, $(\frac{1}{3}, \frac{2}{3})$ in reduced coordinates. The graphene bonding and anti-bonding orbitals at the Γ-point are shown in Fig. 4.6. It can be readily seen that the (relative) energies corresponding to these orbitals are 3β and -3β, respectively, since every atomic orbital forms 3 bonding or anti-bonding combinations with its nearest neighbors and there are two atoms per unitcell.

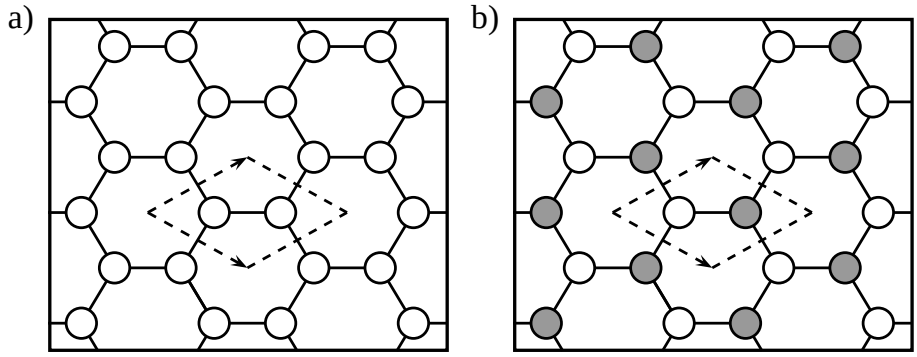

Figure 4.6. *The bonding (a) and anti-bonding (b) graphene orbitals at the* Γ*-point.*

At the K-point the situation is completely different. As shown in Fig. 4.7 the bonding and anti-bonding combinations are equivalent and correspond to orbitals which are restricted to one of the two sublattices. In the nearest-neighbor approximation this means that these orbitals are non-bonding so that their relative energy is zero. It can also be seen that the approximation of the overlap matrix $S_{ij,\mathbf{k}}$ by the identity matrix is exact at the K-point. Since the Fermi-surface of intrinsic graphene corresponds to these K-points, this means that our simple tight-binding model is actually a very good model for the low energy excitations in graphene.

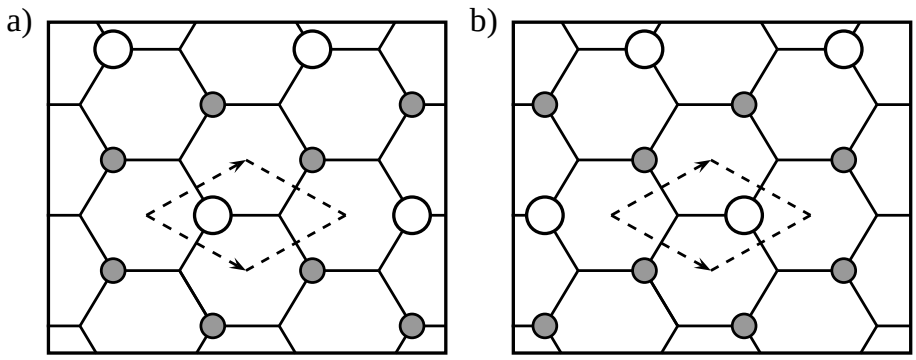

Figure 4.7. *The (real part) of the two equivalent graphene orbitals at the K-point.*

Chapter 5

Density Functional Theory

The most advanced theoretical formalism that I will use is density functional theory (DFT). A short description of this theory is given in the following.
DFT is entirely based on two theorems stated by Hohenberg and Kohn [22] in 1964. But, although these theorems are very important, DFT would not be so popular today without the ingenious approach of Kohn and Sham to put this theory into practice [23]. In the following sections the Hohenberg-Kohn theorems and the Kohn-Sham approach will be treated together with some practical considerations that are important for the results obtained in this thesis.

5.1 The Hohenberg-Kohn theorems

As stated before, DFT is based on the two Hohenberg-Kohn (HK) theorems: the first theorem states that the wavefunction, which has a central position in standard quantum theory, can be replaced by the electron ground state density without any loss of information and the second theorem is more or less the equivalent of the variation principle in standard quantum mechanics. The proofs of these theorems are rather easy and are included here for completeness. The main focus, however, will be on the physical picture.
Before stating the HK theorems in a more rigorous way let us recall our hamiltonian:

$$\hat{H} = \hat{T} + \hat{V}_{ee} + \hat{V}_{ext}, \tag{5.1}$$

with the different terms on the right defined in (3.6). As noted before, the first two of these terms are universal while the third uniquely determines the hamiltonian.

5.1.1 The first Hohenberg-Kohn theorem

The first Hohenberg-Kohn theorem can be stated as follows:

> The external potential, $V_{ext}(\mathbf{r})$, of any system of interacting particles is uniquely determined (up to a constant) by the particle density, $\rho_0(\mathbf{r})$, of the ground state.

So the hamiltonian (5.1), which is completely specified by this external potential, is also uniquely determined by the ground state electron density. Before proving this theorem it is useful to have a more intuitively feeling for it: starting from the ground state electron density, it is possible to deduce important information about the potential producing this same density. First, the density has maxima at the positions of the nuclei $\{\mathbf{R}_I\}$ and the charge of the nuclei $\{Z_I\}$ is closely related to the density at these same positions [24]. Second, the integral of the density over all space provides the total number of electrons, therefore all the parameters needed for the unique specification of the hamiltonian, $\{N,\{\mathbf{R}_I\},\{Z_I\}\}$, are known. This makes the theorem at least plausible.

The rigorous proof of the first theorem is based on reductio ad absurdum and actually requires that the ground state is non-degenerate. Suppose that two external potentials which differ by more than a constant, $V^1_{ext}(\mathbf{r})$ and $V^2_{ext}(\mathbf{r})$, lead to the same ground state density $\rho_0(\mathbf{r})$, i.e.

$$\hat{H}_1\psi_1 = (\hat{T} + \hat{V}_{ee} + \hat{V}^1_{ext})\psi_1 = E_1\psi_1 \quad \Rightarrow \quad \psi_1 \rightarrow \rho_0(\mathbf{r}) \tag{5.2}$$

$$\hat{H}_2\psi_2 = (\hat{T} + \hat{V}_{ee} + \hat{V}^2_{ext})\psi_2 = E_2\psi_2 \quad \Rightarrow \quad \psi_2 \rightarrow \rho_0(\mathbf{r}) \tag{5.3}$$

First we prove that ψ_1 and ψ_2 can not be the same. Suppose $\psi_1 = \psi_2 = \psi$, then it follows from subtracting (5.3) from (5.2) that

$$(\hat{V}^1_{ext} - \hat{V}^2_{ext})\psi = (E_1 - E_2)\psi, \tag{5.4}$$

so V^1_{ext} and V^2_{ext} differ by a constant, namely $E_1 - E_2$. This contradicts our assumption and implies that ψ_1 and ψ_2 cannot be the same. ψ_2 can now be used as a trial wavefunction for $\hat{H}_1$. Taking into account the variation principle and our assumption of a non-degenerate ground state, it follows that

$$\begin{aligned} E_1 < \langle\psi_2|\hat{H}_1|\psi_2\rangle &= \langle\psi_2|\hat{H}_2|\psi_2\rangle + \langle\psi_2|\hat{H}_1 - \hat{H}_2|\psi_2\rangle \\ &= E_2 + \langle\psi_2|\hat{V}^1_{ext} - \hat{V}^2_{ext}|\psi_2\rangle, \end{aligned}$$

and after inserting the definition of $\hat{V}_{ext}$ (given in (3.6))

$$E_1 < E_2 + \int \rho_0(\mathbf{r})(V^1_{ext} - V^2_{ext})d\mathbf{r}. \tag{5.5}$$

After interchanging the indices 1 and 2 and repeating the above steps we arrive at

$$E_2 < E_1 + \int \rho_0(\mathbf{r})(V^2_{ext} - V^1_{ext})d\mathbf{r}. \tag{5.6}$$

Addition of the equations (5.5) and (5.6) leads to a clear contradiction

$$E_1 + E_2 < E_1 + E_2$$

In other words, there cannot be two external potentials leading to the same ground state density. It follows then that the external potential is uniquely determined by the ground state density. This completes the proof of our first theorem.

The fact that the ground state particle density specifies the hamiltonian (5.1) of the system, allows us to consider all properties of the system as functionals[1] of the ground state density. In particular the ground state energy of the system with hamiltonian (5.1) can be written as

$$\begin{aligned} E_{HK}[\rho_0] &= T[\rho_0] + V_{ee}[\rho_0] + V_{ext}[\rho_0] \\ &\equiv F_{HK}[\rho_0] + \int \rho_0(\mathbf{r}) V_{ext}(\mathbf{r}) d\mathbf{r}, \end{aligned} \tag{5.7}$$

where $F_{HK}[\rho_0] = T[\rho_0] + V_{ee}[\rho_0]$ is a universal functional of the density. But this is only a formal reformulation, a matter of principle, which does not tell us what these functionals look like. In fact, how can we even be sure that the density ρ_0 corresponding to the lowest energy given by the $E_{HK}[\rho]$, is the ground state density we are looking for? The answer to this last question is the subject of the second Hohenberg-Kohn theorem.

5.1.2 The second Hohenberg-Kohn theorem

The second Hohenberg-Kohn theorem can be stated as follows:

> The ground state energy of a system with an external potential $V_{ext}(\mathbf{r})$ is given by the minimum value of the energy functional $E_{HK}[\rho]$ and the density for which this minimum is reached corresponds with the ground state density $\rho_0(\mathbf{r})$.

Note that the functional $E_{HK}[\rho]$ in (5.7) depends on the particular potential $V_{ext}(\mathbf{r})$ but that this dependence is universal. This theorem is nothing more than the energy variation principle applied to the density instead of the wavefunction. The proof is therefore analogous.

Suppose we have two different densities $\rho_1(\mathbf{r})$ and $\rho_2(\mathbf{r})$. According to the first HK theorem, these densities correspond with two different external potentials $V^1_{ext}(\mathbf{r})$ and $V^2_{ext}(\mathbf{r})$ and, obviously, with two different ground state wavefunctions ψ_1 and

[1] A functional is roughly a function of a function, i.e. it transforms functions into numbers

ψ_2.

$$E^1_{HK}[\rho_1] = E_1 = \langle\psi_1|\hat{H}_1|\psi_1\rangle$$
$$E^2_{HK}[\rho_2] = E_2 = \langle\psi_2|\hat{H}_2|\psi_2\rangle \tag{5.8}$$

Using ψ_2 as a trial wavefunction for $\hat{H}_1$, we get

$$\langle\psi_2|\hat{H}_1|\psi_2\rangle = E_2' > E_1 = \langle\psi_1|\hat{H}_1|\psi_1\rangle. \tag{5.9}$$

Since we did not make any assumptions[2] about $\rho_2(\mathbf{r})$, it is clear that the energy given by the Hohenberg-Kohn functional (5.7) for the correct ground state (i.e. E_1) is indeed lower than the energy from this expression for any other density (i.e. E_2').

5.1.3 The constrained search formulation

Several assumptions which were made in the proofs of the original Hohenberg-Kohn theorems are actually not necessary. The necessity of a non-degenerate ground state and the V-representability of the density in the proofs of the first and the second theorem respectively, can be removed within the constrained search formulation of Levy and Lieb. Although these are important technical improvements, this is not the reason for including the constrained search formulation here. The main reason is that this approach provides us with an in-principle way to determine the exact energy functional.
The approach of Levy and Lieb starts with the formulation of the ground state energy, E, in terms of the variation principle

$$E = \min_{\psi}\langle\psi|\hat{H}|\psi\rangle = \min_{\psi}\langle\psi|\hat{T} + \hat{V}_{ee} + \hat{V}_{ext}|\psi\rangle. \tag{5.10}$$

where the variation is over all many-body wavefunctions $\psi(\mathbf{x}_1, ..., \mathbf{x}_N)$ with N particles. They continue by introducing an intermediate step in which they first look for the minimum in a subset of wavefunctions that produce a certain density $\rho(\mathbf{r})$ which is then varied until the minimum is reached

$$\begin{aligned} E = \min_{\rho} E_{LL}[\rho] &= \min_{\rho}\left(\min_{\psi\to\rho}\langle\psi|\hat{T} + \hat{V}_{ee} + \hat{V}_{ext}|\psi\rangle\right) \\ &= \min_{\rho}\left(\min_{\psi\to\rho}\langle\psi|\hat{T} + \hat{V}_{ee}|\psi\rangle + \int\rho(\mathbf{r})V_{ext}(\mathbf{r})d\mathbf{r}\right) \\ &\equiv \min_{\rho}\left(F[\rho] + \int\rho(\mathbf{r})V_{ext}(\mathbf{r})d\mathbf{r}\right) \end{aligned} \tag{5.11}$$

where $F[\rho] = \min_{\psi\to\rho}\langle\psi|\hat{T}+\hat{V}_{ee}|\psi\rangle$ is a universal functional of $\rho(\mathbf{r})$. This functional can be compared with the Hohenberg-Kohn functional defined in (5.7). Although

[2] except for the fact that the potential should be V-representable

they should both give the same results for the ground state density, the Levy-Lieb functional has the advantage of having a clear meaning: it is the minimum of the sum of the kinetic and internal interaction energy for all possible many-body wavefunctions producing the given density $\rho(\mathbf{r})$.
At first sight, it may seem that we arrived again at the starting point since the only progress we have made in finding the functional is to define it in terms of many-body wavefunctions. It will only be possible to appreciate these results well in light of the Kohn-Sham approach which is the subject of the following section.

5.2 The Kohn-Sham approach

In a sense the Kohn-Sham approach can be regarded as an attempt to include the benefits of the Hartree-Fock formalism in density functional theory while at the same time preserving all the electron correlations. The main problem when trying to find an approximate expression for the energy functional directly from the ground state density is the term coming from the kinetic energy. We only now how to express the kinetic energy as a functional of the wavefunction, i.e. $T[\Psi] = \langle\Psi|1/2\sum_i \nabla_i^2|\Psi\rangle$. The problem is that the same density can be reproduced by a variety of wavefunctions and these can actually have any kinetic energy. This can be demonstrated by regular plane waves, e^{ikx}, which all correspond to the same density but their kinetic energy is proportional with k^2. The actual ground state wavefunction is uniquely specified as the one corresponding to the lowest (total) energy but it should be clear now that it is not easy to get this directly from the density. Therefore Kohn and Sham proposed to make use of an auxiliary system for which it is possible to find the wavefunctions. It was shown in the Hartree-Fock approach that it is possible to construct a non-interacting hamiltonian which has Slater-determinants as exact solutions for the many-body wavefunction. The idea of Kohn and Sham was to construct a similar non-interacting reference system, i.e. a system of which the wavefunction can be found, so that its density equals the density of the real system. In other words, they assumed a reference system described by a hamiltonian with an effective local potential $V_s(\mathbf{r})$,

$$\hat{H}_S = -\frac{1}{2}\sum_i^N \nabla_i^2 + \sum_i^N V_s(\mathbf{r}_i), \tag{5.12}$$

of which the solution is a Slater-determinant $\Psi_S = |\phi_1\phi_2...\phi_N|$ so that

$$\rho_S(\mathbf{r}) = \sum_i^N |\phi_i|^2 = \rho_0(\mathbf{r}). \tag{5.13}$$

In analogy with Hartree-Fock, the different solutions ϕ_i are given by the N lowest energy solutions of

$$\hat{F}_{KS}\phi \equiv \left(-\frac{1}{2}\nabla^2 + V_s(\mathbf{r})\right)\phi = \epsilon\phi. \tag{5.14}$$

These equations are called the Kohn-Sham (KS) equations. Note that in contrast with the Hartree-Fock operator, $\hat{F}_{HF}$ (4.15), which contains the non-local exchange operator, $\hat{K}_i$, $\hat{F}_{KS}$ is purely local since $V_s(\mathbf{r})$ is local by construction. The problem is now to determine this $V_s(\mathbf{r})$ so that (5.13) is fulfilled. To this end, it should be realized that the only object linking the auxiliary independent particle system with the real system is their identical ground state density, $\rho_0(\mathbf{r})$. Therefore, it is convenient to write the energy of the independent particle system as an explicit functional of this density,

$$E_S[\rho_0(\mathbf{r})] \equiv T_S[\rho_0(\mathbf{r})] + \int \rho_0(\mathbf{r})V_s(\mathbf{r}), \tag{5.15}$$

in which T_S has been introduced as the kinetic energy functional of the independent particles. The whole idea of introducing this reference system was the calculation of the kinetic energy in the hope that it captures a great part of the kinetic energy of the real interacting system. Therefore we include the functional T_S explicitely in the energy functional of the interacting system (5.7) as follows:

$$\begin{aligned} E[\rho(\mathbf{r})] &= T[\rho(\mathbf{r})] + V_{ee}[\rho(\mathbf{r})] + V_{ext}[\rho(\mathbf{r})] \\ &\equiv T_S[\rho(\mathbf{r})] + \frac{1}{2}\int \frac{\rho(\mathbf{r})\rho(\mathbf{r}')d\mathbf{r}'}{|\mathbf{r}-\mathbf{r}'|} + V_{ext}[\rho(\mathbf{r})] + E_{xc}[\rho(\mathbf{r})]. \end{aligned} \tag{5.16}$$

in which a new functional, the exchange-correlation functional $E_{xc}[\rho(\mathbf{r})]$, has been defined as

$$E_{xc}[\rho(\mathbf{r})] = (T[\rho(\mathbf{r})] - T_S[\rho(\mathbf{r})]) + \left(V_{ee}[\rho(\mathbf{r})] - \frac{1}{2}\int \frac{\rho(\mathbf{r})\rho(\mathbf{r}')d\mathbf{r}'}{|\mathbf{r}-\mathbf{r}'|}\right). \tag{5.17}$$

This functional contains those parts of the energy for which there is no (exactly) known functional expression.
From the second HK theorem, it follows that the energy functionals of both systems, $E[\rho(\mathbf{r})]$ and $E_S[\rho_0(\mathbf{r})]$, are both extrema with respect to variations of $\rho_0(\mathbf{r})$. After the introduction of a Lagrange multiplier, μ, to keep the amount of particles constant, we get on the one hand,

$$\begin{aligned} 0 &= \delta\left(E_S[\rho(\mathbf{r})] - \mu\left\{\int \rho(\mathbf{r})d\mathbf{r} - N\right\}\right) \\ &= \left(\frac{\delta T_S[\rho(\mathbf{r})]}{\delta\rho(\mathbf{r})} + V_S(\mathbf{r}) - \mu\right)\delta\rho(\mathbf{r}), \end{aligned} \tag{5.18}$$

and on the other hand,

$$\begin{aligned} 0 &= \delta\left(E[\rho(\mathbf{r})] - \mu\left\{\int \rho(\mathbf{r})d\mathbf{r} - N\right\}\right) \\ &= \left(\frac{\delta T_S[\rho(\mathbf{r})]}{\delta\rho(\mathbf{r})} + \int \frac{\rho(\mathbf{r}')}{|\mathbf{r}-\mathbf{r}'|}d\mathbf{r}' + V_{ext}(\mathbf{r}) + \frac{\delta E_{xc}[\rho(\mathbf{r})]}{\delta\rho(\mathbf{r})} - \mu\right)\delta\rho(\mathbf{r}). \end{aligned} \tag{5.19}$$

Equating (5.18) and (5.19), the local potential $V_S(\mathbf{r})$ is found to be

$$V_S(\mathbf{r}) = \int \frac{\rho(\mathbf{r}')}{|\mathbf{r}-\mathbf{r}'|}d\mathbf{r}' + V_{ext}(\mathbf{r}) + V_{xc}(\mathbf{r}), \tag{5.20}$$

with $V_{xc} = \frac{\delta E_{xc}}{\delta\rho}$. Note that the effective local potential, V_S, depends on the particle density so that the solutions of the Kohn-Sham equations, (5.14), have to be found self-consistently, just like the Hartree-Fock equations.
We have arrived now at a formally exact procedure to find the ground state energy and density of any many-body system. An additional benefit of introducing an independent particle reference system is the simultaneous introduction of useful tools for physical interpretation like the electronic band structure of the system and the density of states.

5.3 Practical implementation of the DFT formalism

Although the theoretical formalism described until now is formally exact, approximations are unavoidable if one wants to make any practical calculation.

5.3.1 The exchange correlation functional

The main problem with the Kohn-Sham procedure described above is the introduction of the unknown exchange-correlation functional (5.17). As long as there is no expression for this term, it is impossible to solve the KS equations. Therefore several approximations have been devised to get an explicit form for this functional. The most widely used approximations in solid state physics are the local density approximation (LDA) and the generalized gradient approximation (GGA). The idea behind the local density approximation is to assume that the E_{xc} can be written in the following form

$$E_{xc}^{\mathrm{LDA}}[\rho] = \int \rho(\mathbf{r})\epsilon_{xc}(\rho(\mathbf{r}))d\mathbf{r}. \tag{5.21}$$

where $\epsilon_{xc}(\rho(\mathbf{r}))$ is a *function* that gives the exchange-correlation energy per particle of an electron gas of a uniform density $\rho(\mathbf{r})$. The exchange part of this uniform

electron gas can be found exactly whereas very accurate data, based on quantum Monte-Carlo simulations, is available for the correlation part [25]. At first sight, it would seem that LDA is not very accurate since the density of any real system is far from homogeneous, but in practice it seems to work surprisingly well.
LDA can be regarded as the zeroth order approximation of the exchange-correlation functional. When gradient corrections are added to this approximation,

$$E_{xc}^{\mathrm{GGA}}[\rho] = \int \epsilon_{xc}(\rho(\mathbf{r}), |\nabla\rho(\mathbf{r})|, ...)d\mathbf{r}. \tag{5.22}$$

we get the so-called generalized gradient approximations (GGA). There are a lot of different exchange-correlation functionals of the GGA type which are based on both physical (*ab initio*) insights and empirical data. In general, one can say that GGA improves on LDA when it comes to calculating bond lengths and energies, but for some systems where GGA fails, LDA leads to correct results because of some hazardous error cancellations.

5.3.2 Bloch states

The Kohn-Sham approach to DFT leads to an auxiliary independent particle system described by (5.14). To find the solutions for this system we can make use of the Bloch theorem (see Appendix A) and write the single particle wavefunctions from (5.14) as

$$\phi_{\mathbf{k}}(\mathbf{r}) = e^{i\mathbf{k}\cdot\mathbf{r}} u_{\mathbf{k}}(\mathbf{r}). \tag{5.23}$$

For large systems, the spectrum of $\mathbf{k}$-points is quasi continuous so that an integration over $\mathbf{k}$ is needed to calculate properties like the energy or density of the system. The integration can be restricted to the first Brillouin zone (due to the symmetry) but, since there is no trivial functional dependence between $\mathbf{k}$ and $\psi_{\mathbf{k}}$ or $\epsilon_{\mathbf{k}}$, one has to approximate these integrals by discretized versions on a finite, well chosen, grid of $\mathbf{k}$-points. The most widely used method to do this is due to Monkhorst and Pack who proposed to use uniform grids defined by

$$\mathbf{k}_{m_1,m_2,m_3} = \sum_{i=1}^{3} \frac{2m_i - q_i - 1}{2q}\mathbf{b}_i \qquad \text{with} \qquad m_i = 1, 2, ..., q_i \tag{5.24}$$

in which q_i denotes the number of discretization steps in the direction of the reciprocal lattice vector $\mathbf{b}_i$, so that there are $q_1q_2q_3$ $\mathbf{k}$-points in total. This number can be further decreased by taking the symmetry of the system into account by restricting the $\mathbf{k}$-points to the so-called irreducible Brillouin zone. The number of $\mathbf{k}$-points that is needed to get a good description of a system depends on the size and nature of the system, but also on the particular property under study. Therefore any calculation should be checked to give converged results with respect to the $\mathbf{k}$-point grid.

5.3.3 Basis set

As was the case for the Hartree-Fock orbitals, it is also more efficient to represent the Kohn-Sham orbitals with the help of a basis set instead of trying to represent them on a finite grid. Different basis sets have been proposed and it depends on the system , the desired accuracy and the computational limitations which basis set is the most appropriate. The *ab initio* code that will be used to perform the DFT calculations in this thesis, ABINIT, uses a plane wave basis set which has several advantages (and also disadvantages) as compared to others (see below).
Only the cell periodic part of the Bloch states (5.23), $u_{\mathbf{k}}(\mathbf{r})$, needs to be expressed in the plane wave basis. This can be done with a simple Fourier series (i.e. a discrete spectrum of plane waves) because the $u_{\mathbf{k}}(\mathbf{r})$ is periodic by construction,

$$u_{\mathbf{k}}(\mathbf{r}) = \sum_{\mathbf{G}} c_{\mathbf{k},\mathbf{G}} e^{i\mathbf{G}\cdot\mathbf{r}}, \tag{5.25}$$

where the summation is over all the reciprocal lattice vectors $\mathbf{G}$ of the system under study. In any practical calculation, the discrete, but infinite, basis set of plane waves has to be truncated. This can be done by demanding that $|\mathbf{G}| < G_{\max}$, which is roughly the same as stating that details in the structure of the wavefunction smaller than $\lambda = 2\pi/G_{\max}$ are ignored.

One advantage of a plane wave basis set is that it is easy to switch between real space and reciprocal space by fast Fourier transformations (FFT). Another is that the basis states stay fixed when one is relaxing the system, i.e. when one changes the position of the atoms. This should be contrasted to local basis sets where the basis changes when the atoms move. In the last case one can get artificial effects because space in not uniformly described by the basis. Furthermore it is easy to improve the plane wave basis set in as systematic way by including more plane waves corresponding to increasingly small wavelengths. The greatest disadvantage is the size of the basis set: compared to other basis sets, an enormous amount of basis functions is needed to describe realistic wavefunctions accurately. This problem can be partially solved by replacing the nuclear potentials of the system with pseudopotentials and the valence wavefunctions by smoothed wavefunctions.

5.3.4 Pseudopotentials and PAW

The single-electron wavefunctions of the valence states of atoms contain a lot of oscillations to satisfy the orthogonality condition with respect to the core states. These oscillations are confined to the core region which is not so important for the interaction between atoms and require a lot of plane waves for an accurate description. Therefore it would be very useful if these oscillations could be removed.

Different schemes have been devised to deal with this of which two will be used frequently in the following.

Pseudopotentials

The method that will be used most often here is the pseudopotential method. It consists of two steps: first the core electrons are removed and next, the valence wavefunctions are replaced by smoother pseudowavefunctions that require less plane waves for their description.

The wavefunctions of the core electrons of an atom are very compact and remain almost unaffected when the atom interacts with other atoms. Therefore it is not a serious approximation to take these core states as fixed and remove them from the calculation. The core electrons can be incorporated into the potential acting on the valence electrons. It should be noted that valence wavefunctions with different angular momentum will feel a different potential because of the orthogonality condition with respect to the core states. E.g. in case of a carbon atom the 2s valence state feels a different potential than the 2p valence state because the 2s state should be orthogonal to the 1s core state. The modified potential is consequently non-local (in the angular coordinates) and is called a pseudopotential.
The second step in the pseudopotential technique is to replace the full ionic core interaction potential (which includes the orthogonality condition) by a softer pseudopotential so that the resulting wavefunctions are smoother and nodeless. Furthermore, the pseudopotentials can be constructed in such a way that their scattering properties (i.e. the phase shifts) are identical to the real atomic potential to first order in energy [26]. This last requirement is fulfilled if the radial part of the smooth wavefunction (pseudowavefunction) is the same as the true wavefunction outside some core radius, r_c, and the matching of the pseudowavefunction and its derivative at r_c is continuous, while at the same time the (integrated) norm of the wavefunction inside the core region is preserved. An actual pseudopotential is constructed the other way around, i.e. one constructs a pseudowavefunction that fulfills these requirements and inverts the Schrödinger equation to get the pseudopotential.
There are many different ways to construct a suitable pseudowavefunction, but in this thesis the scheme due to Troullier and Martins [27] is always followed. Troullier and Martins proposed the following form for the smooth part of the radial part of the valence wavefunctions inside r_c,

$$\begin{aligned} R^l(r) &= r^l e^{p(r)} \\ p(r) &= c_0 + c_2 r^2 + c_4 r^4 + c_6 r^6 + c_8 r^8 + c_{10} r^{10} + c_{12} r^{12}. \end{aligned} \tag{5.26}$$

This form for the pseudowavefunctions is physically justifiable and contains 7 parameters to fullfill the 3 requirements mentioned above. The 4 extra parameters

are used to enhance the smoothness [27].

Projector augmented waves

Another method that is often applied in this thesis is the projector augmented wave (PAW) method due to Blöchl [28]. This method is more difficult to explain in detail so I will limit its discussion to the general ideas.
In contrast to the pseudopotential method, the PAW method keeps the core electrons (in a frozen state) and the full all-electron valence wavefunctions. The core wavefunctions are imported directly from all-electron calculations for the considered atom. The true wavefunctions are replaced by smooth wavefunctions inside some core radius r_c (similar as with the pseudopotential method). A linear transformation operator can be constructed to obtain the true wavefunction from the smooth one in the following way:

1. Find the true (all-electron) wavefunction solutions, ϕ_i, for the atom under study.

2. Transform the true wavefunctions into smoother ones, $\tilde{\phi}_i$, with the use of a pseudopotential method. These smooth wavefunctions are called the auxiliary wavefunctions or partial waves and the operator that determines the inverse transformation is defined as $\phi_i = T\tilde{\phi}_i = (1 + T_0)\tilde{\phi}_i$, in which T_0 is restricted to the core region.

3. The set of wavefunctions $\{\tilde{\phi}_i\}$ can be used to expand smooth valence wavefunctions, $\tilde{\psi}$, of the atom inside the core region in real calculations (i.e. when the atom interacts with other atoms). The smooth valence wavefunction can then be converted into the true wavefunction, ψ, by T. To make the expansion possible one defines so-called projectors $\tilde{p}_i$ by $\langle \tilde{p}_i | \tilde{\phi}_j \rangle = \delta_{ij}$, which are restricted to the core region.

To summarize, the true wave function, ψ, in a system is expanded into different terms,

$$|\psi\rangle = |\tilde{\psi}\rangle + \sum_i \left(|\phi_i\rangle - |\tilde{\phi}_i\rangle \right) \langle \tilde{p}_i | \tilde{\psi}_i \rangle. \tag{5.27}$$

Since ϕ_i, $\{\tilde{\phi}_i\}$, and $\tilde{p}_i$ are known from a separate all-electron calculation, the true wave function can be reconstructed from a smooth pseudowavefunction. This procedure is in principle exact, but the basis of auxiliary wavefunctions has to be truncated in a real calculation. In practice, the basis can be chosen very small (2 partial waves per angular momentum state) because the missing basis states are partially accounted for by the plane wave basis.

Overall the PAW method is more accurate and allows a smaller plane wave basis (i.e. a lower energy cutoff) than the pseudopotential method, but it is more complex and requires more care to implement.

Part III

Results

Chapter 6

Test Models and Preliminary Surveys

In this chapter, a variety of systems and methods is examined which will be useful to understand and interpret the results of the following chapters. The computational details of the performed calculations are only given insofar as they are important for the obtained results.

6.1 Graphene

Since graphene is the principal material in this thesis, it is important to have a detailed understanding of the influence of the computational methodology on its properties.

6.1.1 Electronic band structure

Different models for the electronic band stucture of graphene were already given in the introductory part on the electronic properties of graphene (Fig. 2.1). The most detailed information was given by the DFT band structure which is reproduced in Fig. 6.1. But the problem with this kind of pictures is that the large amount of details make it difficult to get all the information out of it. One solution to this problem is to decompose the total band structure (or the DOS) with the help of simpler models that allow the isolation of the different contributions to the total system. E.g. it was shown before that the valence and conduction band can be more or less reproduced by a nearest-neighbor TB approximation involving only the $2p_z$ orbitals of the 2 carbon atoms.
We can also include the $2s$, $2p_x$, and $2p_y$ orbitals in the TB-approximation. These

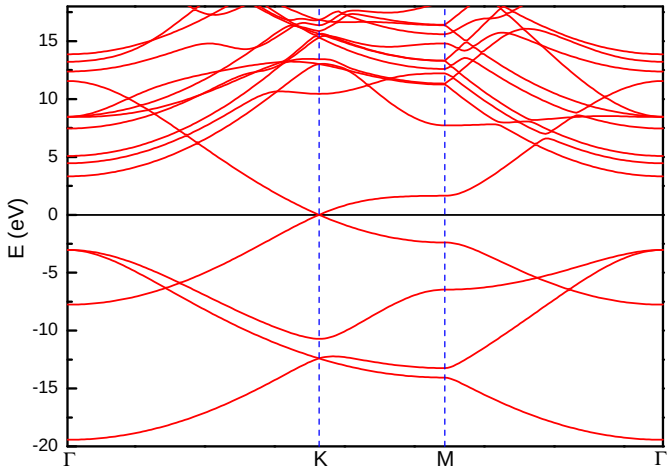

Figure 6.1. *The electronic band structure of graphene as calculated within the DFT formalism. The Fermi-level is put to 0.*

orbitals hybridize to form sp^2 orbitals that form a strong σ-bond network and provide an additional 6 bands to the electronic band structure, 3 below and 3 above the Fermi-level. But it can be seen that there are much more bands present at higher energies. Some of these bands are artificial and are related to the fact that we use periodic boundary conditions. These bands result from free energy states that are bounded by the graphene planes. These states are well described by wavefunctions of the form

$$\psi_{\mathbf{k}n}(\mathbf{r}) = \sqrt{\frac{2}{V}} e^{ik_x x} e^{ik_y y} \sin(n\pi z/L_z), \tag{6.1}$$

with energies

$$\epsilon_{\mathbf{k}n} = \frac{\hbar^2(k_x^2 + k_y^2)}{2m_e} + \frac{\hbar^2\pi^2}{2m_e L_z} n^2. \tag{6.2}$$

with L_z the interplane distance. To recognize these bands, $\epsilon_{\mathbf{k}n}$ in Fig. 6.1 they have to be represented in the same unitcell and shifted by the work function of graphene ($\sim$ 4.5eV). The free electron bands obtained in this way are shown in Fig. 6.2. The symmetry of the bands is easy to recognize in the band structure of graphene. The spacing between these bands is inversely proportional to the vacuum between two graphene layers (see (6.2)) and, consequently, the DOS resulting from the different calculations in this thesis will vary somewhat for the high-energy states.

6.1.2 The different carbon allotropes

It is also interesting to know how the two naturally occurring carbon allotropes, diamond and graphite, are described by our DFT formalism. In table 6.1 some

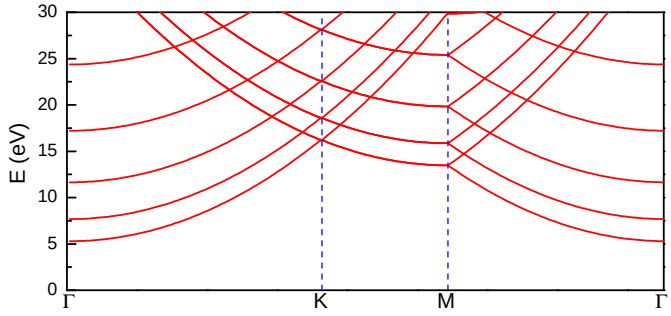

Figure 6.2. *Free electrons bands between graphene layers.*

properties of these materials are calculated within LDA and GGA and compared with experimental data.

Table 6.1. *Properties of graphite and diamond: the unit cell lengths (a, c) and C-C bond lengths, d_{CC}, are given in Å and the interlayer binding energy E_B in meV. The band gap of diamond, E_{gap}, and the formation energy with respect to graphite E_f are given in eV.*

		LDA	GGA	experiment
graphite	a	2.445	2.465	2.46
	c	6.712	8.642	6.67
	d_{CC}	1.412	1.423	1.42
	E_B	26	~ 2	61±5
diamond	a	3.529	3.578	3.57
	d_{CC}	1.529	1.549	1.54
	E_{gap}	5.629	5.568	5.48
	E_f	-0.010	0.122	~ 0.03

It can be seen from table 6.1 that LDA gives a better description of the interaction between graphene layers in graphite. The interlayer distance for LDA is relatively well reproduced, but the interlayer binding energy E_B in graphite is only half the experimental value. However, this is much better than the GGA result which gives a much too large interlayer distance and almost no binding at all. The better description by LDA is believed to be rather accidental and it has been suggested that it results from a cancellation of errors.
As is typical with LDA, the bond lengths are a little underestimated in comparison with the experimental results. The GGA results, on the other hand, give a more accurate description of the (inplane) lattice constants (a) in graphite and diamond. Note that the formation energy of diamond is negative in the LDA case although it is known from experiment that graphite is more stable than diamond [29]. This is a consequence of the underestimation of the interlayer van der Waals (vdW)

interaction energy in graphite as can be seen from table 6.1. If we include the vdW interaction energy[1], the formation energy of diamond is 25 meV which is close to the experimental result of ∼0.03 eV [29]. In agreement with earlier GGA calculations [30] it is found that GGA overestimates the formation energy of diamond.

6.2 Molecular systems

6.2.1 The simulation of molecules

The DFT code that is used for all the calculations in this thesis uses a plane wave basis and periodic boundary conditions in all 3 directions. This is clearly not an ideal case for the description of molecular systems. Therefore it is needed to test whether these systems are described accurately enough. To this purpose, several molecular systems will be examined. Some properties of H_2O, NH_3, NO_2, and H_2 molecules were calculated and they are shown in table 6.2.

Table 6.2. *Properties of some particular molecules. The bond length, d, is given in Å, the bond angle, θ, in degrees and the electric dipole moment, P, in Debye.*

molecule		d	θ	P
	LDA	0.769	-	0
H_2	GGA	0.752	-	0
	exp.	0.741	-	0
	LDA	0.990	104.9	1.883
H_2O	GGA	0.964	104.2	1.813
	exp.	0.958	104.5	1.85
	LDA	1.215	133.3	0.277
NO_2	GGA	1.199	134.1	0.272
	exp.	1.197	134.3	0.30
	LDA	1.028	107.7	1.490
NH_3	GGA	1.015	106.8	1.493
	exp.	1.017	107.8	1.42

The results makes clear that these molecules can be accurately described with the applied methodology and that GGA gives more accurate geometrical results than LDA. However, it is always necessary to check whether the artificial interaction between periodic images of the molecules is important for the obtained results

[1] This can be artificially realized by adding the difference between the experimental and LDA values for the interlayer binding energy to the formation energy.

or not. E.g. polar molecules will interact appreciably with their images and this can increase the total energy of the system. But when only energy differences are considered this will have a much smaller influence (see later).

6.2.2 Van der Waals interaction

One of the major shortcomings of the applied theoretical methodology is the neglection of van der Waals interactions. Although this can be a serious problem in some cases, especially when physisorption processes are considered, it is possible to estimate its importance and to put restrictions on the applicability of the calculated results.
The van der Waals interaction between two neutral subsystems is generally considered to consist of 3 kinds of interaction:

1. **dipole - dipole:** The permanent dipoles of the two subsystems interact with each other through an attractive or repulsive force that decreases as $\mathbf{r}^{-3}$ for large distances. This interaction usually dominates when permanent dipoles are present.

2. **dipole - induced dipole:** The permanent dipole of one of the subsystems induces a charge polarization (i.e. a dipole) in the other subsystem which leads to an attractive force.

3. **induced dipole - induced dipole:** This interaction, also called the London dispersion interaction, is the result of correlation effects between the charge distributions of the two subsystems. An instantaneous charge fluctuation in one subsystem results in a small dipole which induces a dipole in the other subsystem and vice versa. The resulting interaction is attractive and can be very important in cases where other (stronger) interactions are absent as is the case for e.g. noble gases at low temperatures.

The first and the second interaction are present in our model, but the third, which is usually the smallest, is not included.

The interactions that will be examined are primarily molecule/atom-graphene interactions. The first interaction is absent in that case, but, because the investigated molecules are usually polar, the second interaction is present. When the adsorbed molecules are non-polar, an underestimation of the adsorption energy can be expected. This has e.g. been demonstrated recently (2010) by vdW density functional studies (i.e. DFT studies where vdW interaction is explicitly incorporated) on the adsorption of diatomic halogen molecules on graphene [31]. The results of this study are shown in Fig. 6.3.

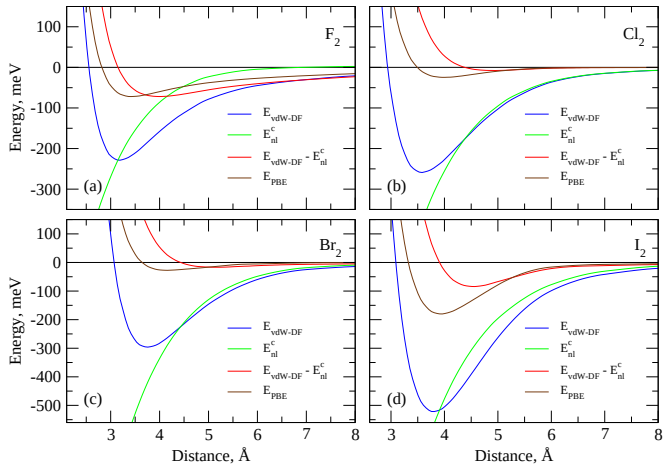

Figure 6.3. *Adsorption of different halogen molecules on graphene. The binding energy as a function of the distance between the molecule and graphene is shown for the vdW-corrected density functional (blue curve) and the PBE-GGA functional (brown curve). The other two curves are of no importance here. (Figure taken from Ref.[31].)*

In the figure the total energy is plotted as a function of the distance between the molecules and graphene for DFT-GGA calculations with (blue curves) and without (dark curves) vdW-interaction. It can be seen that our model, which corresponds to the dark curves, would give more or less the correct adsorption distance, but seriously underestimates the adsorption energy. This is not so bad as it looks because the focus will be more on the charge transfer which mostly depends on the distance and not on the energy.

Chapter 7

Molecular Adsorption on Graphene

In this chapter, the interaction between different molecules and graphene is investigated. It is useful to understand this interaction for several reasons: it is e.g. important to know how adsorbed gas molecules can have an influence on the performance of graphene devices for almost every application. The most important of these applications are those in which this influence is exploited to detect the presence of (e.g. toxic) molecules in the environment, i.e. gas sensors.

7.1 Detection of gas molecules on graphene

Before the theoretical investigation of adsorbed molecules on graphene, I will give a short review of some of the experiments that have stimulated a large part of the research performed in this thesis. The most important of these experiments is the one described in the paper of Schedin *et al.* which deals with the detection of individual gas molecules with an optimized graphene-based sensor [15]. In this paper, graphene-based gas sensors are made by incorporating graphene samples in a FET device in analogy with nanowire and nanotube sensors.

7.1.1 Graphene FET's for gas sensor applications

Graphene is an ideal material for use as the channel material in field effect transistors because of its flatness, high mobility charge carriers and ballistic transport at the micron level. The absence of a band gap in its electronic structure makes it impossible to turn off the FET which is a shortcoming that needs to be overcome if one wants to use graphene FET's for the usual applications in electronics. But for

other applications of graphene-based field effect devices (FED), such as gas sensors, this is a less important issue.

Graphene samples for field effect devices are usually prepared by mechanical exfoliation at the surface of an oxidized silicon wafer (scotch tape procedure) because of the superior quality of these samples. With the help of electron-beam lithography (Au/Ti) contacts can be made to graphene. A scanning electron micrograph of such a graphene field effect device is shown in the upper inset of Fig. 7.1. In this particular case 6 contacts were attached to allow for Hall measurements which are important to determine the sign of the charge carriers.

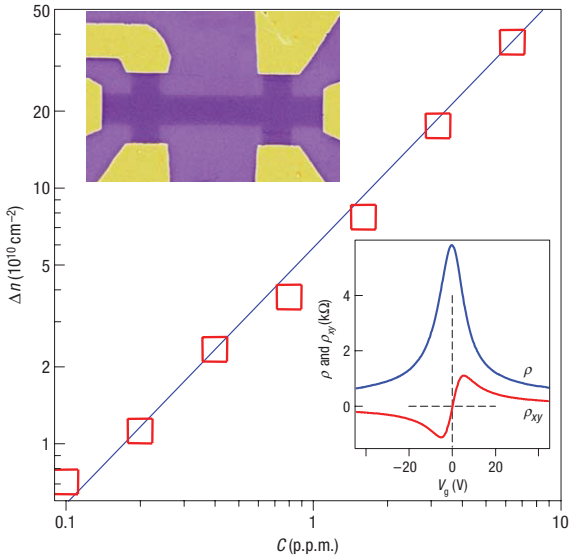

Figure 7.1. *Concentration, Δn, of chemically induced charge carriers in single-layer graphene exposed to different concentrations, C, of NO_2. Upper inset: Scanning electron micrograph of the experimental device (in false colors matching those seen in visible optics). The scale of the micrograph is given by the width of the Hall bar, which is 1 μm. Lower inset: Characterization of the graphene device by using the electric-field effect. (From Ref. [15])*

Longitudinal and Hall resistivity measurements as function of the gate voltage, V_g, show that graphene samples prepared in this way are in their undoped state (see lower inset of Fig. 7.1). The antisymmetry of the Hall resistivity with respect to V_g nicely demonstrates the continuous change from hole to electron charge carriers.

7.1.2 Gas detection with graphene sensor

For the detection of gas molecules, the FET device described above is put in a relatively large (5l) glass volume containing the chemical target molecules strongly diluted in an He or N_2 atmosphere. In Fig. 7.2 the response of the sensor to the chemicals NO_2, NH_3, H_2O and CO in concentrations of 1 part per million (p.p.m.) is shown. (From Ref. [15])

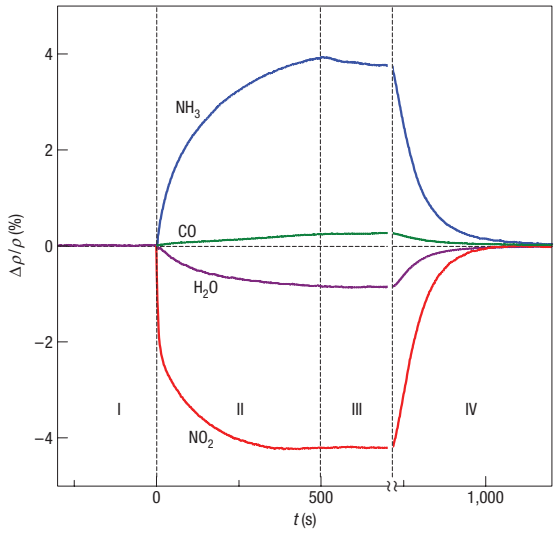

Figure 7.2. *Changes of the resistivity of graphene caused by the exposure to gases diluted in concentrations of 1 p.p.m. The sign of the change is chosen to resemble hole (-) and electron (+) doping. (From Ref. [15])*

It can be seen that the molecules cause easily detectable resistivity changes. The largest responses are observed for NO_2 and NH_3, but after some time saturation occurs which is caused by the finite amount of gas molecules in the experimental atmosphere. When the glass volume is evacuated (region III) the resistivity remains constant, indicating that the molecules are strongly attached. After the sample is heated to 150°C in vacuum (region IV), all the molecules detach from the surface and the graphene device is annealed back to its initial state. The sign of the charge carriers induced in the graphene layer by the different molecules is determined by simultaneous Hall measurements. NO_2 and H_2O appear to be acceptors while the other molecules act as donors. The positive and negative signs of the resistivity changes in Fig. 7.2 are chosen to resemble the electron or hole doping of the graphene sample. When the longitudinal and Hall resistivity of NO_2 and NH_3 are combined one can reproduce the ambipolar electric field effect of the graphene FET, shown in the lower inset of Fig. 7.1. This is demonstrated in Fig. 7.3 where

the charges are now chemically induced instead of with a gate voltage[1]. This makes it also possible to estimate the induced charge density by the adsorbates.

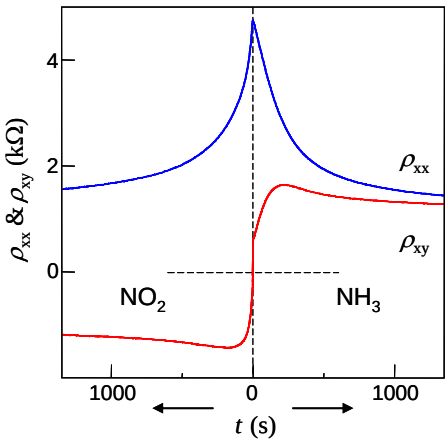

Figure 7.3. *Changes of the longitudinal and Hall resistivity of graphene as a function of time caused by the exposure to a continuous gas flow of NO_2 (left) and NH_3 (right) molecules. (From Ref. [15])*

7.1.3 Detection of individual NO_2 molecules

The detection limit of the sensor device used above can be estimated from the signal/noise ratio to be of the order of 1 p.p.b., which puts graphene at the same level of sensitivity as the most sensitive gas sensors. But to demonstrate the fundamental limit for the sensitivity of graphene-based sensors, Schedin *et al.* optimized their devices by using high driving currents to suppress the Johnson noise and annealing the samples close to the neutrality point. It can be seen from the lower inset of Fig. 7.2 or in Fig. 7.3 that the Hall resistivity, ρ_{xy}, is more sensitive to changes in the carrier concentration around the neutrality point than the longitudinal resistivity, ρ_{xx}. Therefore the changes in the Hall resistivity are used to examine the fundamental sensitivity of the graphene-based sensor. For this experiment the device was exposed to a vanishingly small leak of strongly diluted NO_2 and then evacuated again. The response of the Hall resistivity is shown in Fig. 7.4.
The Hall resistivity appears to change in discrete steps of which the direction depends strongly on the adsorption (gas leak) or desorption (evacuation) mode of the experiment (subfigure a). These steps can be linked with changes in the charge carrier concentration (see above). But since we know the dimensions of the sample

[1]The experimental setup was changed for this particular experiment: the fixed glass volume was replaced by a constant flow of gas molecules to avoid the saturation effect.

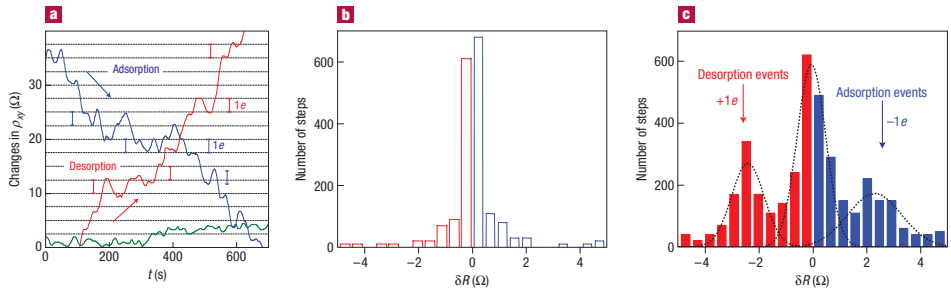

Figure 7.4. *Single molecule detection: a) The Hall resistivity during adsorption in strongly diluted NO_2 or desorption in vacuum. The green curve represents the noise level. b) Statistical distribution of the resistivity changes due to noise. c) Statistical distribution of the observed steps in (a). (From Ref. [15])*

($1\mu m^2$) this can be directly translated in an effective charge transfer per step which appears to be close to one electron (subfigure c). Therefore it seems that every step can be related to the adsorption of a single NO_2 molecule that withdraws one electron from the graphene sample.

7.2 DFT investigation of molecules on graphene

To fully exploit the possibilities of graphene sensors, it is important to understand the interaction between a graphene surface and adsorbing molecules. In this section the adsorption process on graphene is examined for the different molecules that were investigated in the experiment of Schedin *et al.*, discussed in the previous section. To this end, the adsorption of single H_2O, NH_3, CO, and NO_2 molecules on a pure graphene substrate is studied within the DFT formalism. The optimal adsorption positions and orientations of these molecules on the graphene surface are determined and the adsorption energies are calculated. Molecular doping, i.e. charge transfer between the molecules and the graphene surface, is analyzed in light of the molecular orbital theory which was treated before. The efficiency of the doping of the different molecules is determined and the influence of their magnetic moment is discussed.

7.2.1 Computational details

The first principles calculations are performed using density functional theory (DFT) which has been successfully used for the study of molecular adsorbates on single-walled (carbon) nanotubes (SWNT) [32–36]. All the DFT calculations were carried out with the ABINIT code [37], within the generalized gradient approximation (GGA) of Perdew, Burke, and Ernzerhof (PBE) [38]. The advantage of

GGA over the local density approximation (LDA) in this work is that the GGA will not lead to a strong binding of the molecules as in LDA. So if the molecules bind in GGA, they will definitely bind in a real system (and in LDA) too. The distance between the adsorbate and the graphene surface, however, will be somewhat overestimated and consequently the binding energy will be underestimated.
A plane wave basis set is used with a cutoff energy of 30 hartree and pseudopotentials of the Troullier-Martins type [27]. For the adsorption of the molecules NH_3, CO, and H_2O non-spin-polarized calculations are used, while for NO_2 spin-polarization is included. The total system consists of a 4×4 graphene supercell (32 C atoms) with a single molecule adsorbed to it (Fig. 7.5) and with a distance of 30 bohr (∼16 Å) between adjacent graphene layers. The sampling of the Brillouin zone is done with a $5 \times 5 \times 1$ Monkhorst-Pack [39] grid, which was tested to give converged results for all the calculated properties. For the calculation of the density of states (DOS) a $15 \times 15 \times 1$ Monkhorst-Pack grid is used and a Gaussian smearing of 0.005 hartree is applied.

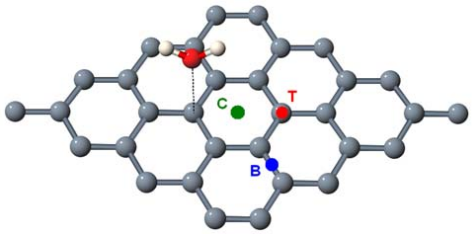

Figure 7.5. *H_2O on graphene. 4×4 supercell of graphene with adsorbed H_2O molecule. Three different adsorption sites that are used in the simulations are indicated: the center of a hexagon (C), on top of a carbon atom (T) and on the middle of a C-C bond (B).*

Charge transfers are calculated with the Hirshfeld charge analysis method [40], which is implemented in ABINIT. The Hirshfeld atomic charge Q_A for each atom is obtained by

$$Q_A = \int \frac{\rho_A^0(\mathbf{r})}{\sum_{A'} \rho_{A'}^0(\mathbf{r})} \rho(\mathbf{r}) d\mathbf{r}, \tag{7.1}$$

with $\rho(\mathbf{r})$ the calculated density and $\rho_A^0(\mathbf{r})$ the electron density computed for the isolated atom A and taken from Ref. [37]). From these atomic charges the charge transfer (ΔQ) can be deduced and it is therefore possible to determine the acceptor or donor character of the adsorbates. It should be noted that the size of the charge transfer depends on the method used to calculate it (see later).
The distance from the adsorbate to the graphene surface is calculated from the difference in weighted averages of the different atoms of the molecule and the carbon atoms of the graphene sheet, where the atomic number Z of the atoms is

used as a weight factor.[2]

7.2.2 Results

For each adsorbate three adsorption sites are considered, namely on top of a carbon atom (T), the center of a carbon hexagon (C) and the center of a carbon-carbon bond (B) (see Fig. 7.5) . For these positions, different orientations of the molecules are examined and the adsorption energy is calculated for all of them. The adsorption energy (E_a) is defined here as the energy of the isolated graphene sheet and isolated molecule minus the energy of the fully relaxed graphene sheet with the molecule adsorbed to it. These energies are not corrected for the dipole-dipole interactions which occur due to the finite size of the supercells. However, these energies mainly cancel, resulting in corrections of the order of 2 meV in the worst cases (H_2O and NH_3). This has no influence on any of the conclusions, so I decided to neglect them.
The strength of the molecular doping is discussed in light of the density of states and the highest occupied and lowest unoccupied molecular orbitals (HOMO and LUMO) of the adsorbate. The position of these orbitals, visible as peaks in the DOS, is practically independent of the orientation and adsorption site of the molecule, so only the total DOS for one geometry per molecule is shown. We can now distinguish two charge transfer mechanisms: i) a charge transfer can occur due to the relative position in the DOS of the HOMO and LUMO of the adsorbate. If the HOMO is above the Fermi level of pure graphene (the Dirac point), there is a charge transfer to graphene. If the LUMO is below the Dirac point, charge will transfer to the molecule. ii) The charge transfer between adsorbate and graphene is also partially determined by the mixing (hybridization) of the HOMO and LUMO with the graphene orbitals. As seen before, this mixing scales with the overlap of the interacting orbitals and the inverse of their energy difference.
It is more difficult to discuss the adsorption energy using qualitative molecular orbital theory because of the large amount of possible interacting orbitals present in graphene. The investigation starts with the non-magnetic molecules H_2O, NH_3, and CO, followed by the paramagnetic ones, NO_2 and NO. The molecules are discussed in the order of increasing complexity of their charge transfer mechanism.

H_2O on graphene

The following orientations of the H_2O molecule with respect to the graphene surface are examined: starting from the O atom the H-O bonds pointing up (u), down (d) or parallel to the graphene surface (n). Another orientation (v) was suggested in

[2]It is more common to take the mass of the atoms as the weight factor, but this seems quite meaningless in a Born-Oppenheimer approximation where masses are irrelevant.

a theoretical study, based on an empirical method, of the adsorption of H_2O on graphite [41]. This orientation has one O-H bond parallel to the surface and the other one pointing to the surface.
All properties were found to be almost invariant with respect to rotations around the axis perpendicular to the surface and through the oxygen atom, and therefore this orientation will not be discussed. The results of the calculations are given in table 7.1.

Table 7.1. *H_2O on graphene: the adsorption energy (E_a), the distance of H_2O above the graphene surface (d), and the charge transfer from the molecule to graphene (ΔQ) for ten different geometries.*

Position	Orientation	E_a(meV)	d(Å)	ΔQ(e)
B	u	18	3.70	0.021
T	u	19	3.70	0.021
C	u	20	3.69	0.021
B	n	24	3.55	0.013
T	n	24	3.56	0.015
C	n	27	3.55	0.014
B	d	18	4.05	-0.009
T	d	19	4.05	-0.009
C	d	19	4.02	-0.010
C	**v**	**47**	**3.50**	**-0.025**

From table 7.1 it can be seen that all the adsorption energies are small (20-50 meV, which is partially a consequence of the calculation method. This is not very important because the adsorption energies are only used to compare the different geometries and to find the best position and orientation of the molecule for which we need only relative values. Table 1 also shows that the adsorption energy is primarily determined by the orientation (u, d, n, v) and to a lesser degree by the position (C, B, T) of the molecule: the energy differences are 5-6 meV with respect to the orientation, but they vary with only about 1-2 meV when changing the position. This difference in importance of position and orientation is even more pronounced when we look at the charge transfers. If the O atom points to the graphene surface, there is a (small) charge transfer to graphene, but if the H atoms point to the surface there is a small charge transfer to the water molecule. This is a consequence of the form of the HOMO and LUMO of H_2O and their relative position with respect to the Dirac point (see Fig. 7.6).
The HOMO ($1b_1$) is completely located on the O atom, but the LUMO ($4a_1$) is mostly located on the H atoms. In the u (and n) orientation the HOMO plays the dominant role and donates, through a small mixing with graphene orbitals above

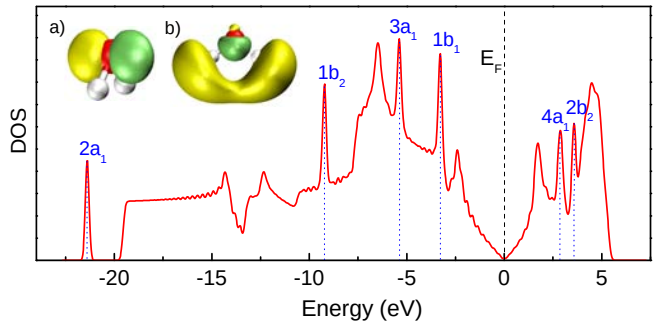

Figure 7.6. *H_2O on graphene. Inset: (a) the HOMO and (b) the LUMO of H_2O (the H atoms are white and the oxygen atom is red; green and yellow indicate different signs of the orbital wavefunction). Main panel: DOS of H_2O on graphene. The blue dotted lines show the positions of the molecular orbitals of H_2O.*

the Fermi level, some charge to graphene. There is also a (stronger) mixing with the orbitals below the Dirac point, because they are closer in energy, but this does not induce any charge transfer because all these orbitals are filled. In the d and v orientation, the LUMO of H_2O interacts stronger with the surface and is able, through a small mixing with the graphene orbitals below the Dirac point, to accept some charge from graphene. There is also a stronger mixing with orbitals above the Dirac point now, but this does not induce any charge transfer because all these orbitals are empty. In the n orientation it is again the HOMO that will interact stronger, but now there is also some interaction with the LUMO. There will be a charge transfer from the molecule to graphene, but, because of the interaction with the LUMO, it will be smaller.
In the experiment described above [15] one finds that H_2O acts as an acceptor on graphene which is in accordance with these theoretical results where it is found that the acceptor character (C,v) is energetically favored on perfect graphene.

NH_3 on graphene

Two orientations of the ammonia molecule are investigated, one with the H atoms pointing away from the surface (u) and the other with the H atoms pointing to the surface (d). All properties were again found to be almost invariant to rotations around the axis perpendicular to the surface and through the nitrogen atom. The results of the calculations are given in table 7.2. The adsorption site and the orientation are now seen to be of the same importance for the adsorption energy. The charge transfer, however, is solely determined by the orientation of the NH_3 molecule.
There is a small charge transfer from the molecule to the graphene surface of 0.03 e in the u orientation and there is (almost) no charge transfer in the d orientation.

Table 7.2. *NH_3 on graphene: the adsorption energy (E_a), the distance of NH_3 above the graphene surface (d), and the charge transfer from the molecule to graphene (ΔQ) for six different geometries.*

Position	Orientation	E_a(meV)	d(Å)	ΔQ(e)
B	u	21	3.86	0.026
T	u	20	3.86	0.026
C	**u**	**31**	**3.81**	**0.027**
B	d	15	4.08	0.001
T	d	16	3.97	0.000
C	d	25	3.92	-0.001

We can see how this comes about by looking at the HOMO ($3a_1$) and LUMO ($4a_1$) of the NH_3 molecule (Fig. 7.7(a) and (b)). In the u orientation, the HOMO is the only orbital that can have a significant overlap with the graphene orbitals and thus can cause charge transfer. As a consequence the NH_3 molecule will act as a donor. In the d orientation, both HOMO and LUMO can cause charge transfers which are similar in magnitude but in opposite directions. The net charge transfer is therefore close to 0.
The u orientation is energetically favored which explains the donor character as observed experimentally [15].

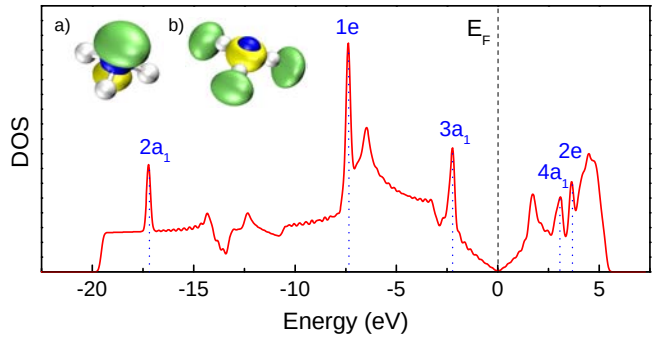

Figure 7.7. *NH_3 on graphene. Inset: (a) the HOMO and (b) the LUMO of NH_3 (the N atom is blue and the H atoms are white). Main panel: DOS of NH_3 on graphene.*

I also performed LDA calculations for the adsorption of NH_3 on graphene. The results of these are similar for the charge transfer, but the adsorption energy is much larger ($\pm$100 meV). The real adsorption energy lies probably between the two approximate values obtained through GGA and LDA. This is consistent with the experimental observation [15] that the adsorbates can be removed from the surface by annealing at 150°C.

CO on graphene

Three different orientations were used for the CO molecule. Two with the molecule perpendicular to the surface, with the O atom above the C atom (u) and the other way around (d), and one parallel to the surface (n).

Table 7.3. *CO on graphene: the adsorption energy (E_a), the distance of CO above the graphene surface (d), and the charge transfer from the molecule to graphene (ΔQ) for seven different geometries.*

Position	Orientation	E_a(meV)	d(Å)	ΔQ(e)
B	u	10	3.75	0.019
T	u	10	3.75	0.019
C	u	13	3.73	0.019
T	d	8	3.72	0.009
C	d	10	3.70	0.010
B	n	14	3.74	0.013
C	**n**	**14**	**3.74**	**0.012**

From table 7.3 it can be seen that the CO molecule always acts as a donor. The size of the charge transfer only depends on the orientation of the molecule with respect to the surface. The differences in charge transfer are due to differences in orbital overlap between the HOMO (5σ) of the CO molecule and graphene. The LUMO (2π) seems to play a less important role in the doping process although it is closer to the Dirac point than the HOMO. To understand this one has to take into account the spatial extension and symmetry of this orbital. The LUMO is less extended than the HOMO so, without taking into account the symmetry, the overlap will be much larger for the HOMO. Remember that the interaction between orbitals scales as $S^2/\Delta E$ when the energy difference, ΔE, is large, so that the overlap is more important than the energy difference. Furthermore, the DOS below the Dirac point originates from (mostly) bonding combinations of the p_z atomic orbitals of the C atoms of graphene. The DOS above the Dirac point is mostly due to anti-bonding combinations. The completely anti-symmetric LUMO will therefore interact stronger with the DOS above the Dirac point which does not cause any doping.
The HOMO is thus the more important orbital and the charge transfer is consequently always to graphene. Because the HOMO is mainly located on the C atom, the charge transfer is largest when the C atom is closest to the surface (u orientation), smallest when the O atom is closer to the surface (d orientation) and intermediate when both atoms are at an (almost) equal distance from the surface (n orientation).

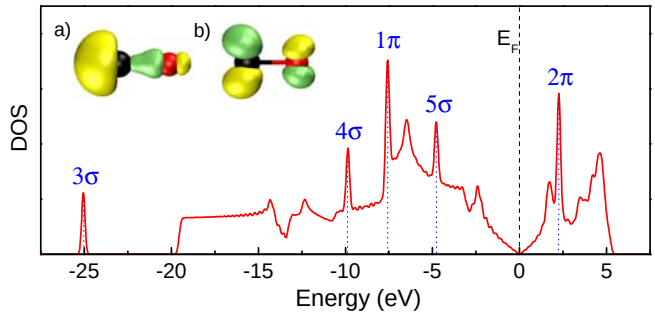

Figure 7.8. *CO on graphene. Inset: (a) the HOMO and (b) the LUMO of CO (the C atom is black and the O atom is red). Main panel: DOS of CO on graphene.*

NO_2 on graphene

In Ref. [42] it was stated that adsorbates with a magnetic moment generally induce a larger doping. Therefore the attention will now be turned to paramagnetic molecules. The first one is NO_2 which has, in a spin-polarized calculation, an energy that is 0.4 eV smaller as compared to an unpolarized one and therefore is paramagnetic. Three different orientations of the NO_2 molecule are examined: starting from the N atom, the N-O bonds pointing up (u), down (d) or parallel to the graphene surface (n).

Table 7.4. *NO_2 on graphene: the adsorption energy (E_a), the distance of NO_2 above the graphene surface (d), and the charge transfer from the molecule to graphene (ΔQ) for six different geometries.*

Position	Orientation	E_a(meV)	d(Å)	ΔQ(e)
B	**d**	**67**	**3.61**	**-0.099**
T	d	65	3.61	-0.099
C	d	63	3.64	-0.098
B	u	55	3.83	-0.089
T	u	55	3.93	-0.090
C	n	67	3.83	-0.102

The LUMO ($6a_1,\downarrow$) of NO_2 is located 0.3 eV below the Dirac point (Fig. 7.9). This induces a large charge transfer to the molecule. But there are also some NO_2 orbitals close enough to the Dirac point to cause some charge transfer in the opposite direction through orbital mixing (especially the HOMO ($6a_1,\uparrow$)). The latter charge transfer is, however, much smaller than the first so that the total charge transfer is to the molecule.

Note that an experimental value of about $1e$ was found per adsorbed NO_2 molecule on graphene [15]. The reason for this apparent discrepancy with the theoretical

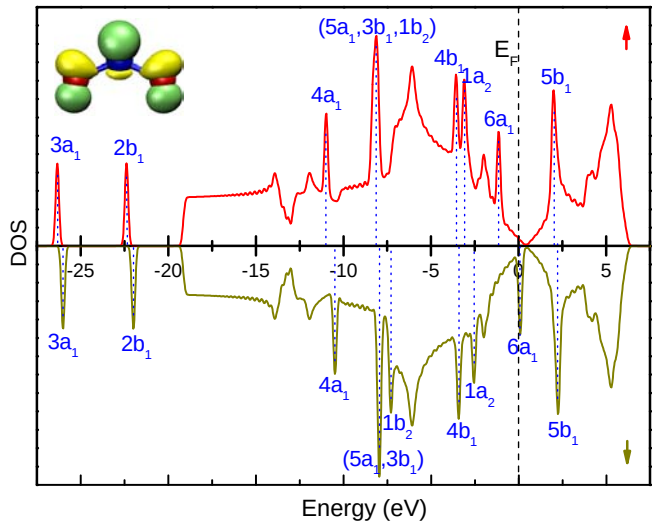

Figure 7.9. *NO_2 on graphene. Inset: HOMO and LUMO of NO_2 (the N atom is blue and the O atom is red). Main panel: spin-polarised DOS of NO_2 on graphene.*

results obtained here is treated in the next chapter.

NO on graphene

To test whether or not there is always strong doping by paramagnetic molecules another one, namely NO, is investigated. For NO a spin polarized calculation gives an energy that is 0.3 eV lower than a non-spin-polarized one, so NO is indeed a paramagnetic molecule. The same orientations and notations as for the CO molecule are used (replace C with N). Contrary to the claim made in Ref. [42], it is found that NO does not induce any strong doping. The charge transfers are an order of magnitude smaller than in the case of the NO_2 molecule (see table 7.5) which is comparable to the non-magnetic molecules. Physically, we can understand this if we compare the DOS of the adsorbates NO (Fig. 7.10) and NO_2 on graphene. For NO_2 adsorbed on graphene, the LUMO is situated 0.3 eV below the Dirac point of graphene. This induces a strong doping. In the case of NO (Fig. 7.10) the HOMO is degenerate ($2\pi_x$, $2\pi_y$) and is half filled (so it is also the LUMO) and lies only 0.1 eV below the Dirac point. This induces a very small charge transfer from graphene to NO, but, due to its small strength, it can be (over)compensated by orbital mixing. The HOMO/LUMO of NO can, because it is half filled, cause charge transfer in both directions by mixing with the graphene orbitals below and above the Dirac point. But, as in the case of the LUMO of CO, it interacts mostly with the latter. So the orbital mixing leads to charge transfer to graphene.
We see from table 7.5 that the charge transfer due to orbital mixing always over-

Table 7.5. *NO on graphene: the adsorption energy (E_a), the distance of NO above the graphene surface (d), and the charge transfer from the molecule to graphene (ΔQ) for six different geometries.*

Position	Orientation	E_a(meV)	d(Å)	ΔQ(e)
C	u	16	4.35	0.006
T	u	14	4.35	0.006
C	d	13	4.11	0.007
T	d	11	4.27	0.005
C	n	28	3.71	0.018
B	**n**	**29**	**3.76**	**0.017**

compensates the small transfer due to the position of the HOMO/LUMO, so NO always act as a donor.[3] It can be noticed that there are large differences in ΔQ and in the distance d. They are obviously correlated because a smaller distance between adsorbate and graphene leads to a larger orbital overlap and consequently to more orbital mixing (i.e. a larger charge transfer).

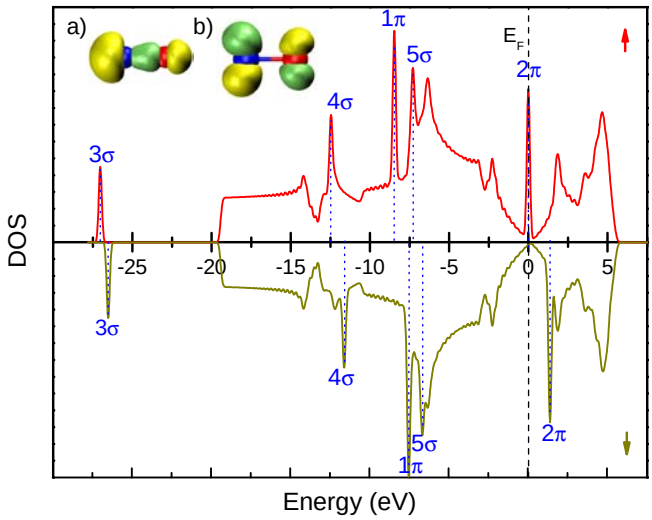

Figure 7.10. *NO on graphene. Inset: (a) 5σ orbital and (b) HOMO/LUMO of NO (the N atom is blue and the O atom is red). Main panel: spin-polarized DOS of NO on graphene.*

The differences in the distance can be explained by the overlap of the 5σ orbital. The position of this orbital is very close in energy to that part of the graphene DOS that originates from the (bonding) combinations of carbon p_z orbitals around

[3] This result will be corrected later.

the Γ point. Mixing of these orbitals induces a net energy shift upwards so they repel each other strongly. The geometry of the 5σ orbital gives a large overlap in the u orientation, a smaller overlap in the d orientation and the smallest overlap in the n orientation. This gives a simple explanation for all the differences found from the calculations.

7.2.3 Summary and conclusions

The charge transfer between the considered adsorbates and graphene is found to be almost independent on the adsorption site but it does depend strongly on the orientation of the adsorbate with respect to the graphene surface. I compared two paramagnetic molecules, NO_2 and NO, and found that NO_2 induces a relatively strong doping (-0.1e), but NO does not (<0.02e). This is in contrast to Ref. [42] where it was claimed that paramagnetic molecules are strong dopants which was found indeed to be the case for NO_2 but not so for NO.

Table 7.6. *Summary of results.*

Adsorbate	Theory	Experiment [15]	E_a (meV)	ΔQ(e)
H_2O	acceptor	acceptor	47	-0.03
NH_3	donor	donor	31	0.03
CO	donor	donor	14	0.01
NO_2	acceptor	acceptor	67	-0.10

For the considered adsorbates the sign of the charge transfer agrees with what was found experimentally (see table 7.6) in Ref. [15]. It was shown that these charge transfers can be understood from two charge transfer mechanisms. In NO_2 on graphene it is mainly due to the position of the LUMO below the Dirac point, for all the other studied adsorbates it is caused by the mixing of the HOMO or LUMO orbitals with the orbitals of graphene. The strength of this hybridization can be deduced from the geometrical orientation of the HOMO and LUMO orbitals with respect to the graphene surface.
The strength of the charge transfer and the binding energies must be seen in light of the used approximations (GGA) and the method of calculation (Hirshfeld method), which probably lead to an underestimation. The trends and relative values, on the other hand, are much more trustworthy. E.g. for water molecules the size of the charge transfer becomes much smaller when calculated with a more advanced Hirshfeld method (see next chapter), although the direction of the charge transfer remains the same for different orientations of the H_2O molecule.
The results are also in good agreement with theoretical studies of the adsorption of molecules on large SWNT's in e.g. Ref. [32]. This suggests that some of the

knowledge of adsorption on nanotubes should be transferable to graphene.

Chapter 8

Charge Transfer Calculations

The use of carbon nanotubes [43–48] and graphene [15] as very sensitive gas sensors has stimulated a lot of theoretical work on this subject [32, 33, 35, 36, 42, 49–51], as described in the previous chapter. Through ab initio calculations, researchers have investigated the adsorption properties of these carbon materials and looked for the mechanisms behind their good sensing capabilities. Although the ab initio calculations were able to provide good qualitative agreement with experiment, e.g. whether the gas molecules act as electron donors or acceptors, a large variation in the size of the doping is found between different theoretical calculations. For example, the calculated charge transfer between a (10,0) single-walled carbon nanotube (SWNT) and a NO_2 molecule varies from $-0.015e$ [33] to $-0.10e$ [36], an order of magnitude difference! The size of the doping is, however, a crucial factor determining the sensitivity of the gas sensor. In this chapter the causes of these discrepancies will be investigated. Two major computational aspects that vary among the different theoretical studies are the charge analysis method used to calculate the charges and the size of the investigated systems. Another influence might have been the choice for the exchange-correlation functional, but this appears to have only a very small influence on the charges.

8.1 Charge analysis methods

To calculate the charge transfer from a molecule to a surface, one needs a physically meaningful and transparent approach to divide the electron density between them. In this section, several methods for calculating effective charges will be investigated and some of them appear to be able to describe the charge transfer more accurately than the Hirshfeld method that was used in the previous chapter.
A variety of methods has been developed to calculate the effective charges of atoms

in a molecule, such as Mulliken's [52] or Bader's [53] charge analysis method. It should be noted that these effective charges are necessarily arbitrary because a molecule is not the sum of its atomic components combined with charge transfers among the different atoms. This can be simply demonstrated by the interaction between two atomic orbitals as given in the qualitative molecular orbital theory. Consider two atoms, a and b, with atomic orbitals ϕ_a and ϕ_b, respectively. Suppose these two orbitals are occupied with one electron each and that their interaction results in the following bonding (molecular) orbital,

$$\Phi_B = c_a\phi_a + c_b\phi_b, \tag{8.1}$$

with a density given by[1]

$$\rho = \Phi_B^2 = c_a^2\phi_a^2 + 2c_ac_b\phi_a\phi_b + c_b^2\phi_a^2. \tag{8.2}$$

This density corresponds to the charge density since Φ_B is the only occupied orbital. It is now clear that the partial density $c_a^2\phi_a^2$ should be attributed to atom a and the density $c_b^2\phi_a^2$ to atom b, but what about the term $2c_ac_b\phi_a\phi_b$? A simple solution, proposed by Mulliken [52], is to divide this term equally between the two atoms but this is obviously an arbitrary choice. On the other hand, this does not mean that it is unreasonable to talk about charge transfers altogether. If ϕ_a has a lower energy than ϕ_b, c_a will be larger than c_b and a charge transfer to atom a is guaranteed. The exact value of this charge transfer, however, is not specified and it depends on the particular choice that is made to divide the total system into different components corresponding to the different atoms. There are some obvious restrictions on this division if a charge analysis method is to have any physical relevance and meaning: e.g. at infinite separation, when the orbital overlap is zero, the calculated charge transfer should have the correct behavior.
Several strategies to calculate the effective (partial) charges in a system have been devised of which most are based on analyzing the wavefunction or the electronic density. But it is also possible to make use of some special features of particular systems to estimate the partial charges such as dipoles or magnetic moments (see below).

8.1.1 Wavefunction based methods

In spite of its limited accuracy, the most widely used wavefunction based method is the Mulliken population analysis which was described above. It is widely used because of its simplicity and in some cases the charges can be calculated at no extra computational costs. This is e.g. the case when one makes use of a basis set of functions that are localized on the different atoms of the system such as

[1] supposing that the orbitals and constants c_a and c_b are real

atomic orbitals, gaussians, etc. In this case the different coefficients, $c_1, c_2, ...$, are calculated when the wavefunction is determined and the charge per atom can be deduced from this since every coefficient belongs to a particular atom. However, the ABINIT code that is used for the DFT calculations uses a plane wave basis so that there is no particular benefit in trying to use a Mulliken charge analysis here.

8.1.2 Density based methods

When performing calculations in the DFT formalism, it is particularly interesting to use a density based charge analysis method because the density is the central object of the calculation.

Bader charges

The Bader charge analysis, introduced by Bader in 1991 [53], is a method which is intuitively very plausible but it is actually rather difficult to apply in practice. It makes use of the concept of a zero-flux surfaces which surround each atom. A zero-flux surface is a closed[2] surface $S(\mathbf{r}_s)$ defined by

$$\nabla\rho(\mathbf{r}_s) \cdot n(\mathbf{r}_s) = 0, \tag{8.3}$$

where $n(\mathbf{r}_s)$ is the unit vector normal to the surface $S(\mathbf{r}_s)$. In other words, the surface cuts the density at its extremes (usual minima) between the atoms (see Fig. 8.1). The density enclosed by these surfaces determines the charge of the different atoms. Although the calculation of the zero-flux surfaces is rather costly and nontrivial to implement, this is probably the most used advanced method to calculate charges in molecules and solids.

Hirshfeld charge analysis

The Hirshfeld method was introduced in the previous chapter to calculate the charge transfers between several molecules and graphene. It will be treated here in more detail because it forms the basis of the more advanced methods described below.
Compared to the Bader charge analysis the Hirshfeld method is remarkably simple to implement and the idea behind it is at least equally plausible. The total density of the system is divided into atomic parts by

$$\rho_A(\mathbf{r}) = \frac{\rho^0_A(\mathbf{r})}{\sum_{A'} \rho^0_{A'}(\mathbf{r})}\rho(\mathbf{r}), \tag{8.4}$$

with $\rho(\mathbf{r})$ the total density and $\rho^0_A(\mathbf{r})$ the electron density of a neutral isolated atom A. The summation in the denominator runs over all the atoms of the system. The

[2] the closure can also be at infinity.

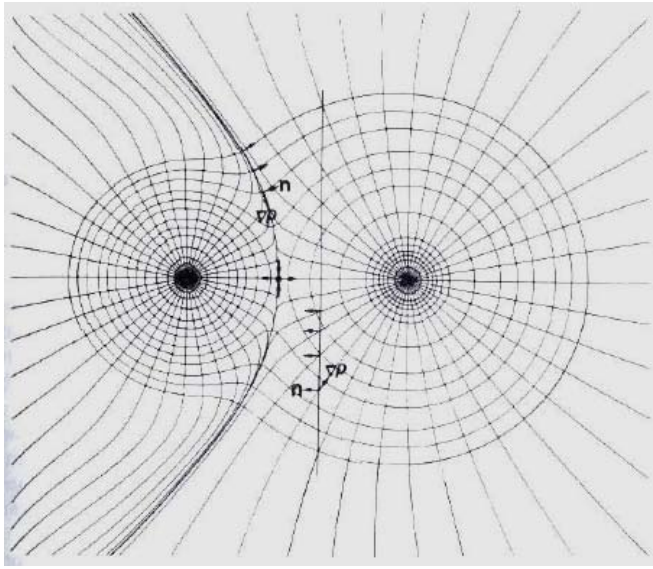

Figure 8.1. *Bader charge analysis: the separation of the density of NaCl with a zero-flux surface is indicated by the dark line. The surface divides space in two and the integrated densities of the two subspaces correspond to the charges on the Na and Cl atom.*

idea behind this is that the total density of a bonded system, ρ, is similar to the density that results from a summation over the densities of all the isolated atoms, $\rho^0(\mathbf{r}) = \sum_{A'} \rho^0_{A'}(\mathbf{r})$. The contribution of every atom A' to this density $\rho^0(\mathbf{r})$ is unambiguously determined, by the construction of this density, to be $\rho^0_{A'}(\mathbf{r})$. To get a particular $\rho^0_A(\mathbf{r})$ again out of $\rho^0(\mathbf{r})$, all that is needed is to multiply $\rho^0(\mathbf{r})$ by a weight function $W_A(\mathbf{r})$ defined by

$$W_A(\mathbf{r})\rho^0(\mathbf{r}) \equiv \frac{\rho^0_A(\mathbf{r})}{\sum_{A'} \rho^0_{A'}(\mathbf{r})}\rho^0(\mathbf{r}) = \rho^0_A(\mathbf{r}). \tag{8.5}$$

The same weight functions $W_{A'}$ are now used to find the contributions of the different atoms to the total density of the bonded system, ρ, which results in the formula (8.4).

The Hirshfeld charges appear in several ways to be more physically justified than the Bader charges. When the densities of neutral atoms are added together, the Hirshfeld analysis gives, by construction, the intuitively correct result that there is no charge transfer[3]. There is however no reason that this should also be the case for the Bader charges for this artificial system. Furthermore, the density at every point in space is attributed to all the atoms (weighted by $W_A(\mathbf{r})$) in the Hirshfeld analysis while it is completely attributed to a single atom in the Bader analysis.

[3]The Mulliken charges should also give the correct result.

The iterative Hirshfeld method

The Hirshfeld method has one major shortcoming: the fact that the density is divided on the basis of neutral atoms is a very arbitrary choice. Imagine e.g. the case of a LiF molecule (this example comes from [54]). This is a highly ionic system. When one calculates the Hirshfeld charges starting from the densities of the neutral Li and F atoms one finds a charge of $0.57e$ on the Li atom and -0.57e on the F atom. However, if one starts with the densities of a Li^+ and a F^- atom, the charges are $0.98e$ and -0.98e respectively. The last case is more consistent than the first: $0.0e$ charge leads to $0.57e$ while $1.0e$ leads to $0.98e$.
This seems to lead to an obvious suggestion to improve the Hirshfeld method but, in fact, it was only made in 2007, 30 years after Hirshfeld first proposed his method [54]. This suggestion was as follows: first calculate the charges with the normal Hirshfeld method. Put these charges on isolated atoms and use the resulting densities to calculate the Hirshfeld charges again. These steps can be repeated until the input and output charges have converged. In this way any arbitrariness in the choice of initial densities is removed except for the fact that we take densities of isolated atoms. But this is exactly what was required since the purpose was to divide the total charge (density) among these different atoms.
The charges resulting from the iterative Hirshfeld method will be called Hirshfeld-I charges, as proposed in Ref. [54].

Modified Hirshfeld method

The Hirshfeld method can be modified further to our needs if it is realized that to know the charge transfer between two systems, such as a molecule and graphene, it is not necessary to know the charges on all the different atoms. All that is needed is the total charge of the molecule and the total charge of graphene. Therefore it might be better to take the total densities of these two subsystems (i.e. the molecule and the graphene layer) to construct the weight functions defined in (8.5). This gives a different result from the atom-based Hirshfeld method because the weight functions are different,

$$W_a^H(\mathbf{r}) = \frac{\sum_{A'} \rho^0_{A'}(\mathbf{r})}{\sum_{A'} \rho^0_{A'}(\mathbf{r}) + \sum_{B'} \rho^0_{B'}(\mathbf{r})} \neq \frac{\rho^0_a(\mathbf{r})}{\rho^0_a(\mathbf{r}) + \rho^0_b(\mathbf{r})} = W_a^{mH}, \qquad (8.6)$$

where a and b are the two subsystems and $\{A'\}$ and $\{B'\}$ denote the atoms in these subsystems. W_a^H is the weight function for subsystem a as found for the atomic Hirshfeld method and W_a^{mH} for the modified version of this method based on the total densities of the subsystems, $\rho^0_a(\mathbf{r})$.
In practice, the procedure looks as follows: first the total system is relaxed completely and the total electronic density is calculated. Then the density of the

molecule and the graphene layer are calculated separately in the same configuration as in the total relaxed system. These densities can now be used in the Hirshfeld-I method instead of the separate atomic densities. When the charges of the two subsystems are made self-consistent in this way, they will be referred to as the modified Hirshfeld-I charges.

8.1.3 Testing the different methods

It is now time to examine the accurateness of the different charge analysis methods by applying them to a concrete example. For this, the charge transfer between the paramagnetic molecule NO_2 and graphene is considered. This system was already studied in the previous chapter, so the results obtained there can be used again. The charge transfer for the most stable adsorption geometry is calculated with the different methods and the results are given in table 8.1.

Table 8.1. *The charge transfer from graphene to NO_2 calculated with different methods.*

method	charge transfer (e)
Hirshfeld	-0.099
modified Hirshfeld	-0.161
modified Hirshfeld-I	-0.181
Bader	-0.212

The direction of the charge transfer is consistent, but the size of the charge transfer seems to be strongly dependent on the calculation scheme: there is a difference of a factor of 2 between the highest and the lowest one. How is it possible to decide which value is most physically relevant? One way to make a physically meaningful way to estimate the charge transfer can be obtained when a simple MO picture of NO_2 is considered. NO_2 is a paramagnetic molecule and has, consequently, an unpaired electron in one molecular orbital. This partially occupied MO (POMO) can be expected to be dominant in any charge transfer from or to the molecule. A schematic picture of this orbital is given in Fig. 8.2b.

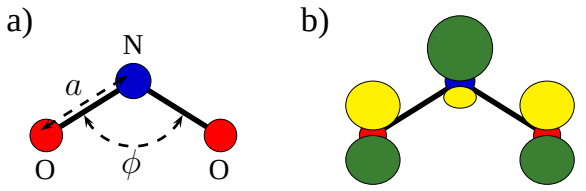

Figure 8.2. *NO_2 molecule: a) schematic view in which the N-O bond length, a, and the bond angle, ϕ, are indicated. b) schematic picture of the POMO ($6a_1$) of NO_2.*

It can be seen that there is an anti-bonding interaction between the N and O atoms while the O-O interaction is bonding. Therefore the geometry of the NO_2 molecules will change when the occupation of the POMO changes. Adding (removing) charge to (from) the POMO will increase (decrease) the N-O bond length, a, and decrease (increase) the bond angle, ϕ. So the bond length and bond angle are related with the charge of the molecule. If we know this relation, we can get an estimate of the charge transfer by calculating the bond length or angle of the molecule after adsorption on graphene. The bond length/angle-charge relation is easily obtained by the addition of charge to an isolated molecule and the subsequent observation of the geometrical changes, as depicted in Fig. 8.3.

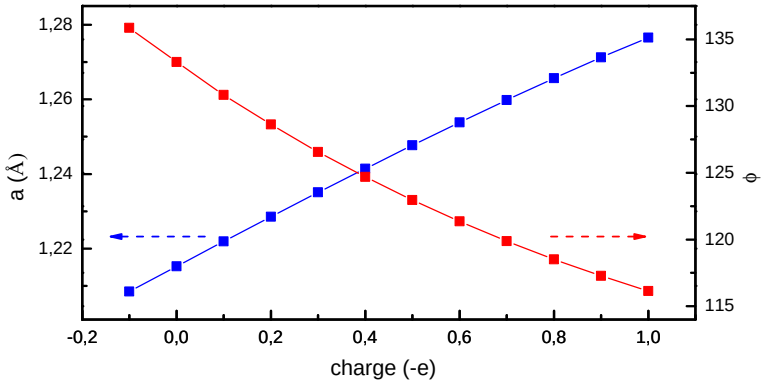

Figure 8.3. *The change of the N-O bond length, a, and the bond angle, ϕ, as a function of the additional charge on a NO_2 molecule.*

The bond length and angle of a NO_2 molecule adsorbed on a 4×4 graphene supercell become $a = 1.229\mathring{A}$ and $\phi = 128.3°$, which translates in a charge transfer of -0.205e and -0.215e, respectively. These results are more than twice the value obtained with the standard Hirshfeld method (see table 8.1), which seems to rule out this approach as a useful estimate for the charges, but the Bader charges are very close to the obtained values. However, the inaccuracy of the geometrical estimates is too large to rule out the other Hirshfeld approaches.

A more accurate physical estimate of the charge is necessary. The same reasoning that leads to the use of the bond length and angle as a measure for the charge suggests a more direct approach. If the charge transfer is related with the occupancy of the POMO in a MO picture, it would be better to use this occupancy in a more direct way. Unfortunately, the occupancies of molecular orbitals are not available since the calculations are done within the DFT formalism. However, it is possible to make use of the paramagnetism of the NO_2 molecule to deduce the occupancy of the POMO. The NO_2 molecule has a magnetic moment of $1\mu_b$ (bohr magneton) and any charge transfer ($< 1e$) reduces this magnetic moment. The graphene layer,

on the other hand, is diamagnetic. Therefore the total magnetic moment of the system (graphene+NO_2) is related to the charge transfer. A spin-polarized calculation gives a total magnetic moment of $0.818\mu_b$ for the system which corresponds to a charge transfer of -0.182e. This value is practically indistinguishable from the result of the modified Hirshfeld-I analysis (-0.181e). This gives some confidence that the modified Hirshfeld-I method is the most accurate one for our purpose and therefore this is the only method that will be used from now on.[4]

8.2 Supercell dependence

Next, it will be investigated how the charge transfer depends on the size of the supercell used in the ab initio calculations because the simulation of adsorption processes at surfaces is necessarily restricted to finite supercells. At the same time the influence of the k-point sampling of the Brillouin zone is examined.

The ab initio calculations in this section were performed within the density funcional theory (DFT) formalism using the ABINIT code within the local spin density approximation (LSD) and with Troullier-Martins pseudopotentials. A plane wave basis set is used with an energy cutoff of 30 hartree, which was tested to give converged results for all the properties studied here. Different graphene supercells ranging from 2×2 to 6×6 were implemented. For the sampling of the Brillouin zone (BZ) Monckhorts-Pack (MP) grids are used for the different supercells equivalent to a range from $12 \times 12 \times 1$ to $48 \times 48 \times 1$ points for a single unit cell.

In the previous chapter, it was demonstrated that there are at least two different charge transfer mechanisms. The charge transfer between the NO_2 and NH_3 molecules and graphene will be used here as typical examples of the two distinct mechanisms. The interaction of these molecules will be examined in increasingly large supercells, namely a $2 \times 2, 3 \times 3, 4 \times 4$, and 6×6 graphene supercell.

8.2.1 NO_2 on graphene

To investigate the influence of the charge transfer on the size of the supercell, only one configuration (i.e. adsorption site and orientation) for the adsorbed NO_2 molecule is needed. The most stable configuration that was found before was the one in which the molecule was placed on a C-C bond with the oxygen atoms closest to the graphene surface. This configuration will be used in the following calculations.

[4] Note that it is not necessary to use this method in case of paramagnetic molecules since the total magnetic moment can be used instead.

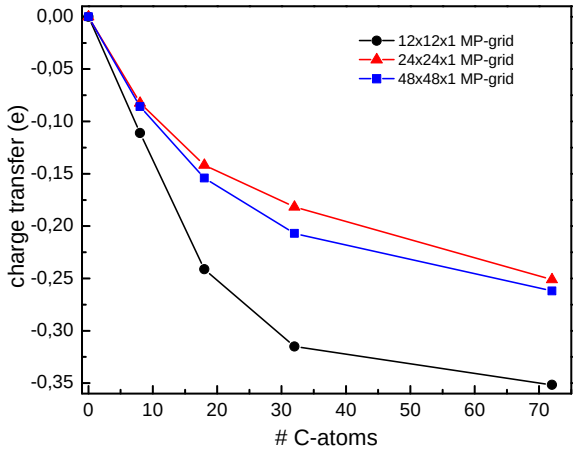

Figure 8.4. *Supercell dependence of the charge transfer between a NO_2 molecule and graphene for different MP-grids.*

In Fig. 8.4 the charge transfer, as calculated with the modified Hirshfeld-I method, is shown for different supercells and k-point grids.

Dependence on the k-point grid

The dependence of the charge transfer on the k-point grid can always be eliminated by taking finer grids. It is the computation time that is the limiting factor here. Three different k-point grids have been examined as shown in Fig. 8.4. The charge transfers seem to be converged reasonably well for a $24 \times 24 \times 1$ MP-grid. Taking into account that a $48 \times 48 \times 1$ MP-grid increases the computation time with a factor of 4, the $24 \times 24 \times 1$ MP-grid will be used from now on.

Dependence on supercell size

There is a pronounced dependence of the charge transfer on the number of atoms in the simulated graphene layer[5]. This can be explained by looking at the density of states (DOS) of the total system (see Fig. 8.5). As seen before, the lowest unoccupied orbital (LUMO) of NO_2 is below the Dirac-point of graphene, which causes the charge transfer to the molecule. But this charge transfer depends clearly on the number of electronic states between the Dirac-point and the LUMO of the NO_2 molecule, which depends linearly on the number of carbon atoms in the supercell. Therefore, it might be expected that if one takes a graphene supercell that is large enough, one would eventually get a charge transfer of one electron [42]. However, it can be seen from Fig. 8.4 that there is no simple linear dependence.

[5]The number of atoms in the simulated graphene layer is equal to twice the number of unit cells in the supercell.

The position of the LUMO in the DOS depends on the filling of this orbital: the more electrons in the orbital the more difficult it gets to put another one in it and this translates in a shift of the LUMO towards the Dirac-point. In Fig. 8.6 this shift is shown as a function of the number of carbon atoms in the supercell. It is not obvious that the orbital becomes totally filled (a transfer of one electron per paramagnetic molecule) before it coincides with the Dirac point, where the shift would stop and the charge transfer would be converged to a value of less than one electron per molecule.

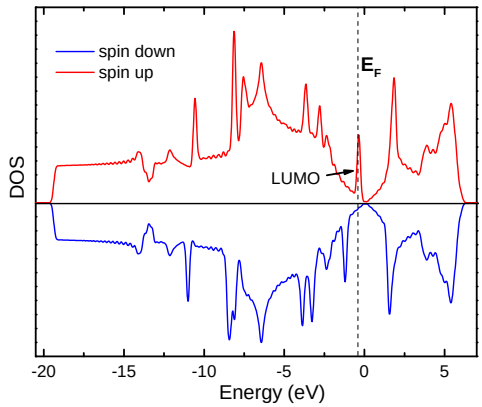

Figure 8.5. *Spin-polarized DOS for NO_2 adsorbed on graphene calculated with a $60 \times 60 \times 1$ MP-grid for a 4×4 supercell. The LUMO of the NO_2 molecule and the Fermi-energy are indicated.*

Thus it seems that one can only obtain a quantitative meaningful value of the charge transfer between a paramagnetic molecule and a graphene layer in two cases: i) when the supercell used is large enough to get a charge transfer of one electron per molecule, or ii) when the LUMO of the molecule coincides with the Dirac-point and the charge transfer has converged. In the case of the NO_2 molecule, one needs a supercell that is much larger than the 6×6 supercell that was used here due to computational limitations. However, from Fig. 8.6 it is seen that if the LUMO stays partially full, it takes more than a thousand carbon atoms to let it coincide with the Dirac-point (if the trend remains the same). On the other hand, from Fig. 8.4 one may deduce that it is not unlikely that a charge transfer of $1e$ is reached before the supercell contains 1000 carbon atoms. This leads to the conclusion that the LUMO of NO_2 will probably be completely filled before it reaches the Dirac-point. This is compatible with the experimental observation [15] that the charge transfer equals one electron charge per NO_2 molecule.

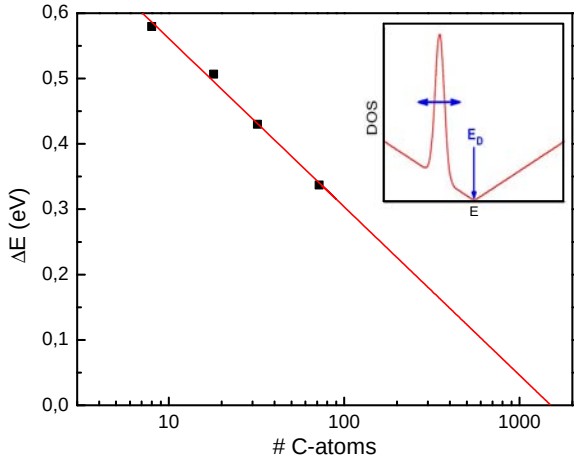

Figure 8.6. *Distance, ΔE, of the NO_2 LUMO to the Dirac-point with respect to the number of carbon atoms used in the supercell. The inset shows a close-up of the total DOS of graphene with an adsorbed NO_2 molecule around the Dirac-point.*

8.2.2 NH_3 on graphene

As for the case of NO_2, the most stable configuration of NH_3 on graphene is used to examine the dependence of the charge transfer on the supercell size. The same k-point grid as for the NO_2 case is used here.

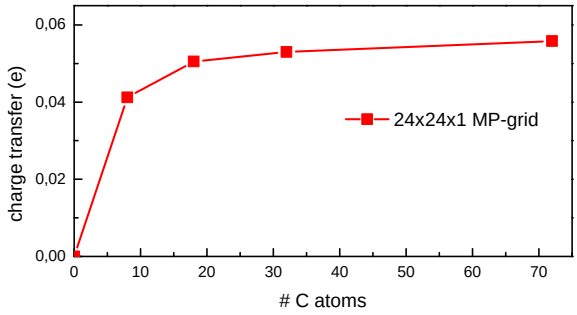

Figure 8.7. *Dependence on the size of the supercell of the charge transfer between a NH3 molecule and graphene for a 24241 MP grid.*

The charge transfer between NH_3 and graphene is caused by the hybridization of the MO's which is a local effect. Therefore it is expected that it does not depend strongly on the supercell size. This is verified by the calculations shown in Fig. 8.7. There seems to be (almost) no dependence of the charge transfer on the size of the supercell for the larger supercells. The deviation for smaller supercells is rather due to dipole interactions between the neighboring supercells. When these dipole

interactions are negligible, the charge transfer is constant. As stated before this is a consequence of the local character of the orbital hybridization that induces the charge transfer.

8.3 Summary

Different numerical approaches to calculate the charge transfer have been investigated. There appears to be a strong dependence of the charge transfer between adsorbed molecules and a graphene surface on the charge analysis method and the size of the supercell used in the simulations. For our purpose, a modified version of the iterative Hirshfeld method seems to be most physically relevant so that this will be the method of choice from now on. The influence of the size of the simulated graphene supercell depends on the particular charge transfer mechanism that dominates the adsorbate-graphene interaction. If orbital mixing (hybridization) is dominant the charge transfer will not depend on the supercell size but when there is a direct charge transfer due to empty (filled) molecular orbitals below (above) the Fermi level of graphene, the size of the supercell is important.
Taking all this into account, we can correct the results from the previous chapter and compare them with experimental findings. In case of NO_2 molecules adsorbed on graphene we could expect a charge transfer of $1e$ or less per molecule (see the discussion above). This is close to the experimental estimation of about $1e$. After the theoretical work described above, there has also been made an explicit experimental estimate for the charge transfer between NH_3 molecules and graphene. In Ref. [55] a value of 0.068 ± 0.004 e was found which is remarkably close to our corrected result of $0.056e$, shown in Fig. 8.7. Note that the corrected value is about twice the value obtained before (see table 7.2). The corrections were not made for all the molecules that were studied in the previous chapter because calculating these corrections is quite time consuming and there is no explicit experimental data available for comparison. Furthermore, the qualitative understanding of the non-corrected values remains and it is only the absolute size of the charge transfer that should not be considered correct.

Chapter 9

Water Clusters on Graphene

9.1 Introduction

As stated in the introductory chapter graphene is completely exposed to the surrounding atmosphere and the underlying substrate and is therefore susceptible to unwanted changes by environmental influences. This close contact of graphene with its environment is often a source of noise that makes different graphene samples behave quantitatively different. E.g. the mobility and density of charge carriers depend crucially on the environment.
There have been some experimental indications that water is almost always present in the environment of graphene devices. And although it has been shown that single water molecules do not bind strongly on a graphene surface (see chapter 7), the large dipole moment associated with water molecules might still be able to modify the electronic properties as e.g. its mobility. In this chapter I will investigate the interaction between graphene and water in more detail. Different systems consisting of small water clusters and ice layers on freestanding graphene sheets will be examined. The optimal orientation of these clusters with respect to the graphene sheet is investigated and various properties of the adsorbed clusters that might have an influence on the electronic properties of graphene are calculated.

9.2 Computational details

I will again make use of DFT within the generalized gradient approximation of Perdew-Burke-Ernzerhof (PBE-GGA) for the simulation of the water-graphene interaction. PBE-GGA is used because it has been shown to give the best results for H_2O hydrogen bonding [56]. Previous calculations of clustered water molecules inside and on top of carbon nanotubes [57, 58] suggest that the interaction between

water molecules and graphene-like structures is described reasonably well although the usual DFT calculations do not take explicitly into account van der Waals interactions. This is due to the polar nature of the water molecules which is responsible for the largest part of the vdW interaction in these systems and which is included in the calculations (as discussed before). Because the amount of atoms in the following simulations is rather large, I will make use of a projected augmented wave basis set which allows to take a lower cutoff energy for the plane wave basis set (20 hartree). The simulated graphene sheet consists of a 4×4 supercell with a distance of 16Å between adjacent layers. A $6 \times 6 \times 1$ Monkhorst-Pack grid is used for the sampling of the Brillouin zone. When studying ice on graphene a different supercell, $(\sqrt{3} \times \sqrt{3})$ R30°, as suggested in Ref. [59] will be used.

9.3 Results

The water systems adsorbed on graphene that are considered here consist of clusters containing up to five water molecules and a full monolayer of ice. Different possible directions of the water molecules are investigated. The energetic favorable adsorption site for a single molecule (see Fig. 9.1) was determined before and therefore there is no need to vary it here. Moreover it was also shown that the adsorption site has only a minor influence on the characteristic properties of the adsorption process. Because the binding energies between the H_2O molecules in a water cluster are more than an order of magnitude larger than the adsorption energies associated with the binding of the clusters to graphene (see below), only those water clusters will be considered that have the lowest energy and their orientation will be varied with respect to the graphene crystallographic axes.

9.3.1 Cluster geometry

Let us first take a look at the most stable geometries of freestanding planar water clusters with up to 5 molecules based on earlier investigations of freestanding water [60, 61] clusters and of water clusters on graphite [62]. In accordance with those earlier studies, it is found that (except for the water dimer and monomer) the optimized clusters consist of rings of water molecules formed in such a way that every water molecule uses one hydrogen atom to form a hydrogen bond with its neighbours. The other hydrogen atoms are pointing out of the plane formed by the ring and alternate their direction as much as possible in order to minimize the interaction between hydrogen atoms of neighboring molecules.
After obtaining the relaxed geometries, these optimized clusters are placed on a perfect graphene sheet and the system is relaxed (see Fig. 9.1). As a starting point for the relaxation two orientations with respect to the graphene surface are used for the monomer and three are used for the dimer. More orientations that

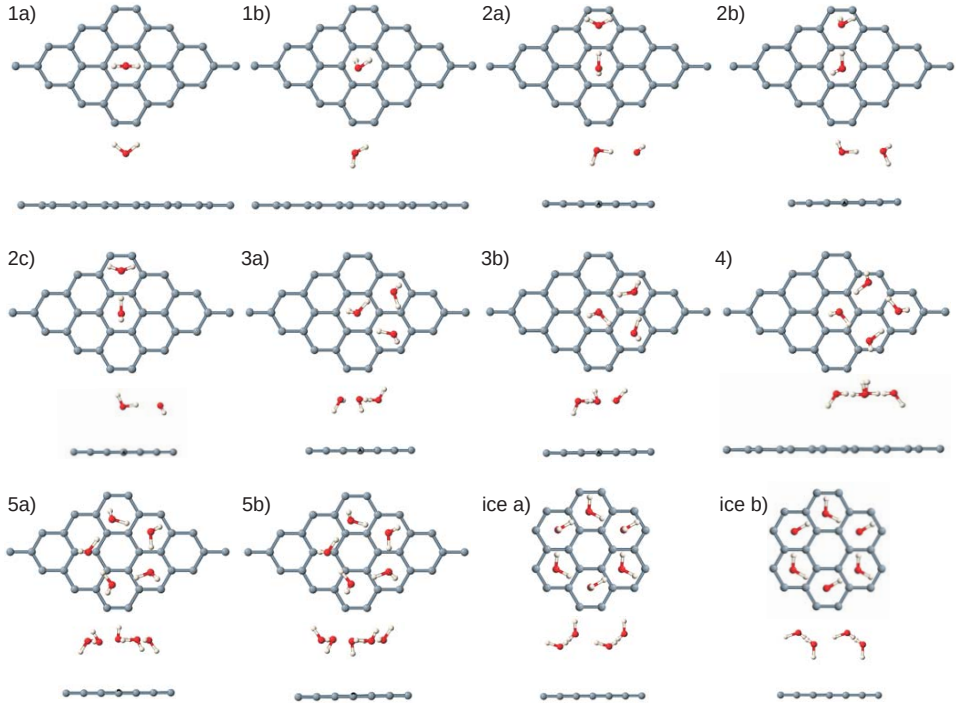

Figure 9.1. *View from the top and the side of all the different water clusters on top of graphene that were investigated in our simulations with their various orientations.*

are meaningful are possible for the monomer, but these have already been studied before (see chapter 7) and therefore it is not needed to consider them here. For the ring-shaped clusters, the starting point for relaxation is such that the ring is more or less parallel to the surface. The notations that will be used for the different clusters with their various orientations is given in Fig. 9.1.

The orientation and the shape of the clusters does not change much after relaxation but the clusters do tend to become more flat. E.g. a freestanding cluster with 5 molecules forms a pentagon that is slightly puckered, but this puckering disappears when the water pentamer adsorbs on graphene. These results are different from recent theoretical results where it was proposed that the adsorption of water clusters on graphene occurs through a 'cluster link' consisting of a single water molecule [63]. As will be shown below, bonding through a single molecule seems surprising for two reasons: i) the binding energy between molecules in a water cluster is much larger than the adsorption energy between the water cluster and graphene, which makes a deformation of the water cluster to form a cluster link unlikely and ii) the adsorption energy of a water cluster is larger than the adsorption energy of a single molecule, implying that the cluster will try to adsorb with as many molecules as possible (without changing the geometry of the cluster too much). A monolayer

of ice I_h (infinite cluster) is also studied and it is found that the lattice constant differs only 0.24 Å from a $(\sqrt{3}\times\sqrt{3})$ R30° graphene supercell, which compares well with the difference of 0.23 Å found in Ref. [59]. Therefore it is allowed to use this supercell to examine the graphene-ice interaction. It appears that the adsorption of ice on graphene has also a minor influence on the geometry in the ice layer.

9.3.2 Binding/adsorption energy

The minor changes in the shape of the water cluster after adsorption on graphene indicate that the binding energy in the cluster is much larger than the adsorption energy. To make this statement more quantitative both energies are calculated.
The adsorption energy of the water clusters on graphene is defined as $E_a = (E_{\text{cluster}} + E_{\text{graph}}) - E_{\text{tot}}$, where E_{cluster} is given by the energy of the separately relaxed cluster, E_{graph} by the energy of a perfect graphene layer, and E_{tot} by the total energy of the relaxed interacting cluster-graphene system. The energy related with the dipole interactions between water molecules of different supercells does not change much after adsorption on graphene. Consequently, this interaction energy will largely cancel in E_{tot} and can therefore be neglected.

Table 9.1. *H_2O on graphene: the total adsorption energy (E_a) per cluster and the average per molecule for clusters of different sizes and orientations.*

# H_2O mol.	Orientation	E_a(eV)	E_a(eV)/mol.
1	a	0.021	0.021
1	b	0.029	0.029
2	a	0.028	0.014
2	b	0.065	0.032
2	c	0.056	0.028
3	a	0.048	0.016
3	b	0.049	0.016
4		0.052	0.013
5	a	0.064	0.013
5	b	0.065	0.013
2 (ice)	a	0.027	0.013
2 (ice)	b	0.030	0.015

The resulting adsorption energy for the different cluster-graphene systems is given in table 9.1. Both the total adsorption energy (per cluster) and the average adsorption energy per molecule are given. The total adsorption energy becomes larger for larger water clusters, which is expected, and the adsorption energy per molecule tends to converge to a smaller value of approximately 13 meV for large clusters. Ice

is bounded a little stronger than the water clusters. However, all the adsorption energies are small, implying that water clusters are only weakly bound to perfect graphene sheets. One can also notice that clusters with more H-O bonds pointing to the graphene surface tend to bind more strongly than those with H-O bonds pointing away from the surface [50, 64]. However, for larger clusters the relative difference between the number of hydrogen bonds pointing up or down becomes small. This makes the influence of the orientation of a large cluster on the adsorption energy negligible, suggesting that both orientations are likely to occur. Notice that these energies are of the order of room temperature (26 meV), so the calculations are only applicable to real systems at low temperatures.

Table 9.2. *H_2O on graphene: the total binding energy (E_b) per cluster and the average per molecule for different size clusters.*

# H_2O mol.	E_b(eV)	E_b(eV)/mol.
2	0.24	0.12
3	0.71	0.24
4	1.28	0.32
5	1.70	0.34
2 (ice)	0.92	0.46

For the calculation of the binding energy of the H_2O molecules in a water cluster, a supercell with the same dimensions as a 4×4 graphene supercell is used. But when calculating these binding energies, the energy associated with the dipole interactions between different supercells does not cancel anymore. However, their relative importance is now much lower because the energies associated with hydrogen bonding are larger. As a consequence we can neglect this dipole interaction again. The results for the total binding energy and the average binding energy per molecule are given in Table 9.2. The binding energy increases as the clusters grow because more hydrogen bonds can be formed and the angles between the different H-bonds in larger clusters approaches those of the ideal tetrahedral bond angles in ice structures.
A comparison of Tables 9.1 and 9.2 makes clear that the binding energies are indeed an order of magnitude larger than the associated adsorption energies. This indicates that water molecules will always form clusters on a graphene sheet or, stated differently, graphene is strongly hydrophobic.

9.3.3 Charge transfer

Using the modified version of the iterative Hirshfeld charge analysis method the charge transfer between the water clusters and graphene can be calculated. The

Table 9.3. *Charge transfers: The charge transfer (CT) from graphene to the water molecules and the average CT per molecule for different size clusters and for different orientations.*

# H_2O mol.	Orientation	CT(e)	CT(e)/mol.
1	a	-0.0028	-0.0028
1	b	0.0098	0.0098
2	a	0.0026	0.0013
2	b	0.0114	0.0057
2	c	0.0073	0.0036
3	a	0.0038	0.0013
3	b	0.0114	0.0038
4		0.0058	0.0014
5	a	0.0065	0.0013
5	b	0.0094	0.0019
2 (ice)	a	-0.0016	-0.0008
2 (ice)	b	0.0064	0.0032

results are given in table 9.3. Note that the charge transfer for a single molecule is smaller than what was found earlier with the simple Hirshfeld method. The average charge transfer per molecule of a cluster decreases as the cluster gets larger and converges to a value of approximately $0.002e$ transferred form graphene to the molecules. All the charge transfers are quite small, and it is doubtful whether these will have any substantial influence on the electronic properties of graphene. The reason the interaction between perfect graphene and water is so small is probably due to the absence of any molecular orbitals of the clusters close to the Fermi level [59]. A calculation of the density of states (DOS) for the most stable orientation of the clusters on graphene shows that the molecular orbitals of the water molecules are indeed located far away from the Dirac point of graphene: for the different clusters the highest occupied molecular orbitals (HOMO) are located between 2.3 and 3.2 eV below the Dirac point and the lowest unoccupied molecular orbitals (LUMO) between 2.9 and 3.2 eV above the Dirac point (see Fig. 9.2). In conclusion, the charge transfer between intrinsic graphene and water clusters appears to be very small and will probably have no large influence on the electronic properties of graphene.

9.3.4 Electric dipole moments

Recently Wehling et al. suggested that the dipole moment of the water molecules on graphene might have a crucial influence on the energy shift of the impurity bands of an underlying (SiO_2) substrate putting them closer to the Dirac point of graphene and resulting in a doping of the graphene layer [59]. So it is interesting to

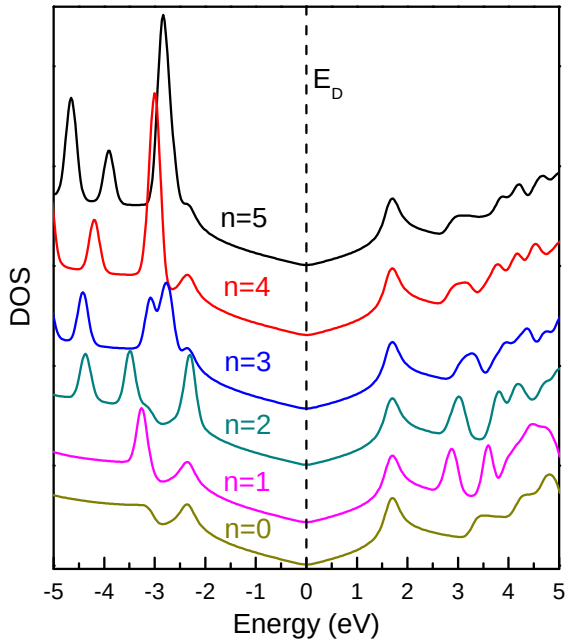

Figure 9.2. *The total density of states of the different water clusters on graphene in the most stable orientations. The number of water molecules in the cluster is denoted by n.*

know how the dipole moments of the different clusters are oriented. Therefore the total strength of the dipoles is calculated and also their projections perpendicular and parallel to the graphene surface are determined. The results for the different clusters are given in Table 9.4.

The dipole moments of neighboring molecules in the same cluster are directed as much as possible in opposite directions. As a consequence, the average dipole moment per molecule in large clusters will become vanishingly small (see Table 9.4). Only in the case that the concentration of water molecules becomes large enough for ice layers to be formed, an appreciable dipole moment will appear. The reason for this is clear: because water molecules in ice-like structures have more than two neighboring molecules with which they form hydrogen bonds, they have less freedom in their orientation and are not able to point their dipole moments in opposite directions. As a result, the dipole moments of the different molecules accumulate and form a dipole layer on graphene. Such dipole moments, which have an influence on the electronic properties of graphene [59], have been observed experimentally [65]. But for lower concentration there will be no direct influence of the electric dipole moment of relatively small water clusters on graphene. However, because of the large dielectric constant of water (the dielectric constant of liquid water is ϵ_w=80) the water clusters can indirectly influence the electronic properties

Table 9.4. *Dipole moments: the total dipole moment (P) as well as the dipole moment parallel ($P_{\parallel}$) and perpendicular ($P_{\perp}$) to the graphene sheet for water clusters with different sizes and orientations ($P_{\perp}$ is positive when pointing away from the sheet and negative when pointing to the sheet). The average dipole perpendicular to graphene per cluster is also shown. All dipoles are given in Debye (D) units.*

# H_2O mol.	Orient.	P	$P_{\parallel}$	$P_{\perp}$	$P_{\perp}$/mol.
1	a	1.80	0.00	1.80	1.80
1	b	1.82	1.36	-0.66	-0.66
2	a	2.94	2.94	-0.11	-0.05
2	b	2.87	2.87	0.10	0.05
2	c	2.66	2.66	-0.09	-0.05
3	a	1.24	0.03	-1.24	-0.41
3	b	1.15	0.04	1.15	0.38
4		0.03	0.03	-0.02	-0.01
5	a	1.08	0.18	-1.06	-0.21
5	b	1.00	0.24	0.97	0.19
2 (ice)	a	/	/	1.62	0.81
2 (ice)	b	/	/	-1.63	-0.81

of graphene through e.g. the screening of the charge-charge interaction and the screening of the Coulomb interaction of ionized impurities that are situated in graphene and/or in the substrate that supports the graphene layer [15, 30].

9.4 Conclusions

In this chapter the influence of water clusters on the electronic properties of a perfect graphene sheet was studied using ab initio DFT calculations. The binding energy of the water molecules in a cluster appears to be an order of magnitude larger than the adsorption energy between the cluster and graphene indicating that graphene is strongly hydrophobic. Charge transfers between a graphene sheet and water clusters, which could influence the density of the charge carriers and consequently the resistance in graphene, are very small. The molecules in a water cluster tend to orient their dipole moments in opposite directions, so that they cancel on average. But in the limit of a large concentration of water molecules such that ice-like structures can be formed the dipole moments of the different molecules accumulate instead of averaging out leading to an appreciable total dipole moment that might have an influence on the electronic properties of graphene [59].

Chapter 10

Alternative Charge Transfer Mechanisms

In chapters 7 and 8, two different charge transfer mechanisms have been investigated which are present when molecules attach to perfect freestanding graphene layers. When less ideal graphene samples are considered other charge transfer mechanisms can be present too. In this chapter, I will describe these alternative mechanisms and discuss the circumstances in which they might occur.

10.1 Influence of dipole layers

In the previous chapter, it was shown that there is only a small charge transfer between clusters of water molecules and perfect graphene (due to orbital hybridization). In experiments, however, one finds that the presence of water induces appreciable hole doping of the graphene samples [1, 15]. To explain these observations, Wehling *et al.* suggested a charge transfer mechanism which is based on a doping effect that is caused by the strong electric dipole of the water molecules [59], as was briefly mentioned in the previous chapter. I will shortly describe the calculations they performed and comment on their validity.

10.1.1 Water on graphene: the role of the substrate

The first systems that were investigated by Wehling *et al.* consist of a freestanding graphene layer covered with high concentrations of water molecules that are described by some model structures such as ice layers (as treated in the previous chapter) or unrelaxed water molecules in a fixed position (see Fig.10.1).
These water molecules form a dipole layer which appears to shift the nearly free

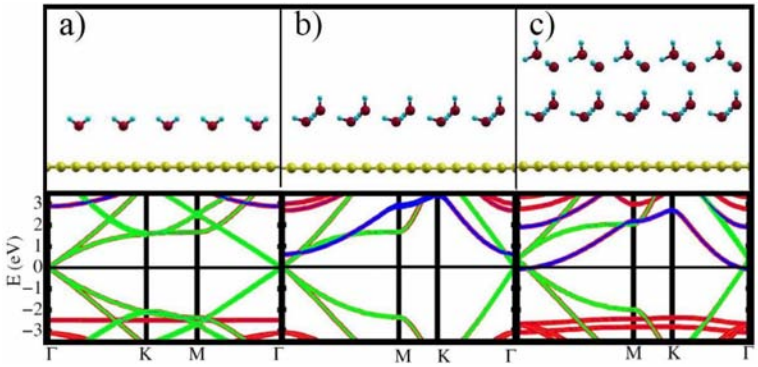

Figure 10.1. *Shifting of the quasi-free electron band by ice layers. The upper pictures show the different investigated systems and the lower figures show the corresponding electronic band structure. The quasi-free electron band is indicated in blue and the bands from the ice layers in red. (Merged figure from Ref. [59])*

electron bands in the graphene spectrum (see Fig. 10.1). When the dipole layer is strong enough, i.e. when enough uniformly oriented water layers are present, the free energy band can be shifted below the Fermi-level of graphene and cause doping. The problem with this explanation, as indicated by Wehling *et al.* [59], is that the dipole layer has to be much stronger than what is observed experimentally [65]. Therefore they suggested an alternative explanation, based on the same principle, in which a model for the SiO_2 substrate is explicitly included in the simulations (see Fig. 10.2). Since SiO_2 is amorphous it can not be incorporated in a direct way. Therefore they used a crystalline model with defects into it to represent this substrate.
The impurity bands resulting from the defects do not cross the Fermi-level, but when water molecules are placed on top of graphene or between the graphene layer and the defected substrate these bands can be shifted across the Fermi-level. In this way they can induce hole or electron doping (depending on the orientation of the water molecules) at much lower concentrations than were needed to induce doping in freestanding graphene.

10.1.2 Influence of dipole layers on graphene

Stimulated by the theoretical research described above I investigated the influence of a dipole layer on graphene. For this, a model water layer is used that consists of a single H_2O molecule in a 2×2 graphene supercell which is directed perpendicular to the graphene surface (see inset of Fig. 10.3(b)). This is not a realistic model, but I only want to examine the qualitative consequences of a molecular dipole layer on the potential at both sides of the graphene layer. The work function, which is defined as the potential difference between vacuum and the Fermi-level, is

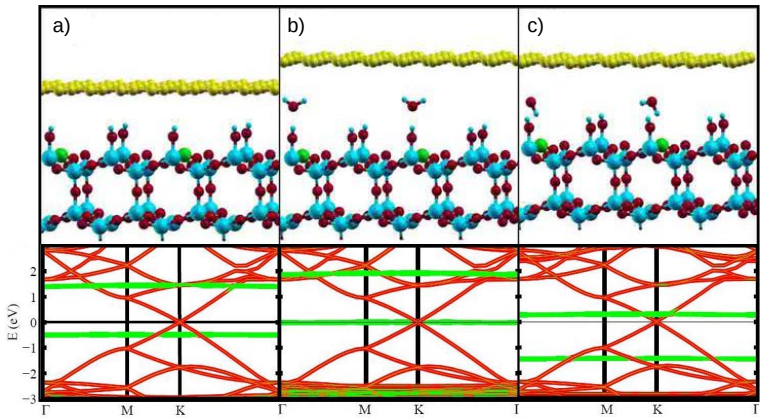

Figure 10.2. *Shifting of the defect band by water layers. The upper pictures show the different investigated systems and the lower figures show the corresponding electronic band structure. The impurity bands are indicated in green and the bands from the water layers in red. (Merged figure from Ref. [59])*

a useful property to do this. However, there is a problem with calculating the work function of a system with non-vanishing electric dipole moment that is simulated with periodic boundary conditions. An infinite dipole layer divides space into two regions with different potential, but when periodic boundary conditions are applied the potentials need to be matched so that artificial electric fields are created (as demonstrated in Fig. 10.3(a)). It is easy to correct the potential by subtracting the electric field.

Two orientations of the water molecule with respect to the graphene layer are considered: one with the H atoms pointing to the surface (d) and the other with the H atoms pointing away from the surface (u). These two orientations correspond to oppositely directed dipole layers. The influence of these dipole layers on the work function is summarized in table 10.1. The work function for both sides of the graphene layer is given together with the difference from the work function of intrinsic graphene which is found to be $\mathrm{WF}_{\mathrm{graph}} = 4.47\mathrm{eV}$ (LDA).

Table 10.1. *Water dipole layer on graphene: the work function (in eV) for the graphene side, WF_g, and the water side, WF_w, and the total dipole moment of the system (in debeye) are given. The difference of the work function relative to intrinsic graphene is shown between brackets.*

orientation	$\mathrm{WF_g}$		$\mathrm{WF_w}$		P
u	4.56	(+0.09)	1.55	(-2.92)	-1.73
d	4.42	(-0.05)	7.55	(+3.08)	1.67

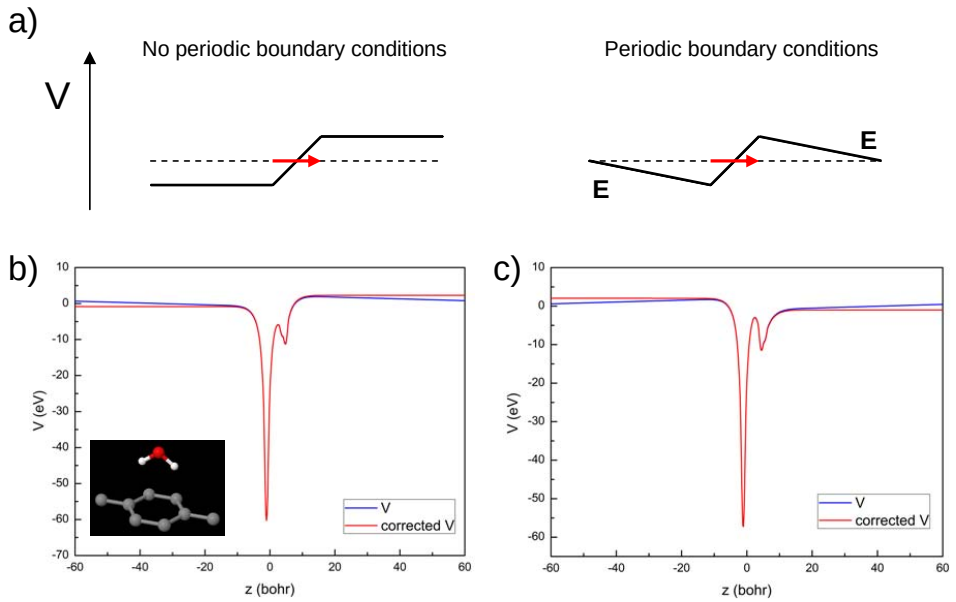

Figure 10.3. *a) The creation of an artificial electric field,* **E***, when applying periodic boundary conditions to a dipole layer. The dipole layer is indicated by a red arrow. b) Calculated and corrected potential for the H_2O molecule with orientation d (see inset). c) Calculated and corrected potential for the H_2O molecule with orientation u.*

The work function on the water side of the water-graphene system, WF_w, is altered by about 3 eV in positive or negative direction according to the orientation of the water molecule. On the other hand, the work function on the graphene side, WF_g, remains practically unchanged by the presence of the water layer. So it appears that the influence of the water layer on the graphene side is almost perfectly screened by the graphene layer. So in conclusion, the (main) influence of a dipole layer on graphene is to change the potential on the side of the dipole layer.

Discussion

We can now apply these results to reconsider the theoretical results obtained in Ref. [59]. The first system that was studied in this paper, i.e. water layers on intrinsic graphene (without a substrate), is similar to our model system. The shift of the quasi-free electron bands in this case is readily explained by the shift in potential due to the water dipole layer as can be understood from the discussion of the graphene band structure in section 6.1.1.

The second observation of Wehling *et al.* was that the impurity bands from defects in the substrate can be shifted across the Fermi-level by placing water molecules on graphene or between graphene and the substrate. Although this conclusion is

valid for water molecules between the graphene layer and the substrate, it can not be true for water molecules on the graphene surface. The influence of the last molecules is negligible because the graphene layer shields their interaction. If DFT simulations find any influence of the dipole layer, this should be ascribed to the periodic boundary conditions that were used which causes the substrate to interact directly with the periodic image of the water molecules.
Therefore the suggested charge transfer mechanism can only account for the doping of graphene samples when the water is already present on the substrate before the graphene layer is deposited onto it (which is probably the case [1]). Atmospheric doping, as observed in Ref. [15], can not be explained by this mechanism, however.

10.2 Electrochemical surface transfer doping

In 1989 Landstrass and Ravi discovered a strange phenomenon when they performed conductance experiments on hydrogenated diamond samples [66]. Although diamond is known to have a large electronic band gap their samples showed a surprisingly high conductivity. A variety of explanations have been proposed, such as doping by atmospheric molecules, but it took a long time before the now (more or less) generally accepted explanation was found [67]. The proposed doping mechanism might, under certain circumstances, be relevant for the doping of graphene samples as well.

Hydrogenated diamond

The accepted doping mechanism for diamond consists of a charge transfer between a hydrogenated diamond surface on one side and an aqueous redox couple on the other side. This mechanism is only possible when there is an aqueous phase present near the diamond surface and if the redox couple has the right electrochemical potential. A hydrogenated diamond surface is hydrophobic but the charge transfer enhances the mutual attraction so that the hydrophobicity is reduced. The following reducing half reactions appear to underly the doping mechanism for diamond,

$$\mathrm{O_2}(g) + 4\mathrm{H^+}(aq) + 4e^- \longrightarrow 2\mathrm{H_2O}(l) \tag{10.1}$$

$$\mathrm{O_2}(g) + 2\mathrm{H_2O}(l) + 4e^- \longrightarrow 4\mathrm{OH^-}(aq). \tag{10.2}$$

It depends on the acidity of the aqueous solution which one is dominant. The electrochemical potentials for these reactions under ambient conditions are -5.66 eV and -4.83 eV, respectively. In other words, energies from 4.83 to 5.66 eV (depending on the acidity of the solution) are gained when an electron is brought from vacuum into the system to trigger these reactions. When the electron is not coming from vacuum but from hydrogenated diamond, one should subtract the energy that is

needed to remove the electron from the hydrogenated diamond into the vacuum. So there will be a spontaneous electron transfer from the hydrogenated diamond to the aqueous solution if the valence band maximum of diamond (-5.2 eV) is higher in energy than the electrochemical potentials for the half reactions. For (10.1) this is indeed the case so that it can cause hole doping in hydrogenated diamond (see Fig. 10.4).

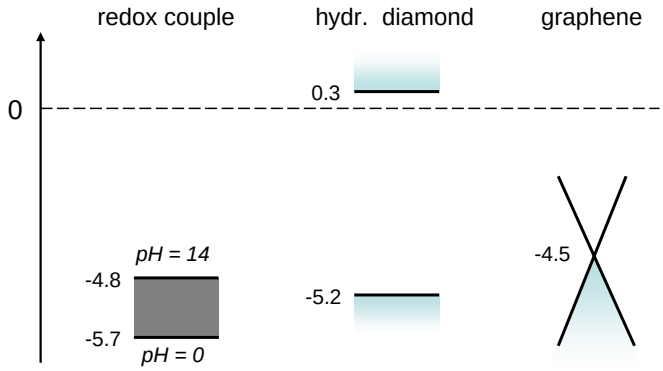

Figure 10.4. *The energy of the redox couple (for different pH) in comparison with the valence and conduction band of hydrogenated diamond and graphene. The energies are in eV.*

graphene

In the case of graphene, the electrochemical potential should be compared to the work function of graphene which is about 4.5 eV so that the same mechanism as for diamond might induce hole doping in graphene (as can be seen in Fig. 10.4). Note that for this doping mechanism to be present, an aqueous phase is needed near the graphene layer and furthermore O_2 gas molecules should be available from the atmosphere. The same mechanism can also be relevant for the doping of some semiconducting graphene derivatives such as graphane, i.e. fully hydrogenated graphene (see later).
One can also imagine other redox couples than in (10.1) to induce doping under certain circumstances, but this needs further investigation.

Chapter 11

Changing the work function of graphene

In the previous chapter, it was shown that the work function of graphene plays an important role in the the doping level of graphene. In this chapter I investigate how this work function can be changed so that more control over the concentration of charge carriers in graphene might be achieved.

11.1 Work function of few layer graphene

The work function (WF) of a single graphene layer is first examined with LDA and GGA to find out which one gives the best result when compared to experiment. When a vacuum layer of 100 bohr is used to converge the potential away from the graphene layer, the work function is calculated to be 4.48 eV and 4.22 eV for LDA and GGA, respectively. The absolute WF found experimentally is ≈4.6 eV for graphite [68] and similar results are found for FLG [69]. Since the WF of single layer graphene is only slightly smaller than FLG (see below), LDA appears to give results that resemble more accurately the experimental values. Therefore I use the local density approximation for the exchange correlation functional in the following.

As a first possible way to alter the work function of graphene I will consider the variation of the work function with the number of graphene layers. To this end, AB-stacked few layer graphene (FLG) samples with 1-7 layers are examined. The relaxation of FLG as compared to graphite is very small, but both the relaxed and unrelaxed cases are investigated. The results for the work function of the unrelaxed and relaxed FLG are plotted in Fig. 11.1. The relaxation seems to have only a minor effect on the work function of FLG, but the figure shows that there

is a small increase of the work function of approximately 0.03 eV when going from single to bilayer graphene. Adding more layers to the system does not induce any further substantial changes to the work function. So when the work function of pure graphene samples is considered, there is only a difference between monolayer graphene and FLG with 2 or more layers. This finding is in contrast with an earlier theoretical investigation [70] in which large variations of the work function were found when the number of layers changes. The behavior of the work function in our case can be explained by the fact that the work function is a surface related property: the charge density of the outer layer is slightly changed by the presence of an underlying layer, but is (almost) unaffected by layers that are lying farther away.

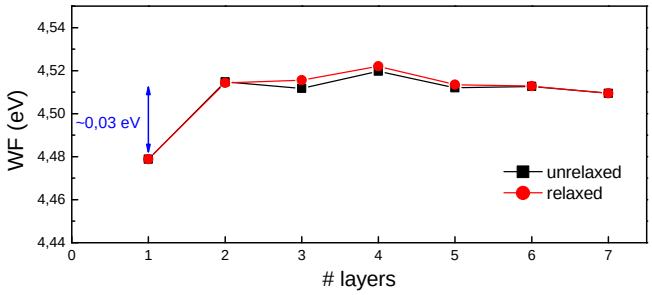

Figure 11.1. *The variation of the work function with the number of layers in unrelaxed and relaxed FLG.*

11.2 Work function of strained graphene

In-plane strain

A more effective way to change the work function of graphene is by the introduction of strain in the sample. In this section the change of the work function is investigated when the graphene sample is stretched or quenched along the zigzag and armchair directions and also the variation of the work function when a uniform strain is applied over the sample is considered. The results for strains from -10% to 30% are shown in Fig. 11.2. The results found here are consistent with previous theoretical calculations performered by S.-M. Choi *et al.* for strains smaller than $\pm 20\%$ [71].

The work function of graphene becomes larger for positive strain and smaller for negative strain. The influence of the strain appears to be independent of the direction, zigzag or armchair, for strains smaller than about 15%. In Fig. 11.3 the relative change of the workfunction due to the strain is plotted for the uniform

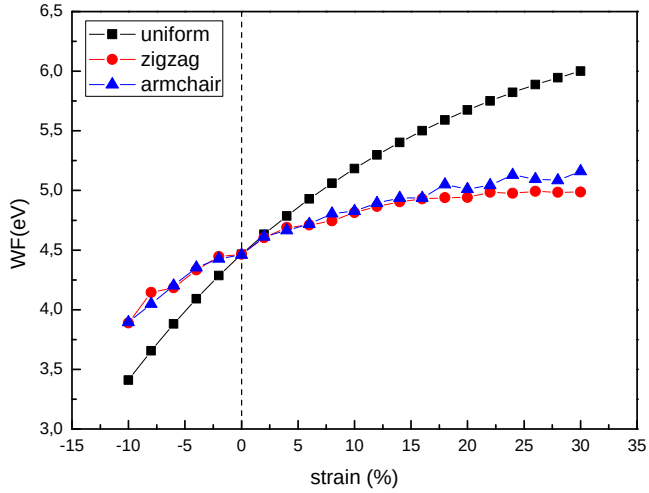

Figure 11.2. *The work function of monolayer graphene as a function of the strain.*

strain and the sum of the work function changes for the strain in the zigzag and armchair directions.

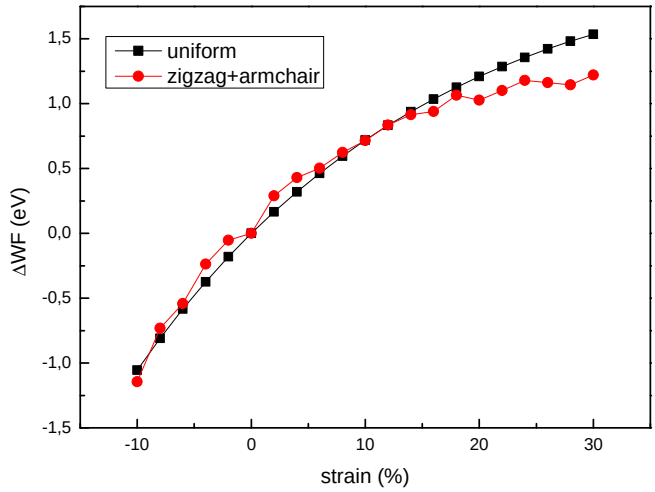

Figure 11.3. *The relative variation of the work function for uniformly strained graphene and the sum of the work function changes for the strain in the zigzag and armchair directions.*

It can be seen that the work function of uniformly strained graphene is the same as the sum of the work functions of the uniaxial strained samples for small strains (<15%). The small variations are due to computational inaccuracies that are caused by the nonuniformity of the k-point grid. Work function changes of the

order of 1 eV can be achieved for graphene in this way.
The variation of the work function as a function of strain can be understood from the simple tight-binding model for graphene that was introduced in chapter 4. The work function of graphene is determined by the Fermi-level of graphene which coincides with the Dirac point in undoped graphene. The qualitative features of the tight-binding band structure remain unaltered when strain is applied to the graphene sample. Therefore it is clear that the position of the Fermi-level is determined by $H_{\mathrm{AA},\mathbf{k}}$ in (4.48), which was chosen to be zero before because only the relative energies were of interest there. Let us now keep this term and also include second neighbor interaction. In this case, the energy corresponding to the Dirac-point (i.e. the energy at the K-point) determines the work function of graphene. As can be seen from the MO at this point (see Fig. 4.7), this energy results from a (second-neighbor) anti-bonding orbital. Introducing positive strain, i.e. decreasing the overlap, results in lower energies (at the K-point) and therefore increases the work function. The opposite is true for negative strain.

Interlayer strain in AB-stacked bilayer graphene

We can also consider the strain in the direction perpendicular to the graphene layers in e.g. a bilayer of graphene. Although the interlayer interaction is not well described with regular DFT, the qualitative changes are expected to be similar. The result of strain in the z-direction in AB-stacked bilayer graphene is shown in Fig.11.4.

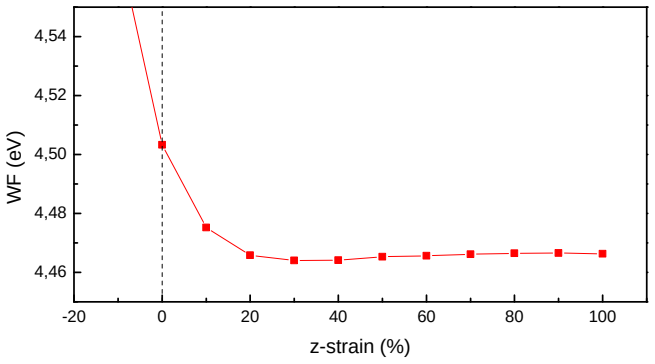

Figure 11.4. *The variation of the work function for a strained AB-stacked bilayer of graphene.*

The work function increases rapidly when the two layers are brought closer together and converges slowly to the work function of monolayer graphene when the distance between the layers is increased.

11.3 Adsorbates on few layer graphene

In the previous chapter, a model system consisting of water molecules on graphene was studied to examine the influence of molecular dipoles on the work function of graphene. It was demonstrated that the work function of graphene was only changed at the side of the adsorbed water layer and that the other side was nearly unaffected. It can be expected that the situation is different when the adsorbed layer induces strong doping in the graphene layer. As has been experimentally demonstrated (see Fig. 11.5), the work function of graphene (and bilayer graphene) on a SiO_2 substrate can be continuously tuned by doping the graphene sample by applying a gate voltage over the system (FET device). The change in the work function in this case is simply a consequence of the shift of the Fermi-level away from the Dirac-point. A similar variation of the work function can be achieved by doping through adsorbates on the surface or a different substrate such as SiC.

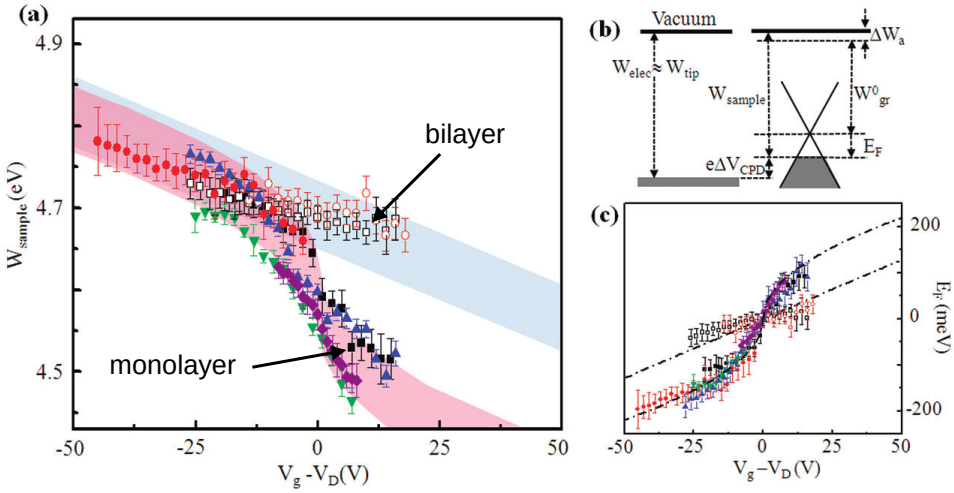

Figure 11.5. *The variation of the work function of single and bilayer graphene as a function of the gate voltage. a) the measured variation of the work function. b) Schematic picture that explains the cause of the work function changes. c) The Fermi energy variation corresponding to the work function change as a function of the gate voltage. The dashed lines are the theoretical predictions of a simple tight-binding band structure calculation. (Taken from Ref. [72].)*

It is an interesting question how the work function changes when few layer graphene is used instead of monolayer graphene. The charge is not expected to be uniformly distributed over the different layers so that deviations from the simple monolayer system are possible. To investigate this another model system will be used consisting of FLG with an adsorbed sodium layer. Na is an alkali metal and is therefore

expected to donate an appreciable amount of electrons to graphene. In the following the charge per layer and the work function per side are studied when the number of graphene layers is increased from 1 to 5. The charges per layer of the different FLG samples are summarized in Fig. 11.6. These charges were again calculated with the modified iterative Hirshfeld method.

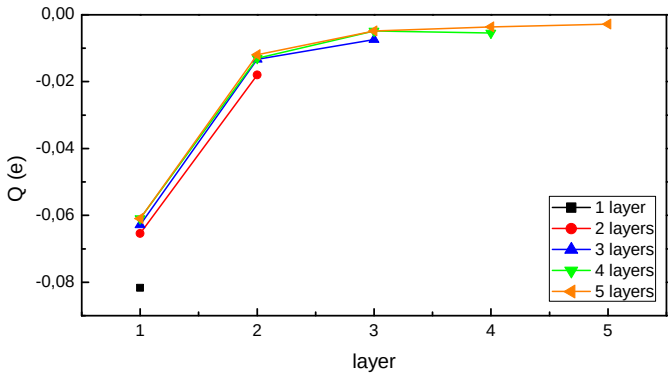

Figure 11.6. *The charge per layer for Na adsorbed on FLG with 1 to 5 layers. The layers are numbered from 1 to 5 starting from the one closest to the adsorbed Na layer.*

The total charge that is transfered from the sodium layer to FLG remains nearly constant, but it can be seen that there is a charge redistribution when more graphene layers are added to the system. The charge per layer decreases exponentially for layers farther away from the adsorbed Na layer. The work function for both sides of the Na-FLG system is given in Fig. 11.7.

The work function at the Na side is almost constant and its size is similar to the one of a freestanding Na layer. A large variation of the work function (>1eV) can be seen at the graphene side when the number of layers is increased from 1 to 5, which is an order of magnitude higher than the changes due to the number of layers. For a single layer the WF is much smaller than the WF of graphene and for 5 layers the WF is a little bit larger. This variation of the WF is partly caused by the charge that is present on the outermost layer: the work function becomes smaller when negative charges are present. Because of the nonuniform charge distribution within the FLG, there is also a dipole layer present at the graphene side which plays also a part in the variation of the work function. The WF as depicted in Fig. 11.7 is the result of the combination of this dipole layer and the shift of the Fermi-level due to the increased orbital occupation in the last layer corresponding to the charge transfer.

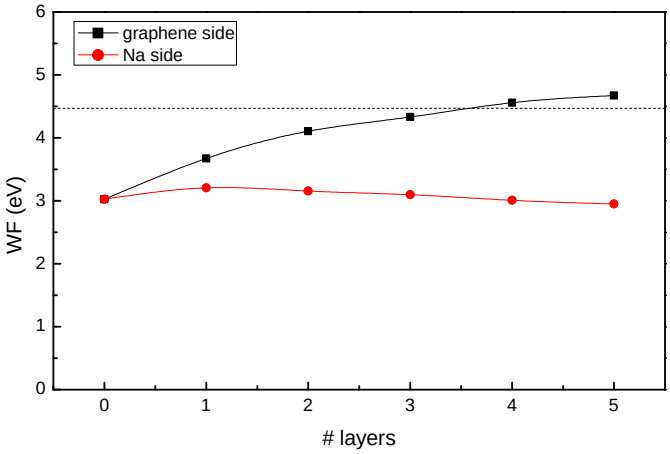

Figure 11.7. *The work function for both sides of the systems consisting of Na adsorbed on FLG with 1 to 5 layers. The dotted line corresponds to the work function of graphene without adsorbates.*

Discussion

It is possible to generalize the findings found above for Na-FLG to some related systems such as FLG on a silicon carbide substrate. As was mentioned in the introductory chapter on graphene (Chapter 2), graphene samples that are synthesized by thermal decomposition of a SiC surface are strongly negatively or slightly positively doped (depending on the side of the SiC crystal where the graphene layers are grown). In case of FLG on SiC a similar exponentially decreasing charge distribution can be expected as for the Na-FLG system discussed above. Therefore the work function is determined by the number of graphene layers that are grown on SiC even if the intrinsic differences of the various FLG's as shown in Fig. 11.1 (<0.03eV), are ignored. In case of FLG grown on the Si side (0001) we can expect large variations with a low WF for monolayer graphene and an increasing WF when more layers are added. At the C side ($000\overline{1}$) small variations are expected with a decreasing value for the WF when the number of layers increases. This is indeed what has been observed experimentally for FLG on the Si side of SiC [73] as shown in Fig. 11.8.

11.4 Conclusions

Several ways have been investigated to tune the work function of graphene. It was demonstrated that only small differences in the WF were obtained by variation of the number of layers in FLG and larger changes can be achieved by applying strain to the graphene samples. The most effective way appears to be through doping:

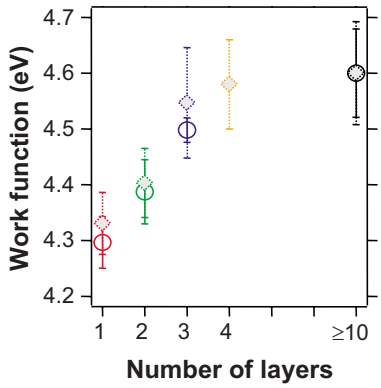

Figure 11.8. *The work function of FLG grown on the (0001) side of SiC as a function of the number of layers (different points represent different samples). Taken from Ref.[73]*

depending on the level of doping and the number of graphene layers present in the sample, the WF can be varied over a large range (≈2eV).
The possibility to change the size of the work function can be useful for some applications where it e.g. needed to reduce the contact resistance between the graphene samples and electrical leads in graphene top electrode devices [72].

Chapter 12

Chemisorption on Graphene

In search for new materials for future electronics, graphene [1] has often been suggested as a suitable candidate because of its exceptional properties such as its essentially two-dimensional form and high crystal quality, electron mobility, and robustness [3, 74, 75]. Some major obstacles which have to be dealt with before graphene can make its promises come true are the absence of a band gap in the electronic spectrum of intrinsic graphene and the Klein paradox as a consequence of the Dirac-like nature of the charge carriers. These obstacles can be overcome through chemical modification of the graphene surface.

Until now, only the interaction between molecules and graphene has been investigated but in this chapter also the interaction with radicals, will be considered. These radicals induce structural changes when adsorbed on graphene in contrast to the physisorbed molecules which did not disturb the graphene lattice.

The most studied way to chemically modify a graphene surface is undoubtly hydrogenation. This is probably due to the simplicity of these systems and additionally the possible application of graphene systems for hydrogen storage [76]. This last application has resulted in a lot of research on the interaction of molecular and atomic hydrogen with graphitic materials. In this research it was found that molecular hydrogen leads to physisorption whereas atomic hydrogen can form chemical bonds with the carbon atoms (as seen before). In case of only a few layers of graphene, it was found that hydrogenating a single layer of graphene is easier than hydrogenating a bilayer [77, 78].

I focus the investigation on two atomic radicals, namely hydrogen and fluorine, which are able to form strong bonds with carbon atoms. These two atomic species have very different electron affinities and this has a great influence on their adsorption behavior. Hydrogen has an electronegativity of 2.2 which is comparable to that of carbon (2.5), but fluorine has a much larger electronegativity of 4.0.

12.1 Preliminary molecular studies

It is useful to investigate the chemical bonds between carbon and the atomic adsorbates in simple molecular systems for comparison with the results of the more complicated interactions between a graphene layer and these radicals. Therefore I briefly examine the molecules CH_4, CH_3F, CH_2F_2, CF_3H, and CF_4. It appears that a large cutoff energy for the plane wave basis (40 Hartree) is required to get an accurate description for fluorine atoms. This is caused by the very compact nature of the valence wavefunctions for this atom. The GGA approximation is used for the exchange-correlation functional to get a good description of the bond lengths and angles. The results for the different molecules are given in table 12.1. The results are in excellent agreement with experimental data [79]. The C-H bond distance has more or less the same length in the different molecules ($1.090 - 1.095$Å) but the C-F bond is variable ($1.334 - 1.397$Å). This indicates that the bond is not purely covalent but that there is also a strong ionic component present. The difference in electronegativity between C and F induces a charge transfer from C to F. When more fluorine atoms are present in the tetragonal CH_xF_{4-x} molecule, the charge on the carbon atom is larger and, consequently, the C-F bonds are shorter. The C-F bond appears also to be stronger than the C-H bond and each type of bond seems to have an almost constant contribution to the total formation energy.

Table 12.1. *The bond distances, d, bond angles, θ, and the formation energy, E_f, per atom with respect to graphene and the H_2 and F_2 molecules.*

	CH_4	CH_3F	CH_2F_2	CF_3H	CF_4
d_{CH}	1.090	1.093	1.095	1.095	-
d_{CF}	-	1.397	1.369	1.348	1.334
θ_{HCH}	109.5	110.1	113.6	-	-
θ_{FCF}	-	-	108.5	108.5	109.5
θ_{HCF}	-	108.8	108.7	110.5	-
E_f	-2.60	-2.73	-2.99	-3.32	-3.61

12.2 Adsorption of H and F on graphene

In this section, the adsorption of hydrogen and fluorine atoms on graphene at low concentrations is shortly investigated.

12.2.1 Adsorption of single atoms

The adsorption of the radicals H and F on graphene is completely different from the molecular adsorption that was examined in the previous chapters. We have seen that the investigated molecules do not perturb the graphene crystal structure when they are physisorbed and that the binding energy of the molecules is more or less independent of the adsorption site. The situation is completely different for chemisorption on graphene. In this case the adsorbates form strong bonds with the carbon atoms and distort the graphene layer by pulling out C atoms. The adsorption site of the radicals depends roughly on the number of 'missing' electrons. E.g. H and F are short of one 1 e and bind to a single C, but oxygen needs two more electrons and therefore it forms a bond with two C atoms by adsorption on the bridge site. In other words, each C atom in graphene is able to provide one electron to form an extra chemical bond.

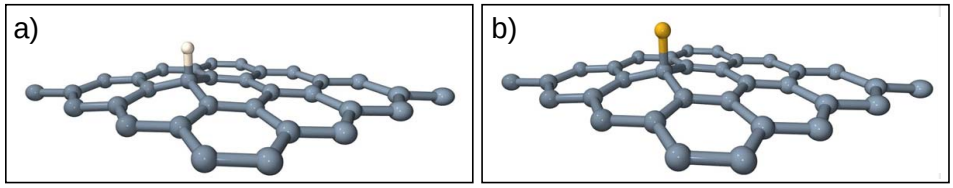

Figure 12.1. *Chemisorption on graphene: adsorption of single H atom (a) and F atom (b) on a 4×4 graphene supercell.*

For the study of the adsorption of H and F on graphene a 4×4 graphene supercell is used and the PBE-GGA exchange-correlation functional is applied to get a good description of the bond lengths. The simulations are spin-polarized since the adsorbates contain unpaired electrons. The fully relaxed structures are shown in Fig. 12.1 and some calculated properties are given in table 12.2. As expected the C-F bond is stronger than the C-H bond.

Table 12.2. *The bond distances, d, bond angles, θ, the binding energy, E_b, and the total magnetic moment, M, of the system are calculated. The different properties are given in Å, degrees, eV and μ_b, respectively.*

	d_{CX}	d_{CC}	θ_{CCX}	θ_{CCC}	E_b	M
H	1.122	1.495	103.4	114.8	-0.835	1.0
F	1.557	1.475	102.6	115.4	-1.594	0.0

Let us now concentrate on the bond lengths between the adsorbates and the carbon atom that takes part in the chemical bond formation. The C-H bond length for H

on graphene, $d_{CH} = 1.12$Å, is typical for C-H bonds as can be seen by comparison with table 12.1. The C-F bond length, on the other hand, has a relatively large value, $d_{CF} = 1.56$Å, when compared to common C-F bonds as in table 12.1. There is a difference of about 0.2 Å which indicates that the Coulomb attraction between the C and F atom, caused by the interatomic charge transfer (see previous section), is diminished. A possible explanation for this might be that the charge on the C atom is spread out over the graphene layer. This can be confirmed by a (simple) Hirshfeld charge analysis that shows that only one third of the charge remains on the bonded C atom.
The length of the C-C bonds closest to the adsorbates are intermediate between sp^2-bonds in graphene, $d_{\text{graph}} = 1.42$Å, and sp^3-bonds in diamond, $d_{\text{diam}} = 1.55$Å. This might be expected from a bond between an sp^2-hybridized and sp^3-hybridized C atom (e.g. the C-C bond in a C_2H_5 molecule is 1.48Å), which indicates that the C atom below the adsorbate is sp^3-hybridized. The bond angles, on the other hand, suggest a hybridization state intermediate between sp^2 and sp^3.
From table 12.2 it is clear that there is a pronounced difference in the magnetic moment of the H-graphene and F-graphene system: H on graphene has a magnetic moment of $1\mu_b$ whereas F on graphene has M=$0\mu_b$. This can be explained by the different electronegativity of H and F. In the isolated state H and F have both M=$1\mu_b$ because their partially filled atomic orbital splits in two spin orbitals that are close in energy, so that one is completely filled and the other is empty. When H adsorbs on graphene one of these spin orbitals will be below the Fermi-level of graphene and the other above (because the electronegativity between H and C is similar), so that the magnetic state remains. When F adsorbs on graphene, both spin orbitals are below the Fermi-level of graphene (because F has much higher electronegativity than C) and the magnetic state disappears.

12.2.2 Pairs of hydrogen atoms adsorbed on graphene

It is interesting to know at which site a second adsorbate will chemisorb if there is already a chemisorbed atom present. This has already been investigated in detail for hydrogen atoms by Boukhvalov *et al.* [80] so I will restrict the discussion to a short review of their results. There appear to be several important aspects for the adsorption of a second H atom: a) the side of the graphene layer, b) the sublattice, and c) the distance to the first adsorbate. These 3 features determine the binding energy and the magnetic moment of the system. Fig. 12.2 shows the total binding energy per H atom as a function of the hydrogen interatomic distance. The four curves represent the adsorption on different sides and sublattices.
It can be seen that the adsorption at small distances is favorable. Furthermore, the adsorption on different sublattices and different sides of the graphene layer is favored, but the sublattice is more important than the adsorption side. This last

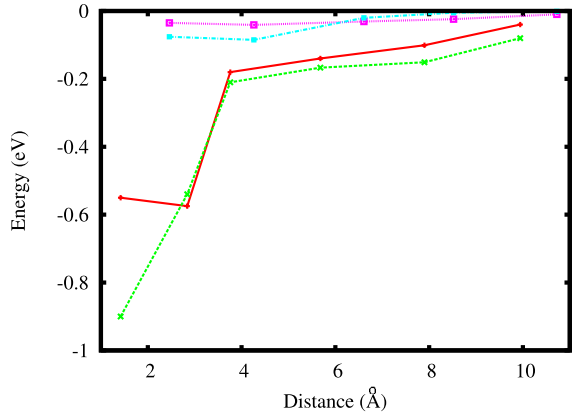

Figure 12.2. *Hydrogen pair adsorbed on graphene: adsorption on the same side and sublattice (blue), the same side but different sublattice (red), different side and sublattice (green), and different side but same sublattice (violet). The binding energy is given per H atom and is given with respect to single H adsorption. (Figure taken from Ref. [80].)*

observation is explained in Ref. [80] as the consequence of the different magnetic states that result from adsorption on the same and different sublattices.

12.3 DFT study of graphane and graphene fluoride

When more and more atoms adsorb to graphene, all C atoms will eventually be saturated and some new crystalline graphene derivatives can emerge. In this section I discuss different stoichiometric configurations of two fully covered graphene derivatives, namely graphane and graphene fluoride. Their structural and electronic properties are examined and the similarities and differences among the various configurations are discussed.

12.3.1 Introduction

The use of graphene for applications in electronics suffers from a major drawback: graphene is, in its pristine state, a zero-bandgap semiconductor and this gapless state appears to be rather robust. Several ways have been explored to induce a finite band gap in graphene. It was found experimentally that a band gap can be opened by confining the electrons as in nanoribbons [81] or by applying a potential difference over a graphene bilayer [82, 83].
The chemical modification of graphene is another promising way to create a band gap [78, 84–86]. When radicals such as oxygen, hydrogen, or fluorine atoms are

adsorbed on the graphene surface they form covalent bonds with the carbon atoms. These carbon atoms change their hybridization from sp^2 to sp^3, which leads to the opening of a band gap (similar as in diamond). The adsorbed radicals can attach to the graphene layer in a random way, as is the case in graphene oxide (GO) [87, 88], or they can form ordered patterns. In the last case, new graphene-based 2D crystals are formed with properties that can vary greatly from their parent material. This has been found to be the case for hydrogen and fluorine adsorbates. The new 2D crystals that are expected to form in those cases[89] have been named graphane [78, 90] and graphene fluoride (or fluorographene)[86], respectively.

Following this route, multi-layer graphene fluoride was recently synthesized [84, 85], and its structural and electronic properties were studied. A strongly insulating behavior was found with a room temperature resistance larger than 10GΩ, which is consistent with the existence of a large band gap in the new material [84, 85]. Only a partial fluorine coverage of the graphene multi-layer samples was achieved in these experiments. The F/C ratio was estimated to be 0.7 in Ref. [84] and 0.24 in Ref. [85], according to weight gain measurements.

Another important step forward in creating fully covered two-dimensional graphene fluoride samples was recently achieved in Ref. [86]. The obtained single-layer graphene fluoride exhibits a strong insulating behavior with a room temperature resistance larger than 1TΩ, a strong temperature stability up to 400°C, and a disappearance of the graphene Raman peaks associated with regions that are not fully fluorinated [86]. The graphene Raman peaks do not disappear completely, however, which could be an indication of the presence of defects in the sample, such as a small portion of carbon atoms not bonded to fluorine atoms. It was also found experimentally that fluorographene has a Young's modulus of ≈ 100 N/m, and the optical measurements suggest a band gap of $\approx$ 3eV.

On the theoretical side, first-principles studies on graphene monofluoride started in 1993, motivated by available experiments on graphite monofluoride. Using density functional theory (DFT) calculations, it was shown in Ref. [91] that the chair configuration of graphene fluoride is energetically more favorable than the boat configuration by 0.145 eV per CF unit (0.073 eV/atom), while a transition barrier of the order of 2.72 eV was found between both structures. Due to the small difference in formation energy and the large energy barrier between both configurations, it was argued that the kinematics of the intercalation could selectively determine the configuration, or that there could also be a mixing of both configurations in the available experiments. By using the local density approximation (LDA) for the exchange-correlation functional a direct band gap of 3.5 eV was calculated for the chair configuration in Ref. [91]. However, it is well known that DFT generally underestimates the band gap. Recent calculations used the more accurate GW approximation and found a much larger band gap of 7.4 eV for the chair configuration of graphene monofluoride (Ref. [92]). This theoretical value is twice

as large as the one obtained experimentally for graphene fluoride in Ref. [86], which is ≈ 3eV. The experimental value for the Young's modulus of Ref. [86] (≈ 100 N/m) is also half the value obtained recently from first-principles calculations in Ref. [93] (≈ 228 N/m) for the chair configuration of graphene fluorine. It is worth noting that the experimental [50] and theoretical [94] values of the Young's modulus of graphene only differ in a small percentage.

Possible reasons for the disagreement between the experimental values and the ab initio results for the Young's modulus and the band gap of graphene fluorine could be i) the presence of a different configuration or a mixture of them in the experimental samples, or ii) the presence of defects, which could decrease the values of both the Young's modulus and the band gap from the expected theoretical values.

The interest in fluorinated or hydrogenated carbon materials is not restricted to graphene. The fluorination of carbon nanotubes and fullerenes is also an important subject of experimental [95] and theoretical [96–98] studies. It can be expected that the results obtained in the following are transferable to relatively large CNT's.

12.3.2 Computational details

Different graphane and graphene fluoride configurations are examined with the use of *ab initio* calculations performed within the density functional theory (DFT) formalism. A PBE-GGA exchange-correlation functional is used and a plane wave basis set with a cutoff energy of 40 hartree is applied. The sampling of the Brillouin zone is done with the equivalent of a $24 \times 24 \times 1$ MP k-point grid for a graphene unit cell and pseudopotentials of the Troullier-Martins type are used [27]. Since periodic boundary conditions are applied in all 3 dimensions a vacuum layer of 20 bohr is included to minimize the (artificial) interaction between adjacent layers. All the calculations were performed with the ABINIT code [37].

I also make use of quasiparticle corrections for the band gap which were obtained by a colleague (Hartwin Peelaers) using the YAMBO code [99]. Here the first-order quasiparticle corrections are obtained using Hedin's GW approximation [100] for the electron self-energy. Because two-dimensional systems are considered here, the spurious Coulomb interaction between a layer and its images should be avoided as this causes serious convergence problems. Therefore a truncation of this interaction in a box layout is used, following the method of Rozzi *et al.* [101]. The remaining singularity is treated using a random integration method in the region near the gamma point [99]. Nevertheless, a larger separation between the layers is necessary, so a value of 60 bohr is used for these calculations.

12.3.3 Results

Four different stoichiometric configurations are studied for both graphane and graphene fluoride and in which every carbon atom is covalently bonded to an adsorbate in an equivalent way, i.e. every carbon/adsorbate pair has the same environment. These configurations are schematically depicted in Fig. 12.3 and I refer to them as the 'chair', 'boat', 'zigzag', and 'armchair' configuration. The chair and boat configurations have been well investigated before, but the zigzag and armchair configurations are rarely examined for graphane[89] and not at all for fluorographene. The names of these last two configurations have been chosen for obvious reasons (see Fig. 12.3(c) and 12.3(d)). After relaxation, the different configurations appear greatly distorted when compared with the schematic pictures of Fig. 12.3, so these figures should only be regarded as topologically correct (see Fig. 12.4).

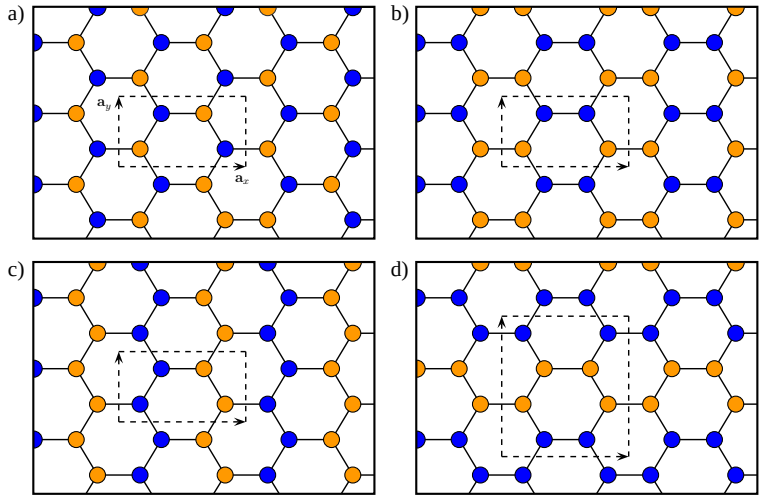

Figure 12.3. *Four different configurations of hydrogen/fluorine-graphene: a) chair, b) boat, c) zigzag, and d) armchair configuration. The different colors (shades) represent adsorbates (H or F) above and below the graphene plane. The orthogonal supercells used to calculate the elastic constants are indicated by dashed lines.*

Stability analysis

To examine the stability of the different configurations, the formation energy of the structures and the binding energy between the graphene layer and the adsorbates are used. The formation energy, E_f, is defined as the energy per atom of the hydrogenated or fluorinated graphene with respect to intrinsic graphene and the corresponding diatomic molecules H_2 and F_2. The binding energy, E_b, is defined

with respect to graphene and the atomic energies of the adsorbates and is calculated per CH or CF pair. The results are summerized in Table 12.3.

Table 12.3. *The formation energy E_f, the binding energy E_b, and the relative binding energy ΔE_f (with respect to the most stable configuration) for different hydrogenated and fluorinated graphene configurations. The energies are given in eV.*

	chair	boat	zigzag	armchair
graphane				
E_b	-2.481	-2.378	-2.428	-2.353
E_f	-0.097	-0.046	-0.071	-0.033
ΔE_f	0.000	0.051	0.027	0.064
fluorographene				
E_b	-2.864	-2.715	-2.791	-2.673
E_f	-0.808	-0.733	-0.772	-0.712
ΔE_f	0.000	0.075	0.036	0.095

As has been reported before, the chair configuration is the most stable one for both graphane [90] and graphene fluoride [102]. The zigzag configuration is found to be more stable than the boat and armchair configurations. The binding energies of hydrogen and fluorine are rather similar (2.5 eV compared to 2.9 eV) but there is a huge difference in the formation energies (0.1 eV compared to 0.9 eV). This is a consequence of the large difference in the dissociation energy between hydrogen and fluorine molecules. The formation energy as defined above can be regarded as a measure of the stability against molecular desorption from the graphene surface. Therefore graphene fluoride is expected to be much more stable than graphane as has indeed been observed experimentally [78, 86].
The energy differences between the various configurations are more pronounced for graphene fluorine than for graphane but they are of the same order of magnitude.

Structural properties

Besides the large difference in formation energy there are also pronounced structural differences between both graphene derivatives. The structural constants for the different configurations of graphane and fluorographene are shown in Table 12.4. Note that all the structures are described in an orthogonal supercell, as illustrated in Fig. 12.3, for ease of comparison. The results for the chair configuration agree well with previous theoretical calculations for graphane [90, 103, 104] and graphene fluoride.[102]
It is also useful to compare the interatomic distances and bond angles with those of graphene and diamond. These were already calculated before (see chapter 6). The

Table 12.4. *Structure constants for the different hydrogenated and fluorinated graphene derivatives. Distances are given in Å and angles in degrees. The distance between neighboring C atoms, d_{CC}, and the angles, θ_{CCX}, are averaged over the supercell.*

	chair	boat	zigzag	armchair
graphane				
$a_x/\sqrt{3}$	2.539	2.480	2.203	2.483
a_y/n_y	2.539	2.520	2.540	2.270
d_{CH}	1.104	1.099	1.099	1.096
$\overline{d}_{\mathrm{CC}}$	1.536	1.543	1.539	1.546
$\overline{\theta}_{\mathrm{CCH}}$	107.4	107.0	106.8	106.7
$\overline{\theta}_{\mathrm{CCC}}$	111.5	111.8	112.0	112.1
fluorographene				
$a_x/\sqrt{3}$	2.600	2.657	2.415	2.662
a_y/n_y	2.600	2.574	2.625	2.443
d_{CF}	1.371	1.365	1.371	1.365
$\overline{d}_{\mathrm{CC}}$	1.579	1.600	1.585	1.605
$\overline{\theta}_{\mathrm{CCF}}$	108.1	106.0	104.6	104.2
$\overline{\theta}_{\mathrm{CCC}}$	110.8	112.8	113.9	114.2

C-C bond has a length of 1.42 Å for graphene compared to 1.54 Å for diamond, and the bond angles are 120° and 109.5°, respectively. Notice that both graphane and fluorographene resemble much closer the diamond structure than graphene, which is not surprising since the hybridization of the carbon atoms in these structures is the same as in diamond, i.e. sp^3. The C-C bond length for the graphane configurations is similar to the one in diamond, but $\overline{d}_{\mathrm{CC}}$ in fluorographene is about 0.05 Å larger. This can be explained from a chemical point of view as the consequence of a depopulation of the bonding orbitals between the carbon atoms. The depopulation of these bonding orbitals results from an electron transfer from the carbon to the fluorine atoms due to the difference in electronegativity between C and F. The modified iterative Hirshfeld method indicates a charge transfer $\Delta Q \approx 0.3e$ from C to F.

The fact that the fluorine atoms are negatively charged has an appreciable influence on the structure of graphene fluoride when compared to graphane. This can, e.g., be seen from the sizes of the different bond angles. The bond angles (and also the bond lengths) in the chair configuration can be regarded as the ideal angles (lengths) for these structures because they can fully relax. The other configurations will try to adopt these ideal bond angles and it can be seen from Table 12.4 that this is indeed the case for the graphane configurations. The fluorographene configurations, on the other hand, appear to be somewhat distorted because their bond angles are (relatively) far from ideal. This is probably caused by the repulsion between the

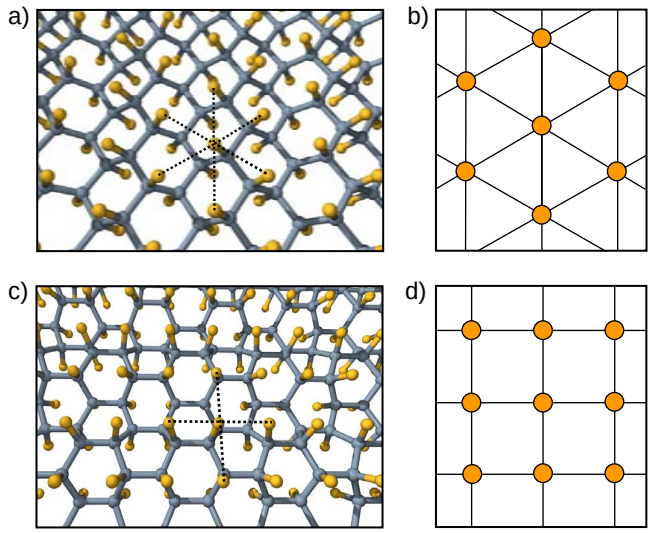

Figure 12.4. *Fluorographene in the zigzag (a) and armchair (c) configuration. The nearest neighbor bonds of one F atom are indicated with dotted lines to show the symmetry of the superlattices (as shown in (b) and (d)). b) The hexagonal superlattice which is formed in case of chair and zigzag configurations. d) The cubic superlattice which is formed in case of boat and armchair configurations.*

different fluorine atoms as can be demonstrated when focusing only on the positions of the F atoms. The fluorine atoms appear to form hexagonal or cubic superlattices depending on the configuration (see Figs. 12.4(b) and 12.4(d)). This is trivial in the case of the chair (and maybe the boat) configuration but not so for the others (see Figs. 12.4(a) and 12.4(c)). These superlattices are not perfect (deviations of a few percent), but are much more pronounced than in the case of graphane.

So it seems that, at the cost of deforming the bonding angles, F superlattices are formed to minimize the electrostatic repulsion between the charged F atoms.

Elastic strain

Graphene and its derivatives graphane and fluorographene can be isolated and made into free-hanging membranes. This makes it possible to measure the elastic constants of these materials from nanoindentation experiments using an atomic force microscope [50, 78, 86]. The experimental elastic constants can be compared to first-principles calculations which gives us information about the purity of the experimental samples. Therefore the (2D) Young's modulus, E', and the Poisson's ratio, ν, are calculated the different graphane and fluorographene configurations, see Table 12.5. The Young's modulus and the Poisson's ratio of graphene are found to be $E' = 336$ Nm^{-1} and $\nu = 0.17$, respectively, which corresponds well to the

experimental value, $E'_{\text{exp}} = 340 \pm 50$ Nm^{-1}, and other theoretical results [93, 105].

Table 12.5. *Elastic constants of the different hydrogenated and fluorinated graphene derivatives. The 2D Young's modulus, E', and Poisson's ratio, ν, are given along the cartesian axes. E' is expressed in Nm^{-1}.*

	chair	boat	zigzag	armchair
graphane				
E'_x	243	230	117	247
E'_y	243	262	271	142
ν_x	0.07	-0.01	0.05	-0.05
ν_y	0.07	-0.01	0.11	-0.03
fluorographene				
E'_x	226	238	240	215
E'_y	226	240	222	253
ν_x	0.10	0.00	0.09	0.02
ν_y	0.10	0.00	0.11	0.02

The 2D Young's modulus of graphane and fluorographene is smaller than that of graphene. The E' of the chair and boat configurations of both graphene derivatives are about 2/3 the value of graphene which makes them very strong materials. The Young's modulus for the zigzag and armchair configurations of graphane are highly anisotropic with values that are roughly halved along the direction that shows the largest crumpling (see Figs. 12.4 (a) and (c)). The situation is completely different for fluorographene where the Young's modulus is more isotropic. The values that are found for the chair configurations agree well with recent calculations [93, 105]. Nair *et al.* performed a nanoidentation experiment on fluorographene [86] and measured a value of 100 ± 30 Nm^{-1} for E'_{FG}. This value is approximately half the theoretical value, which suggests that the experimental samples still contain a lot of defects [105].
The Poisson's ratio shows a similar behavior as the Young's modulus. The knowledge of E' and ν allows us to calculate all the other 2D elastic constants[106] such as the bulk, K', and shear modulus, G'. For the chair configurations these elastic constants are $K'_{\text{HG}} = 131$ Nm^{-1} and $G'_{\text{HG}} = 114$ Nm^{-1} for graphane, and $K'_{\text{FG}} = 126$ Nm^{-1} and $G'_{\text{FG}} = 103$ Nm^{-1} for graphene fluoride.

Electronic properties

Graphene is a zero-gap semiconductor but its derivatives have large band gaps, similar to diamond. In Table 12.6, the band gaps of the configurations under study are given. The GW calculations were performed because GGA is known to underestimate the band gap. The GGA results show that the band gap is

independent of the configuration for graphane. For fluorographene one can notice some variation in the size of the band gap with larger band gaps for the more distorted configurations.

The GGA results give a band gap of 3.2 eV for the most stable fluorographene configuration which is in accordance with the experimental result of ∼3 eV as found in Ref. [86]. However, this value is much smaller than the (more accurate) GW band gap of 7.4 eV, so that there is actually a conflict between the theoretical and experimental results. This conflict might be resolved if the experimental value is ascribed to midgap states due to defects in the system, such as missing H/F atoms (similar to what has been predicted for defected graphane [107]).

Table 12.6. *Electronic properties of the different hydrogenated and fluorinated graphene derivatives. The electronic band gap, E_{gap}, is given for GGA and GW calculations. The ionization energy (IE) is also calculated. All the energies are given in eV.*

	chair	boat	zigzag	armchair
graphane				
E_{gap} (GGA)	3.70	3.61	3.58	3.61
E_{gap} (GW)	6.05	5.71	5.75	5.78
IE	4.73	4.58	5.30	4.65
fluorographene				
E_{gap} (GGA)	3.20	3.23	3.59	4.23
E_{gap} (GW)	7.42	7.32	7.28	7.98
IE	7.69	7.64	7.85	8.27

The electronic band structure and the corresponding density of states of graphane and fluorographene in the chair configuration are shown in Fig. 12.5. Both band structures look similar but there are also some clear differences. In the case of fluorographene the parabolic band at the Γ-point corresponding to quasi-free electron states is at much higher energies which indicates a larger ionization energy for fluorinated graphene. This ionization energy (IE) is defined as the difference between the vacuum level and the valence band maximum and an explicit calculation of this energy indicates a difference of about 3 eV between graphane and fluorographene (see Table 12.6). This is a consequence of the negative charges on the fluorine atoms in fluorographene. These IE values can be compared with the work function of graphene which is the same as its ionization potential (because graphene has no band gap) and has a value of 4.22 eV for GGA (this is somewhat smaller that the experimental value of 4.57±0.05 eV [72]). It can be seen from Table 12.6 that the ionization energies of both graphene derivatives are higher than that of graphene, although the ionization energy of graphane is rather similar to graphene.

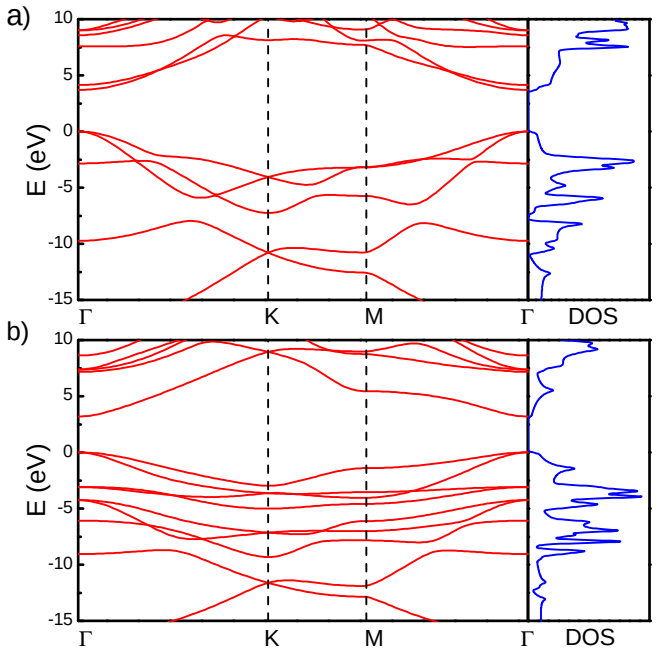

Figure 12.5. *The electronic band structure and the corresponding density of states for the chair configuration of graphane (a) and fluorographene (b). The valence band maximum has been used as the origin of the energy scale.*

12.4 Summary and conclusions

Different configurations of the graphene derivatives fluorographene and graphane were investigated. The chair configuration is the most stable one in both cases, but the zigzag configuration has only a slightly higher formation energy and is more stable than the better known boat configuration. Fluorographene is found to be much more stable than graphane which is mainly due to a much higher desorption energy for F_2 as compared to H_2. It was also demonstrated that there are structural and electronic differences that are caused by the charged state of the F atoms in fluorographene. If the results are compared to available experimental data for fluorographene there appear to be some discrepancies: for all the configurations studied, much larger band gaps in the electronic band structure are found and also the Young's modules is calculated to be much larger. This might indicate that the experimental samples still contain appreciable amounts of defects. The nature of these defects requires further investigation, but one can speculate that these defects consist of missing adsorbates, partial H/F coverage, or mixed configurations.

Chapter 13

Hydrogenation of bilayer graphene

13.1 Introduction

In the previous chapter, the hydrogenation and fluorination of single layer graphene was investigated. In this chapter, however, the hydrogenation of a bilayer of graphene is considered. The maximum coverage of H atoms is examined and the stability of partially hydrogenated bilayer graphene systems is investigated. I will show that when both sides of the bilayer are exposed to atomic hydrogen and when adsorption takes place on one of the two crystal sublattices (on each side), the weak van der Waals bonding is replaced by strong chemical bonds between the two layers which stabilize the system and lead to a new material. Chemical bonding between graphene layers has been investigated before in the context of graphite fluorination[108] or irradiated graphite, in which case point defects (e.g. vacancies and interstitial atoms) can induce interlayer bonding.[109]
The coverage of hydrogen atoms on bilayer graphene can reach a maximum of 50 atomic % and in this case a bilayer analogue of graphane is formed. The geometrical bond lenghts and angles of this bilayer of graphane are between those of graphane and diamond, but the electronic properties are similar to those of single layer graphane.

13.2 Computational details

All the calculations are done within the density functional theory (DFT) formalism as implemented in the ABINIT simulation code[37]. The projector augmented-wave method [110] is used here which allows to reduce the cutoff energy of the plane wave

basis set to 20 Hartree. Different supercells, ranging from 2×2 to 4×4, were used for simulation of the different systems. The sampling of the Brillouin zone was done for these different supercells with the equivalent of a $12 \times 12 \times 1$ Monkhorst-Pack k-point grid [39] for a single graphene unit cell. Spin polarization was included where necessary.[80] For most calculations the local density approximation (LDA) is used for the exchange-correlation functional which was shown to give a better description of the interlayer binding in graphite than the generalized gradient approximation (GGA).

13.3 Results

The main focus is on the formation of chemical bonds between the two layers of graphene as a consequence of hydrogen adsorption. Therefore it is first investigated whether this is possible in principle or not. If any chemical bond between the two layers is possible, it is more likely to occur between two carbon atoms belonging to different layers that are closest to each other, i.e. atoms of the A and B' sublattices as defined in Fig. 13.1. For the formation of a chemical bond between these atoms, it is necessary they change their hybridization from sp^2 to sp^3 because they have to be able to form four bonds now.

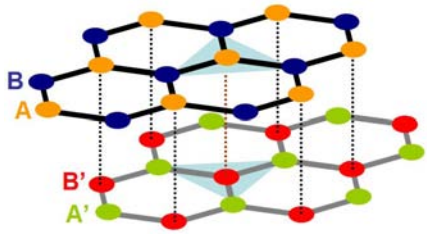

Figure 13.1. *Bilayer of AB stacked graphene with the 4 different sublattices indicated by different colors. The A and B' sublattice are situated on top of each other as illustrated by the dotted lines. The carbon atoms at the corners of the light triangles indicate the 6 neighbors to be hydrogenated.*

Two neighboring atoms of different layers can be brought closer to each other to form a chemical bond, but it is obvious that this can not result in a stable system because the deformation of the two layers costs much more energy than can be gained by forming a new bond: when the two atoms form a new bond they move out of the graphene planes and force their neighbors to change their hybridization from sp^2 because the three bonds formed by these neighboring atoms are not lying in a plane. It is reasonable to suggest that hydrogenation of the neighboring atoms (i.e. atoms of the B and A' sublattice) can result in a stable system because this

makes sure they already have the right hybridization. For this, hydrogen atoms must be able to chemisorb on pure bilayer graphene which was recently shown theoretically to be possible.[111, 112]

Table 13.1. *Interlayer chemical bond formation in a 2×2 supercell. The binding energy per H atom (E_b) and the average(d_{avg}) and minimum distance (d_{min}) between the C atoms of the two layers are shown for different numbers of adsorbed hydrogen atoms and different configurations. Energies are given in eV and distances in Å.*

# H atoms	configuration	E_b	d_{avg}	d_{min}	chem. bond
1	B	-1.084	3.274	3.231	no
2	BB	not stable			
2	BA'	-1.266	2.965	2.853	no
3	BBB	not stable			
3	BBA'	-1.326	2.564	1.660	yes
4	$BBBA'$	-1.426	2.440	1.591	yes
4	$BBA'A'$	-2.018	2.347	1.600	yes
5	$BBBA'A'$	-2.036	2.278	1.574	yes
6	$BBBA'A'A'$	-2.295	2.025	1.550	yes

Table 13.2. *Interlayer chemical bond formation in a 3×3 and 4×4 supercell. The binding energy per H atom (E_b) is shown for different numbers of adsorbed hydrogen atoms and different configurations.*

	3×3		4×4	
configuration	E_b	chem. bond	E_b	chem. bond
B	-1.107	no	-1.225	no
BB	-1.087	no	-1.131	no
BA'	-1.195	no	-1.296	no
BBB	-1.027	no	-0.989	no
BBA'	-1.169	no	-1.218	no
$BBBA'$	-1.334	yes	-1.042	no
$BBA'A'$	-1.466	yes	-1.457	yes

In an AB stacked bilayer of graphene the A and B (or A' and B') sublattices are no longer completely equivalent which results in a different adsorption energy for a hydrogen atom on these two sublattices: adsorption on the B (or A') sublattice is more favorable by 0.03 eV as compared to adsorption on the A (or B') sublattice. Although this difference is small, it might be important for interlayer bonding because the carbon atoms that should be hydrogenated belong to the more favorable

sublattice. The two carbon atoms involved in the interlayer bonding each have 3 neighbors that need to be hydrogenated to get the right hybridization (see Fig. 13.1). However it may be sufficient to hydrogenate some of these neighbors to make the interlayer bond already stable.
To investigate this a 2×2 supercell of bilayer graphene containing 16 carbon atoms (8 per layer) is used and the hydrogenation is gradually increased by putting hydrogen atoms on the six neighbors (3 of the B and 3 of the A' sublattice) of the two carbon atoms between which a possible interlayer chemical bond might be formed. it can be seen from table 13.1 that there is a jump in the minimal interlayer C-C distance (d_{min}) after the adsorption of 3 hydrogen atoms, 2 on one layer and 1 on the other. This indicates the formation of an interlayer chemical bond as illustrated in Fig. 13.2(a). Adsorption of hydrogen atoms on a single sublattice of one side does not result in any stable structure in a 2×2 supercell. Notice that the average interlayer distance (d_{avg}) becomes smaller when more carbon atoms are hydrogenated. This means that the carbon atoms of the different layers, that do not participate in interlayer bond formation, start repelling each other more and more. For lower concentrations of H atoms, i.e. larger supercells, there are more repelling carbon atoms so it is likely that the interlayer bond needs to be stronger. This was checked in a 3×3 and a 4×4 supercell and the results are shown in table 13.2: in a 3×3 (36 C atoms) supercell one needs two hydrogenated neighbors on each side (see Fig. 13.2(c)), so 4 in total, or 3 on one side and 1 on the other side of bilayer graphene (Fig. 13.2(d)). In a 4×4 supercell (64 C atoms) both sides need at least 2 hydrogenated neighbors (Fig. 13.2(b)). For still lower concentrations (thus still larger supercells) the same result is found as for the 4×4 supercell, so it seems that hydrogenation of four of the six neighbors, two on each side, is generally sufficient to induce a chemical bond. Table 13.1 and 13.2 also show that it is more favorable (in all supercells) to divide the number of hydrogen atoms as symmetrical as possible between the two graphene layers, e.g. the $BBA'A'$ configuration has lower energy than the $BBBA'$ configuration.

In any case it is essential that the H atoms bind to both sides of the bilayer in order to have an interlayer bond. This means that both sides of the bilayer should be exposed to hydrogen, since it is known that graphene is very hard to penetrate [113, 114].
Now that I demonstrated that interlayer chemical bonds are possible in principle, I will investigate whether or not they are stable. The bond formation is only possible when all H atoms adsorb on the same sublattice on both sides of the bilayer. It was shown that for a single H atom there is a difference in binding energy of 0.03 eV in favor of the sublattice that should be hydrogenated. However it has been demonstrated theoretically [111, 115] and experimentally [116–118] that hydrogen atoms tend to adsorb on different sublattices of graphitic surfaces to avoid the

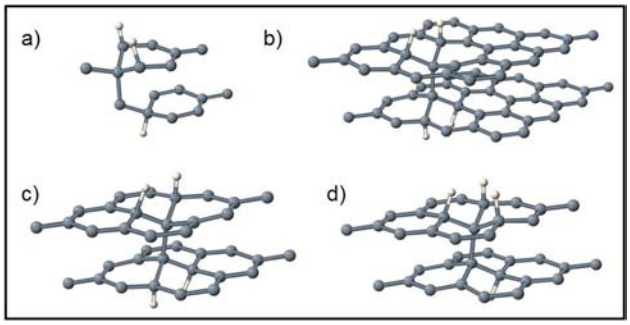

Figure 13.2. *Formation of a chemical bond between the two layers in bilayer graphene in a* 2×2 *(a), a* 4×4 *(b), and a* 3×3 *(c,d) supercell. The light colored atoms are H, the others C.*

presence of unpaired electrons. Boukhvalov and Katsnelson showed that in this way hydrogen coverage is limited to a maximum of 25 at. % (on each side) because otherwise first and second neighbors are unavoidably filled and this is energetically unfavorable [111]. It is demonstrated, however, that it is possible to reach 50% hydrogen coverage when the two sides of the bilayer are available for adsorption. For this I will again make use of the 2×2 supercell and add consecutively more and more H atoms. There are a lot of different configurations possible, even for a fixed number of adsorbed hydrogen atoms, so some guidance is needed to find the most stable ones. I showed before that when the H atoms adsorb on the same sublattice they will be distributed as symmetrical as possible between the two layers. This can be used as a first guide, but, as stated above, there are probably more favorable configurations with the H atoms distributed over both sublattices. In search of these configurations I make use of earlier theoretical [80, 111, 115] and experimental[116–118] works in which it was found that the formation of two kinds of hydrogen dimers are energetically more favorable after hydrogenation of graphitic surfaces. These dimers are shown in the inset of Fig. 13.3 together with the most stable trimer configuration, which is a combination of the two dimers, as suggested in Refs. [117] and [119].

As a measure for the stability of the bilayer graphene samples with different concentrations of chemisorbed hydrogen atoms the formation energy per hydrogen atom is used. As done by Sofo *et al.* the energies of graphite and the H_2 molecule [90] are chosen as the reference energies. The results are shown in Fig. 13.3.

From the calculations presented in Fig. 13.3 it can be seen that for low concentration of H atoms (< 25 at. %) the configurations with hydrogenation of both sublattices is much more stable. This means that no interlayer chemical bonds will be formed for these concentrations. High concentrations of H atoms (> 25 at. %) are not possible for the dimer configurations because the formation energy

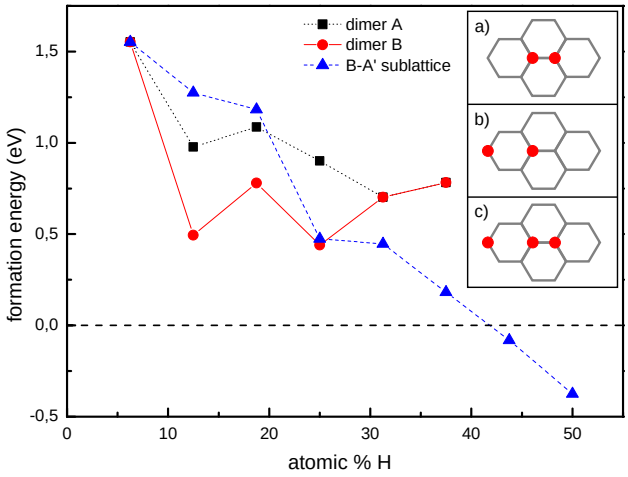

Figure 13.3. *Hydrogenation of* 2×2 *supercell of bilayer graphene. The formation energy per hydrogen atom is shown for increasing H concentration. The 3 curves show 3 different ways of distributing the H atoms: according to dimer configuration a (inset (a)), b (inset (b)), and by placing the H atoms only on sublattice B and A'. Inset (c) shows the trimer configuration which is a combination of dimer a and b. The curves of the two different dimer configurations are the same if the trimer is formed, because the trimer is a combination of these two dimers.*

increases too much, as was already noted in Ref. [111]. But if only the B and A' sublattice are hydrogenated the formation energy still decreases at high concentration until complete hydrogenation has been reached, i.e. all carbon atoms have 4 neighbors and are completely saturated (see Fig. 13.4). The fully hydrogenated bilayer of graphene has negative formation energy as compared to graphite and H_2 and is therefore a very stable structure. If the formation energy is calculated with respect to bilayer graphene and atomic hydrogen, as would be typical in an experimental setup, this results in an almost constant shift of 2.5 ± 0.1 eV to lower energies which makes all energies given in Fig. 13.3 negative. This suggests that, in principle, all structures could be formed at high enough temperatures so that possible formation barriers can be overcome [80, 117]. Large energy barriers are also expected in going from hydrogenation of both sublattices to hydrogenation of a single sublattice as the hydrogen concentration increases [117]. One way to avoid these barriers could be to introduce already some interlayer chemical bonds in the bilayer before hydrogenation by e.g. fs laser excitation [120] or the introduction of point defects through irradiation [109].

Table 13.3. *Properties of single layer and bilayer graphane: the unit cell length (a), the distances (d) and angles (θ) between neighboring atoms, the formation energy (E_F) and the band gap at the Γ point (ΔE). Energies are given in eV, distances in Å, and angles in deg.*

	graphane		bilayer graphane		diamond	
	LDA	GGA	LDA	GGA	LDA	GGA
a	2.505	2.544	2.500	2.535	2.497	2.530
d_{C-C}	1.515	1.539	1.521	1.543	1.529	1.549
$d_{C-C'}$			1.545	1.562	1.529	1.549
θ_{CCC}	111.6	111.5	110.5	110.5	109.5	109.5
$\theta_{CCC'}$			108.4	108.4	109.5	109.5
θ_{CCH}	107.3	107.4	108.4	108.4		
E_F/atom	-0.183	-0.104	-0.125	-0.028	-0.010	0.122
ΔE	3.376	3.480	3.031	3.137	5.629	5.568

13.4 Properties of bilayer graphane

It was found that the energetically most favorable configuration for hydrogen atoms on a bilayer of graphene appears when two of the four sublattices (B and A' as indicated in Fig. 13.1) are fully hydrogenated (see Fig. 13.4). In this case one could speak of bilayer graphane in analogy with a fully hydrogenated monolayer of graphene. Let us now take a look at some properties of this material and compare them to the single layer case and diamond. The results for the geometrical and electronic properties are given in table 13.3. For single layer graphane, the results are in good agreement with earlier studies of this material.[80, 90] The properties of bilayer and single layer graphane are very similar, but there are differences. When the geometrical distances and angles are considered, one can see that those of the bilayer are intermediate between those of the single layer and bulk diamond. The corresponding geometrical results are also shown for GGA in table 13.3 because GGA is more accurate in predicting the actual bond lengths. The formation energy of bilayer graphane is larger than that of single layer graphane, but it is closer to the formation energy of graphane than that of diamond.
The electronic properties of both single layer and bilayer graphane are quite similar (Fig. 13.5). The band gap of the bilayer is slightly smaller, but it is not certain whether this has any physical significance because it is well known that band gaps are not well described in LDA (or GGA). The reason that single and bilayer graphane have similar electronic properties is that the C atoms in both materials have the same hybridization.

So in conclusion one can say that, in contrast to monolayer and bilayer graphene, monolayer and bilayer graphane have very similar electronic properties.

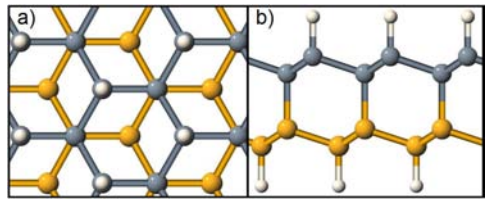

Figure 13.4. *(Color online) Top (a) and side (b) view of a bilayer of graphane. The carbon atoms of the two layers are given different colors for clarity.*

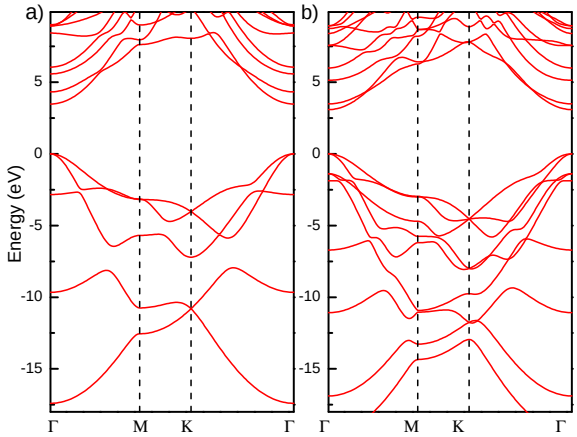

Figure 13.5. *The electronic band structure of monolayer (a) and bilayer (b) graphane. The energies are relative to the Fermi level (E_F =0).*

13.5 Summary and conclusions

Previous theoretical calculations showed that hydrogenation of bilayer graphene can only cause a maximum hydrogen coverage of 25 at. % when both sublattices (on each side of the bilayer) adsorb H atoms.[111] It was demonstrated above that: 1) it is possible to hydrogenate a bilayer of graphene to a limit of 50 at. % through the adsorption of hydrogen atoms on both sides of the bilayer and on a single sublattice per layer, 2) in this case interlayer chemical bonds are formed which stabilize the structure, and 3) when the hydrogenation reaches its limit of 50 at. %, a bilayer analogue of graphane is formed which has qualitatively similar electronic properties as graphane. Although it was shown that bilayer graphane can be made through the hydrogenation of a bilayer of graphene, this procedure is not suited to produce multilayer (>2) graphane. It is essential for the formation of chemical bonds between two layers that both layers are hydrogenated and this is more difficult when more than two layers are present.

Chapter 14

Graphene Membranes

As seen before, graphene can be made into free-standing samples by (partially) etching away the substrate or deposition on a prepatterned substrate with holes into it. This results in an atom-thick membrane that can be used to separate two regions in space. An important issue determining the efficiency of the separation is the permeability of the membrane to atoms and molecules. In this chapter the permeability of (intrinsic and defected) graphene membranes is investigated by *ab initio* molecular dynamics calculations in the DFT formalism. But before the theoretical results are described, some experimental findings (from Ref. [113]) will be summarized.

14.1 Experimental results

In 2008, Bunch *et al.* demonstrated the impermeability of graphene crystals to atmospheric molecules [113] and, consequently, they opened up a new area of applications for graphene as the ultimate membrane at the nanoscale. A schematic view of the free-hanging graphene sample they used is given in Fig. 14.1 a and b. The sample is fabricated by mechanical exfoliation of graphite and deposition of monolayer graphene on a SiO_2 substrate with a hole in it, $4.75\mu\text{m} \times 4.75\mu\text{m} \times 380\text{nm}$ in size (see inset of Fig. 14.1a). In this way a microchamber is created that is sealed by a graphene membrane that is strongly clamped on all sides by vdW interactions between the graphene and the SiO_2 substrate. When the sample is put in a high pressure (690 kPa) environment of N_2 gas for several hours the pressure inside the microchamber, P_{int}, will equilibrate with this external pressure, P_{ext}. When the sample is subsequently put into vacuum the pressure difference will cause the graphene membrane to bulge out as shown in Fig. 14.1c. Similarly, when the sample is first stored in vacuum and subsequently returning it to atmospheric pressure,

the graphene membrane will bulge inward (see Fig. 14.1d). Over time, the internal and external pressures will equilibrate as can be seen from Fig. 14.1e which shows variation of the height of the graphene membrane over a period of 3 days. The deflection at the center of the membrane is initially 175 nm and decreases slowly over time, indicating a slow air leak into the microchamber.

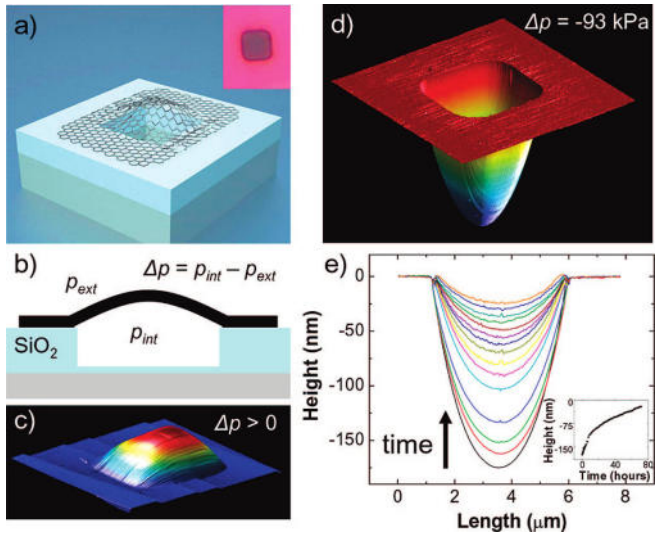

Figure 14.1. *(a) Schematic picture and optical image (inset) of graphene sealed microchamber. (b) Schematic side view of graphene sealed microchamber. (c) AFM image of graphene sealed microchamber with overpressure. (d) AFM image of graphene sealed microchamber with underpressure. (e) AFM line traces through the center of the graphene membrane at different times. Inset: deflection at the center of the graphene membrane as a function of time.*

So it seems that the graphene membrane can sustain substantial pressure differences for some time, but there is no perfect sealing of the microchamber. However, it can be shown that the leakage is not through the graphene membrane but rather through the glass walls of the chamber. Bunch *et al.* demonstrated this by sealing the microchamber with several few layer graphene (1-75 layers) membranes. The gas leak rate as a function of the thickness of the FLG membrane is shown in Fig. 14.2 for several gases. There seems to be no dependence of the leakage on the thickness of the FLG sample. Futhermore, the leakage of He atoms is of the same order as can be estimated from Fick's law for diffusion of He atoms through glass walls [113]. So, in conclusion, the permeability of graphene membranes the to investigated gas molecules appears to be below experimental detectability and graphene can be considered impermeable to all standard gases.
Bunch *et al.* also suggested that the graphene samples should be free of defects to

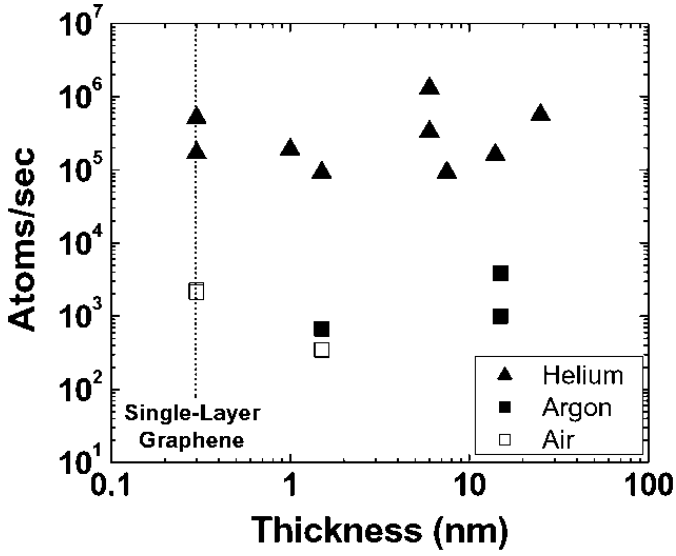

Figure 14.2. *The permeability of FLG as a function of thickness for different gas molecules.*

explain the impermeability [113]. This suggestion was based on a simple classical effusion theory calculation of the penetration of point particles through single atom vacancies in graphene. In the next section, more accurate first-principles density functional theory calculations will be performed to investigate the permeability of a graphene monolayer with defects to check this simple theory.

14.2 Ab initio investigation of graphene membranes

In this study I will concentrate on the penetration of helium atoms through graphene with increasingly large defects. Helium atoms are chosen because they are the smallest atoms that do not chemically interact with graphene. Furthermore the study is limited to point defects that keep the sp^2 hybridization of the carbon atoms of graphene more or less intact. Such defects are more stable [121, 122] and easier to treat in first-principles calculations.

14.2.1 Computational details

The DFT formalism is used here in both the local density (LDA) and general gradient approximation (GGA). All the DFT calculations are performed with the ABINIT software package. The simulation of most defects is done in a $4 \times 4 \times 1$ graphene supercell with a distance of 16 Å between adjacent graphene layers. A plane-wave basis with a cutoff energy of 30 hartree was used and the Brillouin zone

(BZ) is sampled with a $6 \times 6 \times 1$ Monckhorst-Pack (MP) [39] k-point grid which is equivalent to a $24 \times 24 \times 1$ MP grid in a single unit cell. Pseudopotentials of the Troullier-Martins type [27] are used for both the LDA and GGA calculations. There is no need to perform spin-polarized calculations because the defects were chosen to preserve the sp^2 hybridization of the carbon atoms in the simulated defective graphene sheets and the He atom is inert.

14.2.2 Penetration through a perfect graphene membrane

I first examine the penetration of a helium atom through the center of a carbon hexagon of a perfect graphene monolayer. As a first approximation, all the carbon atoms are kept fixed and the potential energy of the He atom at different distances from the graphene sheet is calculated. The resulting energy barrier is given in Fig. 14.3 for both LDA and GGA. The height of the barrier, 18.8 eV for LDA and 11.7 for GGA, is very large and makes penetration of helium gas that is in thermal equilibrium impossible at any temperature at which the graphene layer remains stable.

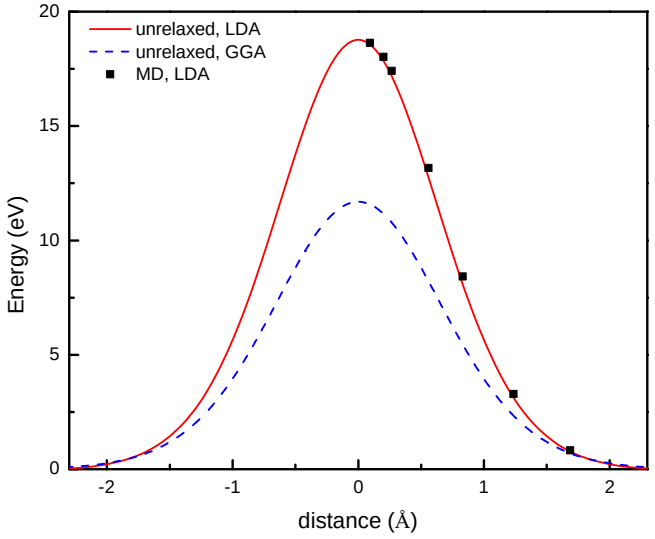

Figure 14.3. *The potential barrier for the penetration of a He atom through the center of a carbon hexagon of a perfect graphene layer. The results for the penetration without relaxation of the graphene layer are shown for LDA and GGA (solid and dashed line respectively). The results of the MD calculations (LDA) are indicated by full squares.*

First-principles molecular dynamics

Next I use velocity-Verlet molecular dynamics [123, 124] simulations to show that the height of the barrier is not essentially decreased when the graphene layer is allowed to relax when the helium atom impinges on the layer. These MD calculations are done within the DFT formalism (LDA) and with full relaxation of the graphene sheet. I start with a nonperturbed graphene sheet and place the He atom above the center of a graphene hexagon at a distance far from the graphene surface where the potential energy is vanishingly small. Then the He atom is given different velocities in the direction of the graphene layer. When the kinetic energy of the He atom is small enough, it will bounce back from the graphene surface at a certain distance d, which is defined to be the difference along the z direction (perpendicular to the graphene surface) between the He atom and the closest C atom of the graphene sheet. The effective potential felt by the He atom depends on its velocity due to the relaxation of the graphene layer. This potential can be constructed from our MD calculations by considering the kinetic energy of the incoming He atom as a function of the distance d at which it is reflected from the graphene layer. The results of the MD calculations are shown in Fig. 14.3 by the black squares. Notice that the difference of the potential felt by the approaching He atom between the relaxed (MD) and the unrelaxed case is very small. This is a consequence of the fact that the graphene atoms appear to lack time to relax while interacting with the fast moving He atom. In Fig. 14.4 the reflection of a He atom with a kinetic energy that is just a little smaller that the energy barrier for penetration is shown. It is clear that the relaxation of the graphene layer is very small at the turning of the He atom (see Fig. 14.4b) and that the relaxation only starts when the He has already been reflected (see Fig. 14.4c). This means that relaxation has no significant influence on the barrier height and from now on it is allowed to ignore any relaxation of the graphene layer when calculating the energy barriers for penetration of the He atom.

The approach used here is different from earlier calculations of the barrier height for the penetration of He into C_{60} fullerenes [125], where the He atom was given a fixed position and the system was allowed to relax completely before calculating the barrier. In my opinion this is actually a less realistic calculation than one where any relaxation is ignored. The reason is that the system relaxes within a much larger time scale than the time scale for motion of the much lighter, chemically inert, He atom. Note that this is not generally true: in the case of other atoms, e.g. a hydrogen atom [126], or molecules, the interaction time can be long enough for the graphene layer to have a significant relaxation, which may be due to the much larger mass of the molecules or as a consequence of chemical reactivity.

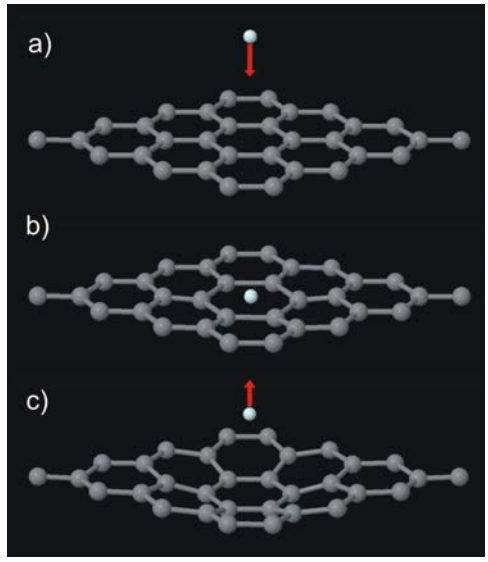

Figure 14.4. *Reflection of a He atom with a kinetic energy of 18.6 eV from a graphene surface: a) The He atom approaches the perfect graphene layer. b) The He atom comes to rest before penetrating the graphene layer. Note that the relaxation of the graphene layer is very small at this moment. c) The He atom is reflected back and the surface starts to relax.*

14.2.3 Penetration through a defected graphene membrane

Let us now turn our attention to the penetration of a defective graphene layer where only those defects are considered that do not destroy the sp^2 hybridization of the carbon atoms. Examples of studied defects (see Fig. 14.5) include the Stone-Wales (SW) defect, the divacancy (585 and 555777), and the tetra-, hexa- and decavacancy. All these defects were fully relaxed in a $4 \times 4 \times 1$ graphene supercell, but for the decavacancy a $6 \times 6 \times 1$ supercell was used. The lowest penetration barrier is always found inside the largest 'ring' of carbon atoms that belongs to the defect. The resulting barriers for the different defects are given in Table 14.1.

As intuitively expected, the barrier height decreases fast with increasing size of the defects. A more quantitative relationship between the barrier height and the size of the defect can be obtained by quantifying the defect size as the number of carbon atoms included in the sp^2-bonded defect ring. In this way, we obtain sizes ranging from 6 (for perfect graphene) to 12 (for the decavacancy). The Stone-Wales defect and the 555777 divacancy both have a size of 7. The barrier height versus defect size is shown in Fig. 14.6. Notice that, to a very good approximation, the penetration barrier height decreases exponentially with the size of the defect (as indicated by the dashed lines). The largest deviation from the exponential behavior is found for the 585 divacancy with 8 carbon atoms in the defect ring. This could

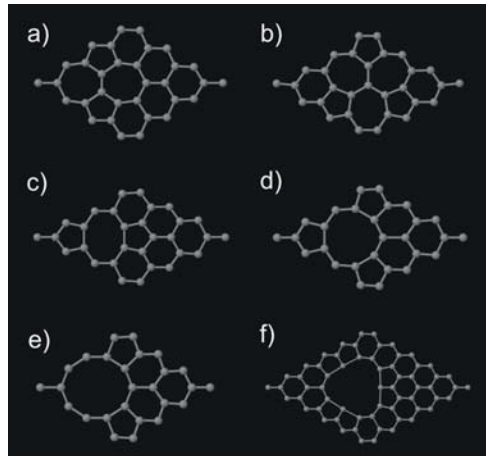

Figure 14.5. *The considered sp^2 hybridization conserving defects: a) Stone-Wales defect, b) 555-777 divacancy, c) 585 divacancy, d) tetravacancy, e) hexavacancy, and f) decavacancy.*

Table 14.1. *The energy barrier height (in eV) for penetration of a He atom through perfect and defective graphene as obtained within LDA and GGA.*

defect	**LDA**	**GGA**
no defect	18.77	11.69
Stone-Wales	9.21	6.12
555777 divacancy	8.77	5.75
858 divacancy	4.61	3.35
tetravacancy	1.20	1.04
hexavacancy	0.37	0.44
decavacancy	0.05	0.10

be a consequence of the noncircular form of the defect (see Fig. 14.5c) which is more pronounced in this defect than in the others. The larger the deviation of the circular form of the defect, the worse is the quantification of the defect size through the number of carbon atoms in the defect ring.

It is also clear from Fig. 14.6 that, although the energy barrier for penetration decreases exponentially, large defects are needed to allow for any appreciable gas leak through a graphene membrane at room temperature (k_BT =26 meV). These findings are in marked contrast to the claim of Ref. [113] that it is necessary to have a perfect graphene layer to preserve the impermeability. This claim was based on a simple classical effusion theory calculation which is clearly not a realistic approximation for the penetration process of He atoms through defective graphene membranes. Our first-principles calculations clearly suggest that small

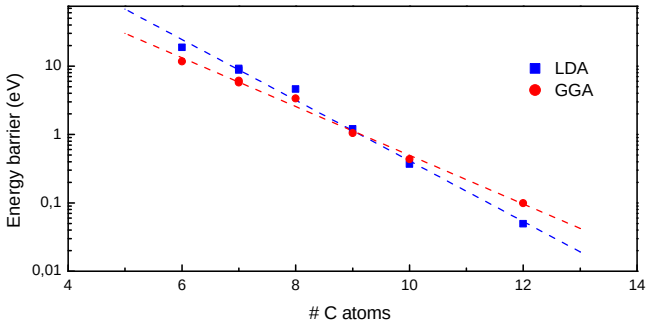

Figure 14.6. *The dependence of the penetration barrier height on the size of the defect for LDA and GGA.*

point defects in graphene will not destroy the impermeability of the membrane.

14.2.4 Summary of results

In summary, I investigated the penetration of a helium atom through perfect and defective graphene. It was found that the relaxation of the graphene layer caused by the impact of the incoming He atom has no influence on the barrier height and can therefore be neglected. This is due to the fact that the time scale for relaxation of the graphene is larger than the time scale during the He atom interacts with the graphene layer. The relaxation of the graphene layer occurs after the He atom has left the graphene layer. We found that the penetration barrier height decreases exponentially with the size of the defects, as expressed by the number of carbon atoms included in the formation of the defect. But the penetration barrier height of small defects is still large enough to preserve the impermeability of graphene membranes for atoms and molecules. Consequently, even defective graphene is a suitable candidate for making impermeable membranes for future applications and therefore can be considered the thinnest possible material for constructing a micro- or nanomembranes.

Part IV

Summary and outlook

Summary of the results

In this thesis, I investigated the interaction of atoms and molecules with graphene, i.e. a single layer of graphite, with the use of density functional theory calculations. Most of the results were interpreted using simpler, more qualitative methods like tight-binding and molecular orbital theory.

The first systems which were examined consist of small molecules interacting with a perfect free-standing graphene monolayer (Chapter 7). The favorable adsorption sites and orientations were searched for and the charge transfer between the molecules and graphene was determined with the Hirshfeld charge analysis method. It was found that the adsorption energy and charge transfer are rather independent of the adsorption site, but strongly depend on the orientation of the molecules with respect to the graphene surface. An explanation for this was found through molecular orbital theory which also allowed to distinguish between two different charge transfer mechanisms. These two mechanisms consist of, on the one hand, a direct doping through the relative positions of the molecular orbitals and, on the other hand, a smaller doping because of orbital hybridization which is always present to some extent. There also appeared to be a qualitative agreement between these DFT results and the experimental findings of Ref. [15].

However, a large variation of calculated charge transfers was noted in the literature and, in case of NO_2 molecules, a quantitative disagreement was found between theory and experiment. This was closer investigated in Chapter 8. Two major causes of the quantitative differences were found: (i) the use of different kinds of charge transfer analysis methods and (ii) the size of the supercell used in the simulations which has a large impact on the resulting charge calculations. To reduce the influence of the first point, a different charge analysis method, based on the Hirshfeld method, was devised which showed to give physically relevant results for the systems under study.

In Chapter 9 the influence of the presence of water clusters and ice layers on the electronic properties of a perfect graphene sheet was studied. The binding energy of the water molecules in a cluster appeared to be an order of magnitude larger than the adsorption energy between the cluster and graphene indicating that graphene is strongly hydrophobic. Charge transfers between a graphene sheet and water clusters, which could influence the density of the charge carriers and consequently the resistance in graphene, are very small. The molecules in a water cluster tend to orient their dipole moments in opposite directions, so that they cancel on average. But in the limit of a large concentration of water molecules such that ice-like structures can be formed the dipole moments of the different molecules accumulate instead of averaging out leading to an appreciable total dipole moment which can have an influence on the electronic properties of graphene.

This influence of the dipole moment was further investigated in the subsequent

chapter in which alternative charge transfer mechanisms were investigated (Chapter 10). It was shown there that a dipole layer is able to shift the free-energy bands and impurity bands with respect to the Fermi level of graphene by changing th relative potentials. This can induce doping if the shift becomes large enough. It was demonstrated through a water-graphene model system that the potential shift restricts itself to the dipole layer side, while the potential at the other side of the graphene layer remains unaffected.
Because the work function of graphene plays an important role in the doping level by the above described mechanism, I investigated how this work function can be changed in Chapter 11. Several ways have been investigated there to tune the work function of graphene. It was demonstrated that only small differences in the WF were obtained by variation of the number of layers in FLG and larger changes can be achieved by applying strain to the graphene samples. In this chapter, it was also shown that the most effective way to change the work function is through doping FLG: depending on the level of doping and the number of graphene layers present in the sample, the WF can be varied over a large range ($\approx$2eV).

In the next two chapters (Chapters 12 and 13) the attention turned to chemisorption instead of physisorption. In other words, the adsorbates studied in these chapters form covalent bonds with the graphene layers. In Chapter 12 two graphene derivatives, namely graphane and fluorographene, were investigated which result from a fully hydrogenated or fluorinated monolayer of graphene, respectively. Different configurations for both derivatives were investigated and it appeared that the chair configuration is the most stable one in both cases. Another, rather unknown, configuration, called the zigzag configuration was demonstrated to have only a slightly higher formation energy and to be more stable than the better known boat configuration. Fluorographene was found to be much more stable than graphane which is mainly due to a much higher desorption energy for F_2 as compared to H_2. It was also demonstrated that there are structural and electronic differences that are caused by the charged state of the F atoms in fluorographene. Comparison of the results to available experimental data for fluorographene revealed some marked discrepancies: for all the configurations studied, much larger band gaps in the electronic band structure are found and also the Young's modules is calculated to be much larger. It was argued that this indicates that the experimental samples still contain appreciable amounts of defects. The nature of these defects requires further investigation with larger supercells.
In Chapter 13, the hydrogenation of a bilayer of graphene was invesigated. It was demonstrated that: 1) it is possible to hydrogenate the bilayer to a limit of 50 at. % through the adsorption of hydrogen atoms on both sides of the bilayer and on a single sublattice per layer, 2) in this case interlayer chemical bonds are formed which stabilize the structure, and 3) when the hydrogenation reaches its limit of

50 at. %, a bilayer analogue of graphane is formed which has qualitatively similar electronic properties as graphane.

The last part of the thesis was concerned with the permeability of defected graphene membranes. The penetration of a helium atom through perfect and defective graphene was investigated for normal incidence. It was found that the relaxation of the graphene layer caused by the impact of the incoming He atom has no influence on the barrier height and can therefore be neglected. This is due to the fact that the time scale for relaxation of the graphene is larger than the time scale during the He atom interacts with the graphene layer. The relaxation of the graphene layer occurs after the He atom has left the graphene layer. The penetration barrier height was found to decrease exponentially with the size of the defects, but it was shown that the barrier height of small defects is still large enough to preserve the impermeability of graphene membranes for atoms and molecules.

Outlook

Many of the calculations that were performed in the thesis can be improved by including explicitly van der Waals interaction in the DFT calculations. Exchange-correlation functionals that include this kind of interaction are being developed at high pace now, but there has not yet emerged any widely applied standard functional.
Another improvement would be the correction of artificial dipole interactions due to the periodicity of the system. This can be done by using larger supercells, i.e. by increasing the computation time and memory, or by the implementation of explicit corrections in the DFT calculations. A simple correction is e.g. to remove the artificial electric fields, resulting from the periodicity requirements for the potential, by introducing an artificial dipole layer in the vacuum region of the supercell with opposite sign (this has already been implemented in a lot of codes, but not yet in ABINIT).

There are still a lot of interesting systems to be explored. E.g. in Chapter 12 the hydrogenation of a monolayer of graphene [80] was discussed. Similar studies for fluorination are still lacking, although some interesting differences might be expected. The C-F bond length will probably be highly dependent on the concentration of F atoms because of the partly ionic character of this bond. In case of fluorination of a bilayer, the induced charges on the carbon atoms might induce some repulsion between the layers, preventing the formation of interlayer chemical bonds such as in hydrogenated bilayers.
Another intriguing system to investigate might be a partly hydrogenated, partly fluorinated graphene sample. It is not easy to see which configurations are most favorable in that case.
It might also be interesting to examine how the adsorption properties of graphene are influenced by defects in the graphene sample. Although defects are usually rare in graphene, it is always possible to induce them to alter the adsorption properties.

Samenvatting

In deze thesis heb ik de interactie van atomen en moleculen met grafeen, een enkele laag grafiet, onderzocht met behulp van dichtheidsfunctionaaltheorie (DFT). De meeste resultaten werden geïnterpreteerd met eenvoudigere, meer kwalitatieve methoden zoals 'tight-binding'-theorie en moleculaire orbitalen.

De eerste systemen die ik onderzocht heb, bestaan uit kleine moleculen die interageren met een perfect grafeenkristal (hoofdstuk 7). De energetische meest voordelige adsorptieplaatsen en -oriëntaties werden bepaald en de ladingsoverdracht tussen de moleculen en grafeen werd berekend met de zogenaamde Hirshfeld-methode. De adsorptie-energie en de ladingsoverdracht blijken vrijwel onafhankelijk van de adsorptieplaats te zijn, maar ze hangen wel sterk af van de oriëntatie van de moleculen t.o.v. het grafeenoppervlak. Dit kon worden verklaard door de interactie tussen de aanwezige moleculaire orbitalen, zodat twee verschillende ladingsoverdrachtsmechanismen onderscheiden konden worden. Deze twee mechanismen bestaan uit enerzijds een dopering ten gevolge van de relatieve posities van de moleculaire orbitalen en anderzijds een geringere dopering ten gevolge van hybridisatie van de orbitalen welke steeds in enige mate aanwezig is. Deze resultaten bleken kwalitatief overeen te stemmen met de experimentele bevindingen in Ref. [15].

Wanneer verschillende theoretische resultaten voor de berekende ladingsoverdrachten uit de literatuur met elkaar vergeleken worden, kan er echter een grote variatie aan waarden vastgesteld worden. Bovendien blijken al deze theoretische waarden kleiner te zijn dan de experimenteel gemeten waarde in het geval van NO_2 moleculen. Dit werd verder onderzocht in hoofdstuk 8. Twee belangrijke oorzaken voor de kwantitatieve verschillen werden vastgesteld: (i) het gebruik van verschillende methoden om de ladingsoverdrachten te berekenen en (ii) de grootte van de supercellen die gebruikt worden in de simulaties, blijken beide een sterke invloed op de resulterende ladingsoverdrachten te hebben. Om de invloed van de eerste oorzaak te verminderen heb ik een andere berekeningsmethode ontworpen, gebaseerd op de Hirshfeld methode, die betere resultaten blijkt te geven voor de onderzochte systemen.

In hoofdstuk 9 werd de beïvloeding van de elektronische eigenschappen van grafeen onderzocht door de aanwezigheid van waterclusters en ijslagen op het grafeenoppervlak. De bindingsenergie van de watermoleculen in een cluster blijkt een orde groter te zijn dan de adsorptie-energie tussen een cluster en grafeen. Dit toont aan dat grafeen sterk hydrofoob is. De ladingsoverdrachten tussen een grafeenlaag en de waterclusters blijken steeds heel klein te zijn. De verschillende moleculen in een watercluster hebben de neiging om hun elektrische dipoolmomenten in tegengestelde richtingen te oriënteren zodat ze gemiddeld gezien tegenover elkaar wegvallen. Maar bij hogere concentraties aan watermoleculen kunnen er ijsstructuren gevormd wor-

den waarbij een sterke dipoollaag gevormd wordt die een sterke invloed op de elektronische eigenschappen van grafeen kan hebben.
De invloed van zo'n dipoollaag werd verder onderzocht in het volgende hoofdstuk waarin ook alternatieve ladingsoverdrachtsmechanismen onderzocht werden (hoofdstuk 10). In dit hoodstuk werd aangetoond dat een dipoollaag de vrije-elektronen banden en eventuele onzuiverheidsbanden kan verschuiven t.o.v. het Fermi-niveau in grafeen door de relatieve potentialen te veranderen. Dit kan tot dopering leiden als de bandverschuivingen groot genoeg worden. Door het bestuderen van een water-grafeen-modelsysteem werd er aangetoond dat de potentiaalverschillen door een dipoollaag beperkt blijven tot de kant van de dipoollaag terwijl de potentiaal aan de grafeenzijde onveranderd blijft.
Omdat de werkfunctie van grafeen een belangrijke rol speelt in het doperingsniveau door het hierboven beschreven mechanisme, heb ik in hoofdstuk 11 onderzocht hoe de werkfunctie veranderd kan worden. Verschillende manieren om de werkfunctie te beïnvloeden werden bestudeerd. Er werd aangetoond dat er slechts kleine variaties optreden wanneer het aantal lagen in FLG (few layer graphene) gewijzigd wordt en dat grotere variaties mogelijk zijn wanneer er mechanische spanning in het grafeenkristal aanwezig is. In dit hoofdstuk heb ik ook laten zien dat de sterkste variaties in de werkfunctie bekomen kunnen worden door FLG te doperen: afhankelijk van het doperingsniveau en het aantal grafeenlagen kan de werkfunctie over een groot interval gevarieerd worden ($\approx$2eV).
In de volgende twee hoofdstukken (hoofdstukken 12 en 13) werd de nadruk verlegd van fysisorptie naar chemisorptie. Met andere woorden, de bestudeerde adsorbaten in deze hoofdstukken vormen covalente bindingen met de grafeenlagen. In hoofdstuk 12 werden 2 materialen onderzocht, namelijk grafaan en fluorografeen, die respectievelijk bestaan uit een volledig gehydrogeneerde of gefluoriseerde grafeenlaag. Er werden verschillende configuraties voor beide materialen onderzocht waarvan de 'chair'-configuratie in beide gevallen de meest stabiele bleek te zijn. Een andere, vrijwel onbekende, configuratie die de 'zigzag'-configuratie werd genoemd heeft een vormingsenergie die nauwelijks hoger is dan die van de 'chair'-configuratie en zelfs lager dan die van de beter gekende 'boat'-configuratie. Fluorografeen blijkt veel stabieler te zijn dan grafaan, wat vooral te wijten is aan een hogere desorptie energie voor F_2 in vergelijking met H_2. Er werd ook aangetoond dat er structurele verschillen zijn tussen grafaan en fluorografeen ten gevolge van de aanwezige ladingen in fluorografeen. Wanneer de berekende eigenschappen van fluorografeen vergeleken worden met beschikbare experimentele gegevens, bleken er sterke verschillen te zijn: voor al de onderzochte configuraties werden grotere bandkloven gevonden en ook de Young-modulus heeft een veel grotere theoretische waarde. Het werd beargumenteerd dat dit erop wijst dat de experimentele samples aanzienlijke hoeveelheden defecten bevatten. De aard van deze defecten vereist echter bijkomende studies met grotere supercellen.

In hoofdstuk 13 werd de hydrogenering van een dubbele laag grafeen onderzocht. De volgende vaststellingen konden worden gedaan: 1) een hydrogenering met een limiet van 50 at. % is mogelijk door waterstofatomen aan beide kanten van de dubbellaag te laten adsorberen, 2) in dat geval onstaan er chemische bindingen tussen de twee lagen en 3) wanneer de limiet van 50 at. % bereikt wordt ontstaat er een dubbellagig materiaal waarvan de elektronische eigenschappen gelijkaardig zijn aan die van grafaan.
Het laatste gedeelte van de thesis handelt over de doorlaatbaarheid van grafeenmembranen. De penetratie van een heliumatoom door perfect grafeen en grafeen met defecten werd hiervoor onderzocht. De relaxatie van de grafeenlaag ten gevolge van de impact van het heliumatoom bleek een zeer kleine invloed te hebben op de hoogte van de potentiaalberg zodat deze verwaarloosd kon worden. Dit komt doordat de tijdsschaal voor relaxatie van grafeen groter is dan de tijdsschaal waarin de interactie tussen het He atoom en het grafeenoppervlak zich afspeelt. De relaxatie van de grafeenlaag gebeurt pas nadat het He-atoom zich terug verwijderd heeft van het grafeenmembraan. De hoogte van de potentiaalberg voor penetratie vermindert exponentieel met de grootte van aanwezige defecten in het grafeenmembraan, maar het werd aangetoond dat de potentiaalberg voor kleine defecten nog steeds hoog genoeg is om de ondoordringbaarheid van de grafeenmembranen te garanderen.

Appendices

Appendix A

In case the system under study is a solid, there are a lot of nuclei and electrons to be incorporated into the Schrödinger equation. A regular (3D) solid consists of roughly 10^{24} atoms/cm^3 whereas for graphene (2D) there are about 10^{16} atoms/cm^2. It is impossible to include all these particles separately in any model but in case the solid is a crystal we can make use of the translational symmetry.
Suppose the translational symmetry of the crystal is determined by the three primitive translation vectors $\mathbf{a}_1$, $\mathbf{a}_2$, and $\mathbf{a}_3$. This means that the external potential V_{ext}, which consists of the sum of potentials of all the nuclei, is invariant under any translation $\mathbf{R} = n_1\mathbf{a}_1 + n_2\mathbf{a}_2 + n_3\mathbf{a}_3$, with $n_1, n_2, n_3 \in \mathbb{Z}$, i.e.

$$V_{ext}(\mathbf{r} + \mathbf{R}) = V_{ext}(\mathbf{r}) \tag{A-1}$$

Consequently, the hamiltonian (3.6) is also invariant under these translations. Defining the operator $\hat{T}_{\mathbf{R}}$ through its operation on a function $f(\mathbf{r}_1, ..., \mathbf{r}_N)$ as $\hat{T}_{\mathbf{R}} f(\mathbf{r}_1, ..., \mathbf{r}_N) = f(\mathbf{r}_1 + \mathbf{R}, ..., \mathbf{r}_N + \mathbf{R})$ it follows that

$$[\hat{H}, \hat{T}_{\mathbf{R}}] = 0. \tag{A-2}$$

Furthermore, the application of two successive translations does not depend on the order in which they are applied, i.e. all the translation operators $\hat{T}_{\mathbf{R}}$ commute. Consequently, it is possible to choose simultaneous eigenfunctions for the operators $\hat{H}$ and all $\hat{T}_{\mathbf{R}}$. Although it is possible to derive a Bloch theorem for the many-body wavefunction, we will switch now to the usual independent particle picture in which the original Bloch theorem was derived [127]. The independent particle picture is also the only one in which we are going to make use of the Bloch theorem. Moreover it is more convenient, albeit not necessary, to introduce the Bloch theorem with periodic boundary conditions:

$$(\hat{T}_{\mathbf{a}_1})^{N_1} = (\hat{T}_{\mathbf{a}_2})^{N_2} = (\hat{T}_{\mathbf{a}_3})^{N_3} = \hat{1} \qquad \text{with} \qquad N_1, N_2, N_3 \in \mathbb{N}, \tag{A-3}$$

Let us take a closer look at the operator $\hat{T}_{\mathbf{R}}$ operating on the single-particle wavefunction $\psi(\mathbf{r})$, which is an eigenfunction of $\hat{H}$ and all $\hat{T}_{\mathbf{R}}$,

$$\hat{H}\psi(\mathbf{r}) = \epsilon\psi(\mathbf{r}) \tag{A-4}$$

$$\hat{T}_{\mathbf{R}}\psi(\mathbf{r}) = t_{\mathbf{R}}\psi(\mathbf{r}) \tag{A-5}$$

First $\hat{T}_{\mathbf{R}}$ has the property $\hat{T}_{\mathbf{R}}\hat{T}_{\mathbf{R}'} = \hat{T}_{\mathbf{R}'}\hat{T}_{\mathbf{R}} = \hat{T}_{\mathbf{R}+\mathbf{R}'}$. A similar relation holds for the eigenvalues $t_{\mathbf{n}}$ of the translation operator

$$\hat{T}_{\mathbf{R}}\hat{T}_{\mathbf{R}'}\psi(\mathbf{r}) = t_{\mathbf{R}}t_{\mathbf{R}'}\psi(\mathbf{r}) = t_{\mathbf{R}+\mathbf{R}'}\psi(\mathbf{r}) = \hat{T}_{\mathbf{R}+\mathbf{R}'}\psi(\mathbf{r}) \tag{A-6}$$

So it is possible to write any eigenvalue of $\hat{\mathbf{T}}_{\mathbf{n}}$ as

$$t_{\mathbf{R}} = (t_{\mathbf{a}_1})^{n_1}(t_{\mathbf{a}_2})^{n_2}(t_{\mathbf{a}_3})^{n_3}. \tag{A-7}$$

Therefore the problem is reduced to finding the explicit expressions for the eigenvalues of the translation operators corresponding with the primitive translation vectors, $\{\mathbf{a}_i\}$. These can be derived from the periodic boundary conditions (A-3) which imply that $(t_{\mathbf{a}_i})^{N_i} = 1$. The are exactly N_i different solutions for this equation,

$$t_{\mathbf{a}_i} = e^{i2\pi m/N_i} \qquad \text{with} \quad m = 1, ..., N_i. \tag{A-8}$$

It is very convenient now to introduce the concept of reciprocal space to express the eigenvalues for an arbitrary translation operator $\hat{T}_{\mathbf{n}}$.

> With each lattice, determined by the primitive lattice vectors $\{\mathbf{a}_i\}$, there corresponds a reciprocal lattice determined by the reciprocal basis vectors $\{\mathbf{b}_i\}$ which are defined by $\mathbf{a}_i \cdot \mathbf{b}_j = 2\pi\delta_{ij}$. Any point in reciprocal space can be expressed in this basis.

If we define the vector $\mathbf{k}$ in reciprocal space as

$$\mathbf{k}_{\mathbf{m}} = \frac{m_1}{N_1}\mathbf{b}_1 + \frac{m_2}{N_2}\mathbf{b}_2 + \frac{m_3}{N_3}\mathbf{b}_3, \tag{A-9}$$

we can write, using (A-7) and (A-8),

$$\hat{T}_{\mathbf{R}}\psi_{\mathbf{m}}(\mathbf{r}) = \psi_{\mathbf{m}}(\mathbf{r} + R) = e^{i\mathbf{k}_{\mathbf{m}}\cdot\mathbf{R}}\psi(\mathbf{r}) \tag{A-10}$$

For a crystal with around 10^{24} atoms N_1, N_2, and N_3 become very large and, consequently, the wavevector $\mathbf{k}_{\mathbf{m}}$ can be written as a continuous variable, $\mathbf{k}$,

$$\mathbf{k}_{\mathbf{m}} = \frac{m_1}{N_1}\mathbf{b}_1 + \frac{m_2}{N_2}\mathbf{b}_2 + \frac{m_3}{N_3}\mathbf{b}_3 \quad \longrightarrow \quad \mathbf{k} = k_1\mathbf{b}_1 + k_2\mathbf{b}_2 + k_3\mathbf{b}_3, \tag{A-11}$$

with $k_1, k_2, k_3 \in [0, 1]$. It is easy to see that any function satisfying (A-10) can then be written as

$$\psi_{\mathbf{k}}(\mathbf{r}) = e^{i\mathbf{k}\cdot\mathbf{r}} u_{\mathbf{k}}(\mathbf{r}) \tag{A-12}$$

with $u_{\mathbf{k}}(\mathbf{r})$ an arbitrary periodic function with the same periodicity as the lattice $u_{\mathbf{k}}(\mathbf{r} + \mathbf{R}) = u_{\mathbf{k}}(\mathbf{r})$. So the problem has been reduced to finding $u_{\mathbf{k}}(\mathbf{r})$ in a single unitcell for every $\mathbf{k}$-point of reciprocal space. However, since the Bloch-states are invariant for transformation of the form $\mathbf{k} \rightarrow \mathbf{k} + \mathbf{G}$ (with $\mathbf{G} = m_1\mathbf{b}_1 + m_2\mathbf{b}_2 + m_3\mathbf{b}_3$), we can restrict $\mathbf{k}$ to the so-called first Brillouin zone (1BZ) defined by

$$\mathbf{k} \in \text{1BZ} \qquad \text{if} \quad |\mathbf{k} + \mathbf{G}| > |\mathbf{k}| \quad \text{for any } \mathbf{G}. \tag{A-13}$$

Bibliography

[1] K. S. Novosolov, A. K. Geim, S. V. Morozov, D. Jiang, Y. Zhang, S. V. Dubonos, I. V. Grigorieva, and A. Firsov, Science **306**, 666 (2004).

[2] E. H. L. Falcao and F. Wudl, J. Chem. Tech. Biotech. **82**, 524 (2007).

[3] A. K. Geim and K. S. Novosolov, Nat. Materials **6**, 183 (2007).

[4] R. E. Peierls, **5**, 177 (1935).

[5] L. D. Landau, Phys. Z. Sowjetunion **11**, 26 (1937).

[6] J. C. Meyer, A. K. Geim, M. I. Katsnelson, K. S. Novoselov, T. J. Booth, and S. Roth, Nature (London) **446**, 60 (2006).

[7] M. I. Katsnelson, K. S. Novosolov, and A. K. Geim, Nat. Phys. **2**, 620 (2006).

[8] S. Das Sarma, S. Adam, E. H. Hwang, and E. Rossi.

[9] S. Park and R. S. Ruoff, Nat. Nanotechnol. **4**, 217 (2009).

[10] V. C. Tung, M. J. Allen, Y. Yang, and R. B. Kaner, Nat. Nanotechnol. **4**, 25 (2009).

[11] X. Y. Yang, X. Dou, A. Rouhanipour, L. J. Zhi, H. J. Rader, and K. Mullen, J. Am. Chem. Soc. **130**, 4216 (2008).

[12] J. Hass, W. A. de Heer, and E. H. Conrad, J. Phys. **20**, 323202 (2008).

[13] F. Varchon, R. Feng, J. Hass, X. Li, B. N. Nguyen, C. Naud, P. Mallet, J.-Y. Veuillen, C. Berger, E. H. Conrad, and L. Magaud, Phys. Rev. Lett. **99**, 126805 (2007).

[14] K. S. Kim, Y. Zhao, H. Jang, S. Y. Lee, J. M. Kim, J. H. Ahn, P. Kim, J. Y. Choi, and B. H. Hong, Nature (London) **457**, 706 (2009).

[15] F. Schedin, A. K. Geim, S. V. Morozov, E. W. Hill, P. Blake, M. I. Katsnelson, and K. S. Novosolov, Nat. Materials **6**, 652 (2007).

[16] H. Hellmann, Deuticke, Leipzig (1964).

[17] R. P. Feynman, Phys. Rev. **56**, 340 (1939).

[18] D. R. Hartree, Proc. Cambridge Phil. Soc. **24**, 89, 111, 426 (1928).

[19] J. C. Slater, Phys. Rev. **35**, 210 (1930).

[20] V. Fock, Z. Phys. **61**, 126 (1930).

[21] C. C. J. Roothaan, Rev. Mod. Phys. **23**, 69 (1951).

[22] P. Hohenberg and W. Kohn, Phys. Rev. **136**, B864 (1964).

[23] W. Kohn and L. J. Sham, Phys. Rev. **140**, A1133 (1965).

[24] N. C. Handy, Lecture Notes in Quantum Chemistry II, B. O. Roos (ed.), Springer, Heidelberg (1994).

[25] D. M. Ceperley and B. J. Alder, Phys. Rev. Lett. **566**, 1980 (2008).

[26] D. R. Hamann, M. Schlüter, and C. Chiang, Phys. Rev. Lett. **43**, 1494 (1979).

[27] N. Troullier and J. L. Martins, Phys. Rev. B **43**, 1993 (1991).

[28] P. E. Blöchl, Phys. Rev. B **50**, 17953 (1994).

[29] S. Fahy, X. W. Wang, and S. G. Louie, Phys. Rev. B **42**, 3503 (1990).

[30] C. Jang, S. Adam, J.-H. Chen, E. D. Williams, S. Das Sarma, and M. S. Fuhrer, Phys. Rev. Lett. **101**, 146805 (2008).

[31] A. N. Rudenko, F. J. Keil, M. I. Katsnelson, and A. I. Liechtenstein, Phys. Rev. B **82**, 035427 (2010).

[32] J. Zhao, A. Buldum, J. Han, and J. P. Lu, Nanotechnology **13**, 195 (2002).

[33] S. Santucci, S. Picozzi, F. Di Gregorio, L. Lozzi, C. Cantalini, L. Valentini, J. M. Kenny, and B. Delley, Phys. Rev. **35**, 210 (1930).

[34] J. Robinson, E. Snow, S. Badescu, T. Reinecke, and F. Perkins, Nano Lett. **6**, 1747 (2006).

[35] S. Peng and K. Cho, Nanotechnology **11**, 57 (2000).

[36] S. Peng, K. Cho, P. Qi, and H. Dai, Nanotechnology **11**, 57 (2000).

[37] X. Gonze, J.-M. Beuken, R. Caracas, F. Detraux, M. Fuchs, G.-M. Rignanese, L. Sindic, M. Verstraete, G. Zerah, F. Jollet, M. Torrent, A. Roy, M. Mikami, P. Ghosez, J.-Y. Raty, and D. C. Allan, Comp. Mat. Science **25**, 478 (2002).

[38] J. P. Perdew, K. Burke, and M. Ernzerhof, Phys. Rev. Lett. **77**, 3865 (1996).

[39] H. J. Monkhorst and J. D. Pack, Phys. Rev. B **13**, 5188 (1971).

[40] F. L. Hirshfeld, Theor. Chim. Acta **44**, 129 (1977).

[41] B. S. González, J. Hernández-Rojas, J. Bretón, and J. M. Gomez Llorente, J. Phys. Chem. C **111**, 14862 (2007).

[42] T. O. Wehling, K. S. Novoselov, S. V. Morozov, E. E. Vdovin, M. I. Katsnelson, A. K. Geim, and A. I. Lichtenstein, Nano Lett. **8**, 173 (2008).

[43] J. Kong, N. R. Franklin, C. Zhou, M. G. Chapline, S. Peng, K. Cho, and H. Dai, Science **287**, 622 (2000).

[44] J. Li, Y. Lu, Q. Ye, M. Cinke, J. Han, and M. Meyyappan, Nano Lett. **3**, 902 (2003).

[45] K. Bradley, J.-C. P. Gabriel, M. Briman, A. Star, and G. Grüner, Phys. Rev. Lett. **91**, 218301 (2003).

[46] P. Qi, O. Vermesh, M. Grecu, A. Javey, Q. Wang, H. Dai, S. Peng, and K. J. Cho, Nano Lett. **3**, 347 (2003).

[47] C. Staii, A. T. Johnson Jr., M. Chen, and A. Gelperin, Nano Lett. **5**, 1774 (2005).

[48] X. Tang, S. Bansaruntip, N. Nakayama, E. Yenilmez, Y.-I. Chang, and Q. Wang, Nano Lett. **6**, 1632 (2006).

[49] E. H. Hwang, S. Adam, and S. Das Sarma, Phys. Rev. B **76**, 195421 (2007).

[50] C. Lee, X. Wei, J. W. Kysar, and J. Hone, Science **321**, 385 (2008).

[51] I. Zanella, S. Guerini, S. B. Fagan, J. M. Filho, and A. G. S. Filho, Phys. Rev. B **77**, 073404 (2008).

[52] R. S. Mulliken, J. Chem. Phys. **23**, 2343 (1955).

[53] R. F. Bader, Chem. Rev. **91**, 893 (1991).

[54] P. Bultinck, C. Van Alsenoy, P. W. Ayers, and R. Carbó-Dorca, J. Chem. Phys. **126**, 144111 (2007).

[55] H. E. Romero, P. Joshi, A. K. Gupta, H. R. Gutierrez, M. W. Cole, S. A. Tadigadapa, and P. C. Eklund, Nanotechnology **20**, 245501 (2009).

[56] D. R. Hamman, Phys. Rev. B **55**, 10157 (1997).

[57] T. Kurita, S. Okada, and A. Oshiyama, Phys. Rev. B **75**, 205424 (2007).

[58] A. Maiti, J. Andzelm, N. Tanpipat, and P. von Allmen, Phys. Rev. Lett. **87**, 155502 (2001).

[59] T. O. Wehling, A. I. Lichtenstein, and M. I. Katsnelson, Appl. Phys. Lett. **93**, 202110 (2008).

[60] S. Xantheas and T. H. Dunning, J. Chem. Phys. **99**, 8774 (1993).

[61] F. K. Keutsch and R. J. Saykally, Proc. Natl. Acad. Sci. U.S.A **98**, 10533 (2001).

[62] S. Maheshwary, N. Patel, N. Sathyamurthy, A. D. Kulkarni, and S. R. Gadre, J. Phys. Chem. A **105**, 10525 (2001).

[63] J. Berashevich and T. Chakraborty, Phys. Rev. B **80**, 033404 (2009).

[64] M. C. Gordillo and J. Marti, Phys. Rev. B **78**, 075432 (2008).

[65] J. Moser, A. Verdaguer, D. Jiménez, A. Barreiro, and A. Bachtold, Appl. Phys. Lett. **92**, 123507 (2008).

[66] M. I. Landstrass and K. Ravi, Appl. Phys. Lett. **55**, 1391 (1989).

[67] V. Chakrapani, J. C. Angus, A. B. Anderson, S. D. Wolter, B. R. Stoner, and G. U. Sumanasekera, Science **318**, 1424 (2007).

[68] T. Takahashi, H. Tokailin, and T. Sagawa, Phys. Rev. B **32**, 8317 (1985).

[69] K. Ihm, J. T. Lim, K.-J. Lee, J. W. Kwon, T.-H. Kang, S. Chung, S. Bae, J. H. Kim, B. H.

Hong, and G. Y. Yeom, Appl. Phys. Lett. **97**, 032113 (2010).
[70] N. Ooi, A. Rairkar, and J. B. Adams.
[71] S.-M. Choi, S.-H. Jhi, and Y.-W. Son, Phys. Rev. B **81**, 081407 (2010).
[72] Y.-J. Yu, Y. Zhao, S. Ryu, L. E. Brus, K. S. Kim, and P. Kim, Nano Lett. **9**, 3430 (2009).
[73] H. Hibino, H. Kageshima, M. Kotsugi, F. Maeda, F.-Z. Guo, and Y. Watanabe, Phys. Rev. B **79**, 125437 (2009).
[74] P. Avouris, Z. Chen, and V. Perebeinos.
[75] A. K. Geim, Science **324**, 1530 (2009).
[76] S. Patchkovskii, J. S. Tse, S. N. Yurchenko, L. Zhechkov, T. Heine, and G. Seifert, Proc. Natl. Acad. Sci. U.S.A **102**, 10439 (2007).
[77] S. Ryu, M. Y. Han, J. Maultzsch, T. F. Heinz, P. Kim, M. L. Steigerwald, and L. E. Brus, Nano Lett. **8**, 4597 (2008).
[78] D. C. Elias, R. R. Nair, T. M. G. Mohiuddin, S. V. Morozov, P. Blake, M. P. Halsall, A. C. Ferrari, D. W. Boukhvalov, A. K. Geim, and K. S. Novosolov, Science **323**, 610 (2009).
[79] D. O'Hagan.
[80] D. W. Boukhvalov, M. I. Katsnelson, and A. I. Lichtenstein, Phys. Rev. B **77**, 035427 (2008).
[81] M. Y. Han, B. Özyilmaz, Y. Zhang, and P. Kim, Phys. Rev. Lett. **98**, 206805 (2007).
[82] T. Ohta, A. Bostwick, T. Seyller, K. Horn, and E. Rotenberg, Science **313**, 951 (2006).
[83] E. McCann, Phys. Rev. B **74**, 161403 (2006).
[84] S. H. Cheng, K. Zou, F. Okino, H. R. Gutierrez, A. Gupta, N. Shen, P. C. Eklund, J. O. Sofo, and J. Zhu, Phys. Rev. B **81**, 205435 (2010).
[85] F. Withers, M. Dubois, and A. K. Savchenko.
[86] R. R. Nair, W. C. Ren, R. Jalil, I. Riaz, V. G. Kravets, L. Britnell, P. Blake, F. Schedin, A. S. Mayorov, S. Yuan, M. I. Katsnelson, H. M. Cheng, W. Strupinski, L. G. Bulusheva, A. V. Okotrub, K. S. Novoselov, A. K. Geim, I. V. Grigorieva, and A. N. Grigorenko.
[87] D. A. Dikin, S. Stankovich, E. J. Zimney, R. D. Piner, G. Dommett, G. H. B. and. Evmenenko, S. T. Nguyen, and R. S. Ruoff, Nature (London) **448**, 457 (2007).
[88] G. Eda and M. Chhowalla, **22**, 2392 (2010).
[89] M. H. F. Sluiter and Y. Kawazoe, Phys. Rev. B **68**, 085410 (2003).
[90] J. O. Sofo, A. S. Chaudhari, and G. D. Barber, Phys. Rev. B **75**, 153401 (2007).
[91] J.-C. Charlier, X. Gonze, and J.-P. Michenaud, Phys. Rev. B **47**, 16162 (1993).
[92] M. Klintenberg, S. Lebègue, M. I. Katsnelson, and O. Eriksson, Phys. Rev. B **81**, 0855433 (2010).
[93] E. Muñoz, A. K. Singh, M. A. Ribas, E. S. Penev, and B. I. Yakobson, Diamond and Rel. Mat. **19**, 351 (2010).
[94] F. Liu, P. Ming, and J. Li, Phys. Rev. B **76**, 064120 (2007).
[95] C. Bittencourt, G. Van Lier, X. Ke, I. Martinez-Suarez, A. Felten, J. Ghijsen, G. Van Tendeloo, and C. Ewels, **10**, 920 (2009).
[96] G. Van Lier, G. Van Assche, H. Miltner, N. Grossiord, C. Koning, P. Geerlings, and B. Van Mele, Phys. Chem. Chem. Phys. **11**, 11121 (2009).
[97] S. Osuna, M. Torrent-Sucarrat, C. Ewels, M. Sola, P. Geerlings, and G. Van Lier.
[98] S. Osuna, M. Torrent-Sucarrat, , M. Sola, P. Geerlings, and G. Ewels, C.P. Van Lier.
[99] A. Marini, C. Hogan, M. Grüning, and D. Varsano, Phys. Commun. **180**, 1392 (2009).
[100] L. Hedin, Phys. Rev. **139**, A796 (1965).
[101] C. A. Rozzi, D. Varsano, A. Marini, G. E. K. U., and A. Rubio, Phys. Rev. B **73**, 205119 (2006).
[102] S. S. Han, T. H. Yu, B. V. Merinov, A. C. T. van Duin, R. Yazami, and W. A. Goddard,

Chem. Mat. **22**, 2142 (2010).
[103] M. Z. S. Flores, P. A. S. Autreto, S. B. Legoas, and D. S. Galvao, Nanotechnology **20**, 465704 (2009).
[104] O. Leenaerts, B. Partoens, and F. M. Peeters, Phys. Rev. B **80**, 245422 (2009).
[105] M. Topsakal, S. Cahangirov, and S. Ciraci, Appl. Phys. Lett. **96**, 091912 (2010).
[106] M. F. Thorpe and P. N. Sen, J. Accoust. Soc. Am. **77**, 1674 (1994).
[107] J. Berashevich and T. Chakraborty, Nanotechnology **21**, 355201 (2010).
[108] K. Guerin, J. P. Pinheiro, M. Dubois, Z. Fawal, F. Masin, R. Yazami, and A. Hamwi, Chem. Mat. **16**, 1786 (2006).
[109] R. H. Telling, C. P. Ewels, A. A. El-Barbary, and M. I. Heggie, Nat. Materials **2**, 333 (2003).
[110] M. Torrent, F. Jollet, F. Bottin, G. Zerah, and X. Gonze, Comp. Mat. Science **42**, 337 (2008).
[111] D. W. Boukhvalov and Katsnelson, Phys. Rev. B **78**, 085413 (2008).
[112] Z. Luo, T. Yu, K.-j. Kim, Z. Ni, Y. You, S. Lim, Z. Shen, S. Wang, and J. Lin, ACS Nano **7**, 1781 (2009).
[113] J. S. Bunch, S. S. Verbridge, v. d. Z. A. M. Alden, J. S., J. M. Parpia, H. G. Craighead, and P. L. McEuen, Nano Lett. **8**, 2458 (2008).
[114] O. Leenaerts, B. Partoens, and F. M. Peeters, Appl. Phys. Lett. **93**, 19307 (2008).
[115] S. Casolo, O. M. Lø vvik, R. Martinazzo, and G. F. Tantardini, J. Chem. Phys. **130**, 54704 (2009).
[116] L. Hornekæ r, v. Šljivančanin, W. Xu, R. Otero, E. Rauls, I. Stensgaard, E. Læ gsgaard, B. Hammer, and F. Besenbacher, Phys. Rev. Lett. **96**, 156104 (2006).
[117] L. Hornekæ r, E. Rauls, W. Xu, v. Šljivančanin, R. Otero, I. Stensgaard, E. Læ gsgaard, B. Hammer, and F. Besenbacher, Phys. Rev. Lett. **97**, 186102 (2006).
[118] N. P. Guisinger, G. M. Rutter, J. N. Crain, P. N. First, and J. A. Stroscio, Nano Lett. **9**, 1462 (2009).
[119] E. V. Castro, K. S. Novosolov, S. V. Morozov, N. M. R. Peres, J. M. B. Lopes dos Santos, J. Nilsson, F. Guinea, A. K. Geim, and A. H. Castro Neto, Phys. Rev. Lett. **99**, 216802 (2007).
[120] J. Kanasaki, E. Inami, K. Tanimura, H. Ohnishi, and K. Nasu, Phys. Rev. Lett. **102**, 087402 (2009).
[121] C. Z. Lee, G. D. and. Wang, E. Yoon, N. M. Hwang, D. Y. Kim, and K. M. Ho, Phys. Rev. Lett. **95**, 205501 (2005).
[122] C. Z. Lee, G. D. and. Wang, E. Yoon, N. M. Hwang, D. Y. Kim, and K. M. Ho, Phys. Rev. B **74**, 245411 (2006).
[123] L. Verlet, Phys. Rev. **159**, 98 (1967).
[124] L. Verlet, Phys. Rev. **165**, 201 (1968).
[125] J. Hrušák, D. K. Böhme, T. Weiske, and H. Schwarz, **193**, 97 (1992).
[126] A. Ito, H. Nakamura, and A. Takayama, J. Phys. Soc. Jap. **77**, 114602 (2008).
[127] F. Bloch, Z. Phys. **52**, 555 (1928).

Curriculum Vitae

Name:	**Ortwin LEENAERTS**
Born:	12/04/1984, Schoten
Contact:	Groenenborgerlaan 171 (U206) 2020, Antwerpen Belgium
E-mail:	Ortwin.Leenaerts@ua.ac.be

Education

2006-2010:	PhD in Physics, University of Antwerp
2002-2006:	Master in Physics, University of Antwerp

Teaching experience (exercises)

2007-2008	Advanced quantum mechanics
2008-2009	Introductory quantum mechanics
2009-2010	Introductory quantum mechanics
2010-2011	Numerical methods

Computer skills

Operating systems:	Windows, Linux
Office:	Word, Excel, PowerPoint
Programming (basic):	C/C++, Fortran, Java
DFT packages:	ABINIT, Siesta
Mathematical software:	MATLAB, Maple, Mathematica

Languages

Dutch (native), English (fluent), French (good), German (basic)

List of publications

- O. Leenaerts, B. Partoens, and F. M. Peeters, *Adsorption of H_2O, NH_3, CO, NO_2, and NO on graphene: A first-principles study*, Physical Review B **77**, 125416 (2008) (SCI IF: 3.322).
- O. Leenaerts, B. Partoens, and F. M. Peeters, *Paramagnetic adsorbates on graphene: A charge transfer analysis*, Applied Physics Letters **92**, 243125 (2008) (SCI IF: 3.726).
- O. Leenaerts, B. Partoens, and F. M. Peeters, *Graphene: A perfect nanoballoon*, Applied Physics Letters **93**, 193107 (2008) (SCI IF: 3.726).
- O. Leenaerts, B. Partoens, and F. M. Peeters, *Adsorption of small molecules on graphene*, Microelectronics Journal **40**, 860 (2009) (SCI IF: 0.859).
- O. Leenaerts, B. Partoens, and F. M. Peeters, *Water on graphene: Hydrophobicity and dipole moment using density functional theory*, Physical Review B **79**, 235440 (2009) (SCI IF: 3.322).
- O. Leenaerts, B. Partoens, and F. M. Peeters, *Hydrogenation of bilayer graphene and the formation of bilayer graphane*, Physical Review B **80**, 245422 (2009) (SCI IF: 3.322).
- O. Leenaerts, H. Peelaers, A. D. Hernández-Nieves, B. Partoens, and F. M. Peeters, *First-principles investigation of graphene fluoride and graphane*, Physical Review B **82**, 195436 (2010).
- H. Peelaers, A. D. Hernández-Nieves, O. Leenaerts,B. Partoens, and F. M. Peeters, *Vibrational properties of graphene uoride and graphane*, submitted to Applied Physics Letters.